ACS APPLIED NANO MATERIALS

www.acsanm.org Review

Visible-Light-Active Doped Metal Oxide Nanoparticles: Review of their Synthesis, Properties, and Applications

Riddhiman Medhi, Maria D. Marquez, and T. Randall Lee*

Cite This: *ACS Appl. Nano Mater.* 2020, 3, 6156–6185 Read Online

ACCESS | Metrics & More | Article Recommendations

ABSTRACT: Metal oxide semiconductors with a bandgap between 2 and 4 eV are an important class of compounds in the electronics industry and for photocatalysis. With the demand for these materials expanding rapidly, especially in the field of photocatalysis, the fabrication of nanoscale metal oxide particles, which increases the surface-to-volume ratio and thereby reduces the materials costs, is an emphasis of current research. For the purpose of photocatalysis, another important quality is the ability to absorb light efficiently. However, due to the wide bandgap of metal oxide semiconductors, the absorptions are limited to the UV region. Conveniently, a wider range of wavelengths and physical properties can be enabled by doping these metal oxide nanoparticles. Furthermore, the synthesis of doped metal oxides in nanoparticle form offers utility in an expansive array of systems, substrates, and dispersion media. However, the reliable synthesis of nanosized colloidal particles of doped metal oxides remains an ongoing challenge for materials researchers. This manuscript gives a concise overview of research conducted regarding the synthesis of visible-light-active doped metal oxide nanoparticles (NPs) and analyzes how doping impacts the optical properties, making them active in the visible to near-infrared regions. The effects of doping on applications are also summarized. Given that the most commonly doped metal oxide materials are TiO_2 and ZnO, this review highlights both anion- and cation-doped TiO_2 and ZnO nanoparticles. In addition, doped perovskite nanoparticles (e.g., $BaTiO_3$ and $SrTiO_3$) as well as some of the lesser studied doped metal oxide nanoparticle systems are covered. This work is intended to provide not only a broad overview of existing doped metal oxide nanoparticles but also a foundation for the development of semiconducting nanoparticle architectures for next-generation applications.

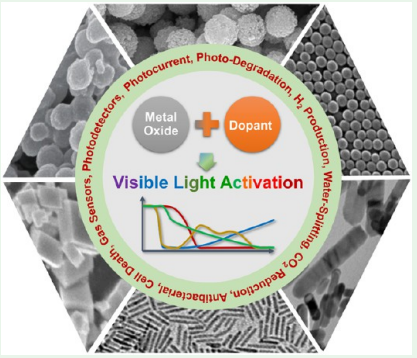

KEYWORDS: *metal oxide, doped, bandgap, visible, photocatalyst, antibacterial, dye degradation, water splitting*

1. INTRODUCTION

Traditional semiconductors (with a bandgap <2 eV) have revolutionized the electronics industry in the last few decades.[1,2] In particular, Si and GaAs have been the frontrunners in driving this revolution. However, the continued thinning of devices and the increasing need for processing power are motivating the search for new materials that can withstand high power loads. Wide bandgap semiconductors with a bandgap between 2−4 eV and typically >3 eV offer possible solutions because the wider bandgap allows them to withstand rapid switching frequencies and high power loads while maintaining insulating properties.[3−6] Additionally, wide bandgap semiconductors are also stable at high temperatures, can work under high voltages and currents, and exhibit high carrier density and mobility.[3−7] Silicon carbide (SiC) and gallium nitride (GaN) are the most commonly explored wide bandgap materials and are used widely in light-emitting diodes (LEDs), lasers, and solar cells.[4,6,8] However, such wide bandgap semiconducting materials are chemically sensitive, especially toward oxidation,[3] which creates complications with respect to their fabrication, modification, and utilization.

Alternatively, wide bandgap metal oxides offer a solution to the aforementioned shortcomings.[3,9] In addition to possessing a wide bandgap, metal oxides, in lieu of already being in the oxidized state, resist oxidation at high temperatures and are robust under a wide variety of chemical environments.[3,9] These characteristics are especially important for photocatalysis, a contact process, where the chemical stability of wide bandgap metal oxides is massively important, as is the need for compatibility with a wide variety of reaction media and reacting species. The wide bandgap of most metal oxides is also comparable to electrode potentials of many important reactions, such as the splitting of water to produce both hydrogen and oxygen, reduction of CO_2, oxidation of organic molecules, and the degradation of dyes and other pollu-

Received: April 18, 2020
Accepted: June 15, 2020
Published: June 15, 2020

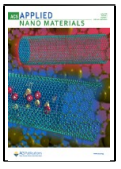

https://dx.doi.org/10.1021/acsanm.0c01035
ACS Appl. Nano Mater. 2020, 3, 6156–6185

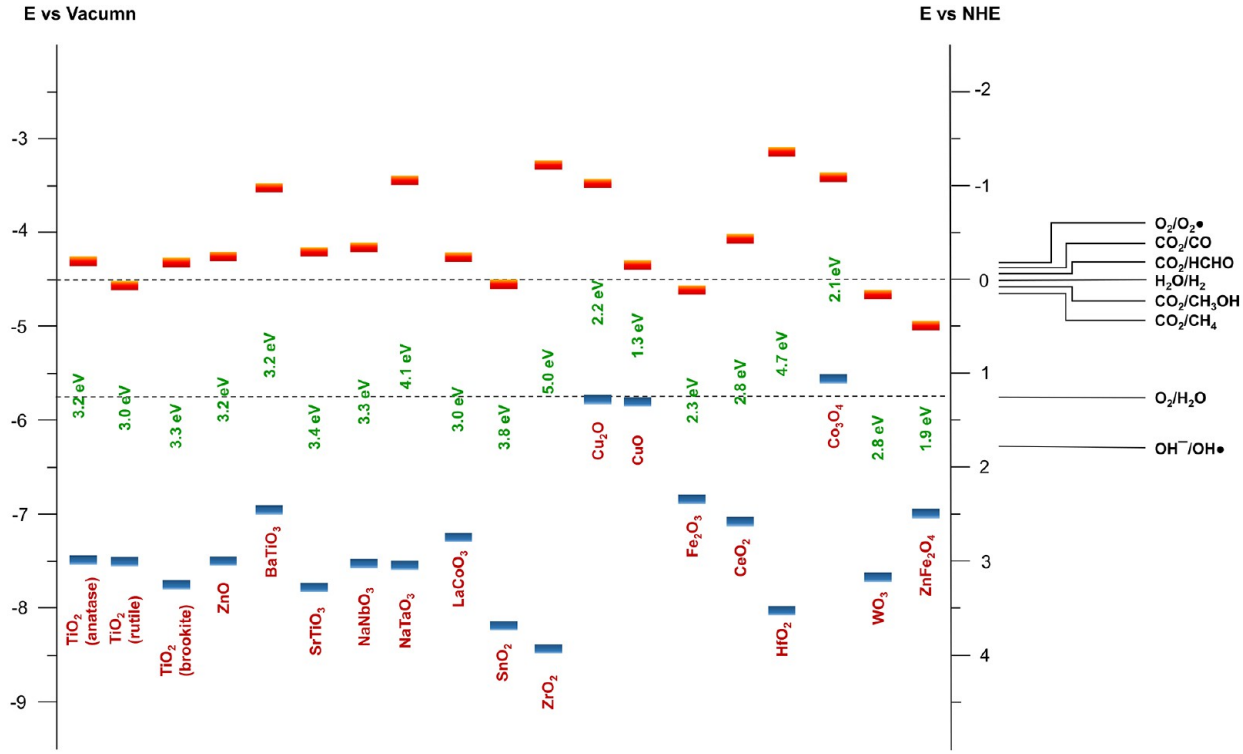

Figure 1. Bandgap, band-edge positions with respect to the vacuum level, and normalized hydrogen electrode (NHE, at pH 0) for common metal oxides. The horizontal red lines represent the conduction edges, and the horizontal blue lines represent the valence band edges. The right-hand *y*-axis also represents the redox potential of different chemical species involved in common photocatalytic reactions.[11,15−27]

tants.[10,11] The bandgaps of commonly used metal oxides and their band-edge positions relative to commonly catalyzed reactions are illustrated in Figure 1. Upon irradiation by light having an appropriate wavelength, electrons are excited from the valence band (VB) to the conduction band (CB), while at the same time creating holes in the VB.[12] The photogenerated electrons can participate in reduction reactions, while the holes in the VB can catalyze oxidation reactions, making metal oxides powerful photocatalytic materials.[12] In addition to the aforementioned benefits, metal oxides are also the most abundant materials in the Earth's crust, which translates to low costs compared to other types of wide bandgap semiconductor materials. Metal oxides are also known for their good mechanical stress tolerance and compatibility with organic materials, extending their range of applications.[13] Interestingly, certain metal oxides, such as zinc oxide and tin oxide, can exhibit both conductivity and optical transparency, and are paving the way for the widespread use of transmitting conducting oxides (TCOs) in optoelectronic devices.[3,14]

Nevertheless, the desired wide bandgap for metal oxides comes at a price. The corresponding absorption of these materials is limited to the UV region (5% of the solar spectrum reaching the Earth's surface), which hinders their efficient utilization of the entire solar spectrum. Therefore, for the purpose of photocatalysis and photovoltaics, a more efficient absorption of solar light is desirable: one which encompasses a much wider range of wavelengths. This shortcoming is driving the search for wide bandgap metal oxide materials with optical responses in the visible to near-IR regions. One way of achieving this objective is to couple the metal oxides with visible-light-absorbing materials such as organic dyes or plasmonic noble metal nanoparticles.[28,29] An alternative approach is to tune the bandgap down toward the visible region, which can be effectively achieved by doping the metal oxides with selected elements.[12,30] In addition to down-tuning the bandgap, doping can also introduce new spectral features in the visible to near-IR regions, thereby increasing the overall absorption efficiency.

A majority of the studies conducted on doped metal oxides have featured bulk powders or as-deposited nanostructured films.[31−35] However, synthesis of stand-alone colloidal nanoparticles (NPs) allows better utilization of these materials by introducing a high surface-to-volume ratio.[36] For photocatalysis, which is a surface-specific process, the surface area per mass of material becomes an important quality for making these materials economically feasible. Correlations between photocatalytic activity and surface area are commonly observed in doped metal oxide films, powdered photocatalysts, and fibrous/porous/mesoporous micrometer-sized structures.[37−41] Surface area effects can be maximized through the synthesis and use of discrete nanosized particles. Fibrous and porous microstructures also assist the diffusion of charge carriers to the surface and inhibit recombination.[38,41] These enhancements can be better realized with nanoparticles, as their small size also enables ready migration of charge carriers to reaction sites on the surface, decreasing recombination.[38] In addition, well-developed stand-alone nanoparticles offer flexibility for use in suspensions and colloidal solution-phase reactions as well as keep the door open for deposition onto finely structured thin films.[42] The optical properties also change with decreasing size, whereupon the photocatalytic activity invariably increases.

Methods for the synthesis of nanoparticles vary widely and require a range of approaches and much greater control

https://dx.doi.org/10.1021/acsanm.0c01035
ACS Appl. Nano Mater. 2020, 3, 6156−6185

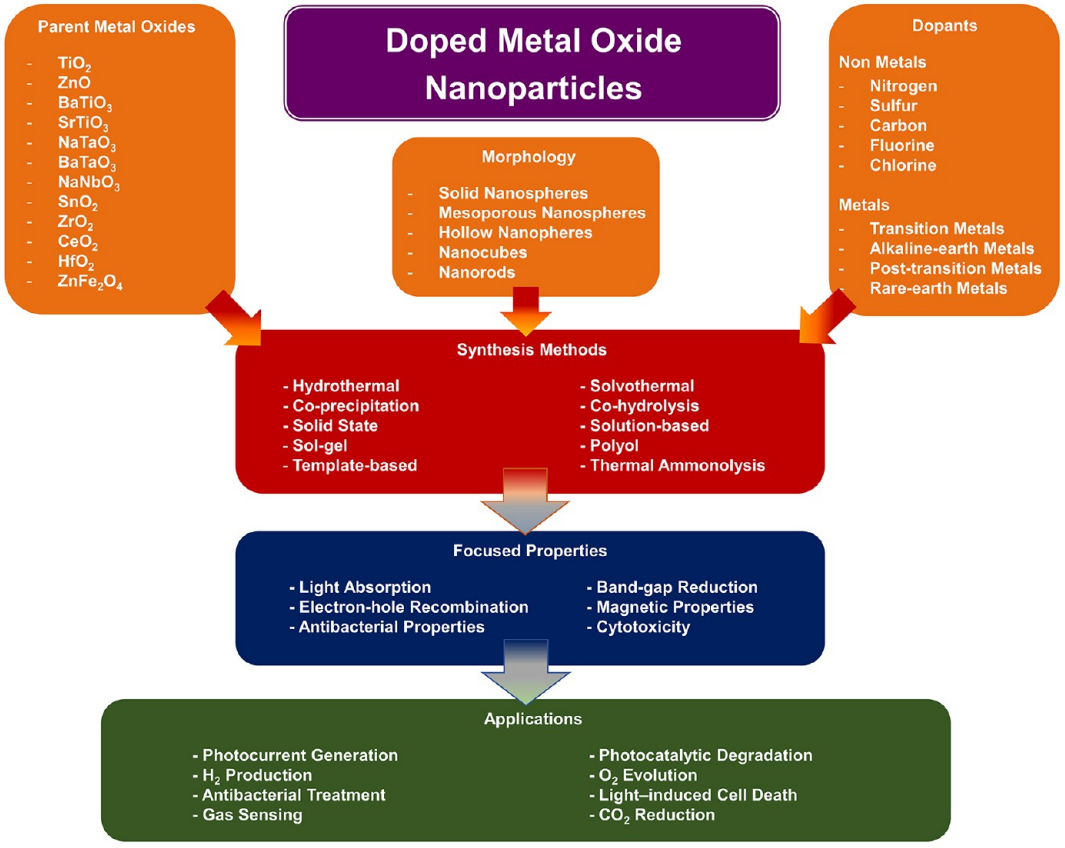

Figure 2. An overview of the synthesis, properties, and applications of doped metal oxide nanoparticles.

compared to bulk powders. Considering the importance of nanosized metal oxide particles, the number of reports for the reliable synthesis of doped metal oxide nanoparticles remains limited, largely due to the difficulties in stabilizing colloidal nanoparticles, which is compounded further with doping. Lower surface area typically corresponds to higher surface energy.[43] Doping often induces additional surface defects and vacancies that make the surface more reactive and unstable, leading to distortions in shape and homogeneity as well as problems with aggregation.[44] Given these considerations, there is a need to focus on and master the art of synthesizing doped metal oxide nanoparticles in a reliable fashion.

This review focuses on previously conducted research on the synthesis, properties, and applications of visible-light-active doped metal oxide nanoparticles. The effects of doping on the enhancement of visible-light absorption and corresponding enhancements in properties and their impacts on targeted applications will also be discussed, as outlined in Figure 2. The studies highlighted herein should provide a good foundation for the development of new semiconducting nanoparticle architectures for emerging and future applications.

2. SYNTHESIS OF METAL OXIDE NANOPARTICLES: BACKGROUND

Strategies for the synthesis of nanoparticles can be broadly classified as top-down or bottom-up. The top-down approach begins with large particles (macro- or microscale) that are broken down to nanosized particles, typically via mechanical processes such as milling. A major disadvantage of this approach is the lack of control over the shape, size, and uniformity of the resulting nanoparticles. In contrast, the bottom-up approach begins with atomic nuclei, which affords much greater control over the structural parameters. In the latter approach, the precursor salts of the constituent elements are treated with oxidizing/reducing agents, leading to seeding and growth of the desired nanoparticles. Bottom-up approaches were first explored and optimized with elemental nanoparticles of noble metals such as gold, silver, and palladium.[45,46] Later, the approaches were adapted for the synthesis of bimetallic nanoparticles, composed of two elements, starting with dual precursors.[47] Further advances in this field saw the nanoparticle synthesis of metal oxides, chalcogenides, polymers, carbon-based nanostructures, and recently doped and multicomponent versions of these materials.[12,46,48−53]

The primary advantage of the bottom-up approach is that the nanoparticle seeding and growth processes can be controlled by additional reagents acting as ligands, surfactants, and growth inhibitors.[54−56] Colloidal nanoparticles experience interparticle van der Waals attraction that pulls them closer, while high surface energies cause them to aggregate.[54] To inhibit aggregation, colloidal nanoparticles are often stabilized by the use of ligands or surfactants that bind to the surface of the nanoparticles, lowering their surface energy[54] and providing steric or electrostatic stabilization.[55] Commonly used surfactants include polyethylene glycols (PEGs), poly(vinyl alcohols) (PVAs), poly(vinylpyrrolidone) (PVP), polyacrylamides, Triton X-100, citrate, sodium dodecyl sulfate (SDS), and cetyltrim-ethylammonium chloride or bromide (CTAC, CTAB).[55] The addition of surfactants during synthesis can also stabilize the seeded nuclei or bind to the

https://dx.doi.org/10.1021/acsanm.0c01035
ACS Appl. Nano Mater. 2020, 3, 6156−6185

surfaces of the growing nanoparticles, providing additional control over the growth process.[56,57]

Nanoparticle seeding and growth processes can also be controlled by modifying a variety of parameters such as temperature, pressure, stir-speed, solvent, degassing, and reaction times. The most common methods for the synthesis of metal oxide nanoparticles are wet chemical methods, such as solution-based, hydrothermal, sol−gel, microwave-assisted, nonaqueous (solvothermal), and polyol methods. Solution-based methods are typically carried out in glass reactor vessels at temperatures below 150 °C. The advantages of this method are the ability to monitor the progress of the reaction visually, adjust stir-speed, stepwise addition of reagents, and the option to conduct the reaction under inert atmosphere or reflux conditions.[58] However, for the synthesis of metal oxides nanoparticles, hydrothermal methods are more common. Hydrothermal methods are sometimes also preceded by a low-temperature solution-based preparation step. Hydrothermal synthesis utilizes higher temperature and high pressure water conditions to generate nanoparticles from precursors that are insoluble at moderate temperatures and pressures.[59,60] Hydrothermal synthesis is usually carried out below 300 °C and can be regarded as an electrostatic reaction between metal ions and hydroxyl ions to generate the metal oxide.[59,60] Hydrothermal conditions are preferred over routine solution-based methods because high temperatures in a closed vessel, typically a Teflon-lined autoclave inside a stainless steel reactor, aids in the formation of crystalline nanoparticles. Furthermore, this facile and convenient method provides good control over homogeneity, size, composition, phase, and morphology.[59−61]

Another popular technique for metal oxide nanoparticle synthesis is the sol−gel technique. The sol−gel technique begins with a homogeneous solution of the precursors; after condensation of the solution to a gel, the solvent is dried to form the nanoparticles.[62,63] This technique is especially suitable for fabricating multicomponent nanoparticles with good control over size and shape, and can yield crystalline nanoparticles using ambient temperatures for sol and gel preparation.[62] Most of these methods typically require an additional calcination step to improve the crystallinity of the resulting nanoparticles.[64−66]

However, aqueous sol−gel and hydrothermal methods suffer from certain disadvantages due to the double role of water as ligand and solvent, complicating the synthesis of small structures.[67−69] As such, nonaqueous solvothermal and sol−gel methods have seen increased use for the synthesis of binary, ternary, and doped metal oxide nanoparticles.[67,68] Using organic solvents such as benzyl alcohol offers a better match in reactivity of metal oxide and dopant precursors, providing good control over size and shape.[67−69] The polyol method, using ethylene glycol and its derivatives as solvent, is another powerful method for controlled nanoparticle synthesis. The sheer multitude of available polyols with varying molecular weights and boiling points, combined with water-like solubility for common precursors, offers additional flexibility; furthermore, synthesis temperatures of 200−320 °C can be accessed without using autoclaves.[49] Wet chemical methods using combinations of oleic acid, oleyl amine, and oleic alcohol have also shown great success for the synthesis of uniform metal oxides at temperatures near 390 °C.[70,71] These high temperature processes allow for the formation of crystalline nanoparticles directly from the liquid phase.[49,67−69]

Notwithstanding the advantages of the above-mentioned wet chemical methods, these processes generally need long reaction times (typically between 4 to 48 h).[61] Microwaves can penetrate and supply heat throughout the volume of a material, enabling temperatures well above the boiling point of the solvent. Such heating can increase the speed of reactions by a factor of 10−1000, allowing reactions to be completed in minutes or even seconds.[61] Even at such rapid processing times, it has been observed that microwave-assisted synthesis can also maintain narrow size distribution and high purity.[61]

These aforementioned methods for the synthesis of metal oxide nanoparticles can be modified and adapted to fabricate doped metal oxide nanoparticles. Doped metal oxides are typically prepared via coprecipitation or cohydrolysis of the precursor of the parent metal with that of the dopant in the case of metal dopants;[72,73] in contrast, nonmetal doping (e.g., doping with N, C, and S) is typically achieved in the presence of ammonia, urea, thiourea, and the like.[74−76] These modified methods are described in greater detail in later sections.

3. DOPING IN METAL OXIDE NANOPARTICLES: BACKGROUND AND APPLICATIONS

Doping can induce changes to the crystal and electronic structure of the parent metal, which gives rise to changes in the bandgap. Both metals and nonmetals can be used as dopants for tuning the bandgap of metal oxide materials.[12,30] The most commonly used nonmetal dopants are nitrogen, carbon, phosphorus, fluorine, chlorine, iodine, sulfur, and other tellurides such as selenium and tellurium. The nonmetal dopant can substitute either at the oxygen or parent metal atomic sites or also exist as an interstitial dopant.[77] The 2p orbital contributions from these nonmetal dopants give rise to the creation of mixed or localized states near the edges of the valence and/or conduction bands that lead to a narrowing of the bandgap and visible-light activity.[12,30] Doping can also add additional dopant states in between the original bandgap that bring about significant new excitations corresponding to visible-light wavelengths.[78] The dopant acting as an impurity also leads to defects that can trigger additional optical features.[79,80] For example, oxygen vacancies created upon doping by nitrogen and sulfur in metal oxides often produce enhanced visible-light activity.[30,81] Additional trap states can be created that prevent spontaneous recombination of the charge carriers, thus extending the lifetime of electrons and holes.[79] Longer lifetimes for the charge carriers ensure better utilization of the charge carriers for the targeted processes.[82] On the other hand, doping can also create recombination centers that decrease the number of active charge carriers, especially at high doping percentages.[73,83,84] It has also been observed that codoping and tridoping with different elements is often more effective than monodoping for enhancing visible-light absorption.[74,76,85,86]

Metal dopants can also reduce the bandgap in metal oxides and enhance additional properties.[30] The most commonly used metal dopants are transition metals, post-transition metals, alkaline earth metals, and rare earth metals.[72,87−89] Among transition metals, first-row transition metals as well as d^8 and d^9 transition metals are most commonly employed, where the 3d orbitals of the dopant metal introduce electronic states in between the original bandgap.[90] Metal ion dopants can also induce defects and changes in the diffusion behavior,[91] which can enhance charge transport and electron mobilities, boosting electrical performance.[92] Cation doping in tin oxide with

https://dx.doi.org/10.1021/acsanm.0c01035
ACS Appl. Nano Mater. 2020, 3, 6156−6185

Table 1. List of Visible-Light-Active Doped Metal Oxide Nanoparticles along with Their Synthetic Method, Morphology, Optical Properties, and Applications

parent metal oxide	dopant	synthesis method	morphology	size/aspect ratio	visible light properties	application	ref
TiO_2	C	hydrothermal	nanorods	100 nm: 1.5−3.6 μm	bandgap narrowing −2.7 eV broad absorption band until 800 nm	organic pollutant degradation	Shao et al.[109]
TiO_2	C	hydrothermal	nanotubes, nanowires, nanorods	7−15 nm: > 100 nm	bandgap narrowing −2.9 eV broad absorption tail until 700 nm	degradation of VOCs	Wu et al.[65]
TiO_2	C	hydrothermal	nanowires	60−100 nm: 1−10 μm	broad absorption tail until 800 nm		Kiran et al.[110]
TiO_2	C, N, S	solution reflux	hollow nanospheres	200 nm	absorption tail until 550 nm	dye degradation	Lin et al.[76]
TiO_2	N	sol−gel	hollow nanospheres	∼500 nm	absorption tail until 800 nm		Qiao et al.[111]
TiO_2	N	solvothermal		9−16 nm	absorption tail until 600 nm	dye degradation	Yang et al.[112]
TiO_2	N	rapid breakdown anodization	nanotubes		bandgap narrowing −2.9 eV	H_2 production from water splitting	Preethi et al.[113]
TiO_2	N	sol−gel, thermal ammonolysis	nanospheres, nanorods	25 nm, 28:170 nm	broad absorption tail until 825 nm	O_2 evolution from water	Lee et al.[64]
TiO_2	N	solution reflux	mesoporous nanospheres	400−600 nm	absorption tail until 700 nm	dye degradation	Li et al.[114]
TiO_2	N, S	hydrothermal	spherical aggregates	>500 nm	bandgap narrowing −2.3 eV	dye degradation	Albrbar et al.[74]
TiO_2	N, Zr	solution-based			absorption tail until 800 nm	organic pollutant degradation	Zhang et al.[99]
TiO_2	N, Cu	sol−gel	nanospheres	∼120 nm	bandgap narrowing −2.0 eV	organic pollutant degradation	Jaiswal et al.[85]
TiO_2	N, F	oleic acid/oleylamine method	nanorods, nanocubes, nanodiamonds	2−3 nm: 25−35 nm	broad absorption peak until 800 nm	cell labeling, cell death	Biswas et al.[115]
TiO_2	N, F	sol−gel			absorption tail until 500 nm	degradation of cyanotoxins	Palaez et al.[116]
TiO_2	I	hydrothermal	nanospheres	<20 nm	absorption tail until 550 nm	CO_2 reduction	Zhang et al.[117]
TiO_2	Ti^{3+}	hydrothermal	irregular	60−170 nm	absorption band increasing 500−700 nm	H_2 production from CH_3OH	Zuo et al.[118]
TiO_2	Ti^{3+}	plasma spray	irregular	<500 nm	bandgap narrowing −2.9 eV absorption tail until 800 nm	dye degradation, antibacterial	Kumar et al.[119]
TiO_2	Ti^{3+}	solvothermal	irregular, nanocuboids	50 nm, 20:100 nm	absorption band increasing 500 − 800 nm	dye degradation	Zhou et al.[120]
TiO_2	Ti^{3+}	sol−gel, alkaline hydrothermal	nanorods	100−350 nm: 0.5−2 μm	bandgap narrowing −2.6 eV absorption band increasing 400 − 800 nm	H_2 production from water splitting	Zhang et al.[121]
TiO_2	V	polyol method	irregular	12 nm	bandgap narrowing −2.6 eV absorption tail until 800 nm	dye degradation	Belfaa et al.[100]
TiO_2	V	sol−gel	irregular	10−15 nm	bandgap narrowing −1.7 eV absorption tail until 700 nm	industrial pollutant degradation	Takle et al.[122]
TiO_2	V	hydrothermal	nanorods	∼15:150 nm	broad absorption peak until 850 nm	dye degradation	Li et al.[123]
TiO_2	Cr	hydrothermal	nanorods	20−50 nm: 0.2−1 μm	absorption tail until 800 nm	photocurrent generation	Zhu et al.[124]
TiO_2	Cr	flame spray pyrolysis	nanospheres	3−30 nm	broad absorption peak until 600 nm	organic pollutant degradation	Tian et al.[125]
TiO_2	Cr, V, Mn, Fe, Co, Ni, Cu, Mo	oleic acid/oleylamine method	nanorods	4:30−50 nm	absorption tail until 600 nm	H_2 production from CH_3OH	Zhang et al.[96]
TiO_2	Co, Fe, Zn, Al	template synthesis	hollow nanospheres	300 nm	absorption tail until 800 nm	dye degradation	Peng et al.[87]
TiO_2	Fe	solution-based	irregular	35−70 nm	absorption tail until 500 nm	dye degradation	Eshaghi et al.[126]
TiO_2	Fe	oleic acid/oleylamine method	nanospheres, nanorod-clusters	9 nm, NR diameter: 10 nm	absorption tail until 600 nm	degradation of VOCs	Liu et al.[127]
TiO_2	Fe	sol−gel	nanocubes	9 nm	absorption tail until 650 nm	organic pollutant degradation	Wu et al.[128]
TiO_2	Fe	hydrothermal	nanospheres	150−500 nm	absorption tail until 550 nm	dye degradation	Tong et al.[129]
TiO_2	Co	biosynthesis	irregular	∼9 nm	bandgap narrowing −1.7 eV broad absorption peak until 800 nm	anode for Li-battery	Kashale et al.[130]

https://dx.doi.org/10.1021/acsanm.0c01035
ACS Appl. Nano Mater. 2020, 3, 6156−6185

Table 1. continued

parent metal oxide	dopant	synthesis method	morphology	size/aspect ratio	visible light properties	application	ref
TiO_2	Co	sol−gel	irregular	∼20 nm	bandgap narrowing −1.9 eV broad absorption peaks until 750 nm		Khurana et al.[131]
TiO_2	Cu	alkaline hydrothermal	nanotubes	9:>100 nm	absorption tail until 500 nm Absorption Band at 600 − 800 nm	self-cleaning glass surfaces, degradation of carcinogens	Miyauchi et al.[132]
TiO_2	Zn, Mn	sol−gel	irregular	15−50 nm	absorption tail until 800 nm	dye degradation	Benjwal et al.[83]
TiO_2	Zn, Mn	solvothermal hydrothermal	nanospheres, nanorods	100−250 nm, 50:200 −10 000 nm	broad absorption peak until 800 nm	dye degradation	Benjwal et al.[133]
TiO_2	Nb	sol−gel	irregular	<20 nm	absorption tail until 600 nm	organic/inorganic pollutant degradation	Lim et al.[134]
TiO_2	Nb, Mo, W	oleic acid/oleylamine method	nanocrystals	6−12 nm	LSPR absorption between 500−2000 nm		Cao et al.[135]
TiO_2	Zr	sol−gel	nanocrystals	3−30 nm	absorption tail until 350 nm	dye degradation	Chang et al.[136]
TiO_2	Zr, Ag	sol−gel		6−20 nm	bandgap narrowing −2.8 eV	dye degradation, antibacterial	Naraginti et al.[137]
TiO_2	Ag	sol−gel	irregular	∼9 nm	bandgap narrowing −2.5 eV broad absorption peak until 700 nm	dye degradation, antibacterial	Ali et al.[138]
TiO_2	Pt	sol−gel	irregular	<33 nm	bandgap narrowing −2.7 eV absorption tail until 600 nm	organic pollutant degradation	Kim et al.[66]
TiO_2	Bi	polyol	nanospheres	87−117 nm	broad absorption peak until 600 nm	dye degradation	Li et al.[139]
TiO_2	Bi	hydrothermal	nanocubes	∼92 nm	absorption tail until 800 nm	photocurrent generation	An'amt et al.[88]
TiO_2	Ce	hydrothermal	nanospheres	100−500 nm	absorption tail until 500 nm	dye degradation	Tong et al.[140]
TiO_2	Er	sol−gel	irregular	13−20 nm	sharp additional peaks from rare earth transitions	degradation of VOCs	Rao et al.[141]
ZnO	C	solid state reaction	nanorods, nanospheres	∼200 nm	absorption band until 600 nm	dye degradation	Zhang et al.[142]
ZnO	N	sol−gel	irregular	80−100 nm	bandgap narrowing −2.9 eV	degradation of herbicides	Macías-Sánchez et al.[75]
ZnO	N	paper-mediated template	irregular	20−30 nm	bandgap narrowing −2.97 eV absorption tail until 700 nm	dye degradation	Kale et al.[143]
ZnO	Mg	co-precipitation	irregular	30−100 nm	bandgap narrowing −3.0 eV	dye degradation, antibacterial	Pradeev raj et al.[72]
ZnO	Mg	co-precipitation	nanospheres	∼50 nm	absorption tail until 550 nm	dye degradation	Etacheri et al.[144]
ZnO	Al	sol−gel	irregular		absorption tail until 800 nm		Khan et al.[145]
ZnO	Mn	solvothermal	nanospheres	21 nm	broad absorption tail until 800 nm	dye degradation	Achouri et al.[73]
ZnO	Mn	co-hydrolysis		21−73 nm	absorption tail until 650 nm	dye degradation	Ullah et al.[146]
ZnO	Fe	hydrothermal	nanoflowers		broad absorption peak at 500 extending until 700 nm	gas sensing	Han et al.[147]
ZnO	Co	co-precipitation	nanospheres	40−50 nm	bandgap narrowing −2.8 eV broad absorption peaks 500−700 nm	photodetectors, photocurrent generation	Jacob et al.[148]
ZnO	Co	microwave-assisted	irregular	∼10 nm	broad absorption peaks 500−700 nm		Bilecka et al.[149]
ZnO	Cu	co-hydrolysis	mesoporous nanospheres	∼150 nm		antibacterial, cell death	Gupta et al.[150]
ZnO	Cu	co-precipitation	irregular	40−85 nm	absorption tail until 550 nm	H_2 production from H_2S	Kanade et al.[151]
ZnO	Cu	antisolvent	elliptical nanocrystals	50−200:500 nm	broad absorption band 350−800 nm	photocurrent generation	Lu et al.[152]
ZnO	Ag	sol−gel	irregular		band edge narrowing to 450 nm	antibacterial	Nigussie et al.[153]

https://dx.doi.org/10.1021/acsanm.0c01035
ACS Appl. Nano Mater. 2020, 3, 6156−6185

Table 1. continued

parent metal oxide	dopant	synthesis method	morphology	size/aspect ratio	visible light properties	application	ref
ZnO	Dy	sono-chemical	nanospheres	~38 nm		dye degradation	Khataee et al.[154]
ZnO	Sm	gel-combustion	nanospheres	~30 nm	absorption tail until 600 nm	industrial pollutant degradation	Faraz et al.[84]
$SrTiO_3$	S, N	solid state reaction	irregular	20−200 nm	absorption tail until 600 nm	removal of NO	Wang et al.[86]
$SrTiO_3$	Ag	hydrothermal	nanocubes	~32 nm	broad absorption peak at 450 nm until 800 nm	removal of NO	Zhang et al.[155]
$SrTiO_3$	Ru, Ni	solution-based	nanocubes	5−20 nm	bandgap narrowing −1.9 eV broad absorption peaks until 700 nm	dye degradation	Joseph et al.[156]
$SrTiO_3$	Rh	hydrothermal	nanocubes/ nanospheres	20−50 nm	broad absorption peak until 550 nm	antibacterial, dye degradation	Kiss et al.[157]
$SrTiO_3$	Rh, La	solid state reaction	irregular	<300 nm	broad absorption peak at 580 nm −800 nm	H_2 production from CH_3OH, water splitting	Wang et al.[97]
$SrTiO_3$	La, Cr	microwave-assisted	nanocubes	60 nm	bandgap narrowing −2.8 eV broad absorption peaks until 700 nm	H_2 production from CH_3OH	Cai et al.[98]
$BaTiO_3$	Ce	hydrothermal	nanospheres	109−127 nm		PEC water splitting	Senthilkumar et al.[158]
$BaTiO_3$	Rh	hydrothermal	nanocubes	100−250 nm	absorption tail until 550 nm	H_2 production from CH_3OH	Nishioka et al.[159]
$NaTaO_3$	C	solvothermal			absorption tail until 550 nm	decomposition of NO_x	Wu et al.[160]
$NaTaO_3$	S	hydrothermal	nanocubes	200−500 nm	absorption tail until 600 nm	organic pollutant degradation	Li et al.[161]
$NaNbO_3$	N	solid state reaction	irregular	200−700 nm	absorption tail until 500 nm	organic pollutant degradation	Shi et al.[162]
$BaTaO_3$	N	polymerizable complex, thermal ammonolysis	nanospheres	~100 nm	absorption tail until 700 nm	H_2, O_2 evolution from water splitting, photocurrent generation	Maeda et al.[163]
$LaCoO_3$	C	microorganism chelation			broad absorption until 800 nm	CO_2 reduction	Jia et al.[25]
$Sr_5Ta_4O_{15}$	N	polymerizable complex, thermal ammonolysis	irregular	50−100 nm	broad absorption until 600 nm	H_2, O_2 evolution from water splitting	Chen et al.[164]
ZrO_2	C, N, S, Eu	solution-based	nanospheres	8−30 nm	broad absorption peaks increasing until 800 nm	dye degradation	Agorku et al.[165]
ZrO_2, HfO_2	N	co-hydrolysis		5−50 nm	absorption tail until 1000 nm	dye degradation	Qiu et al.[166]
CeO_2	Sm, Gd, Pr, Tb	sol−gel		30−50 nm	broad absorption peak until 800 nm		Guo et al.[89]
SnO_2	Zn, Sb	hydrothermal	nanospheres	31−39 nm	absorption tail until 700 nm		Medhi et al.[107]
$ZnFe_2O_4$	Co	hydrothermal	nanospheres	10−30 nm	broad absorption peak until 800 nm	organic pollutant degradation, dye degradation	Fan et al.[108]
CoO/ Co_3O_4	S	oleic acid/oleylamine method	nanocubes	9 nm		CO_2 reduction	Choi et al.[23]

https://dx.doi.org/10.1021/acsanm.0c01035
ACS Appl. Nano Mater. 2020, 3, 6156−6185

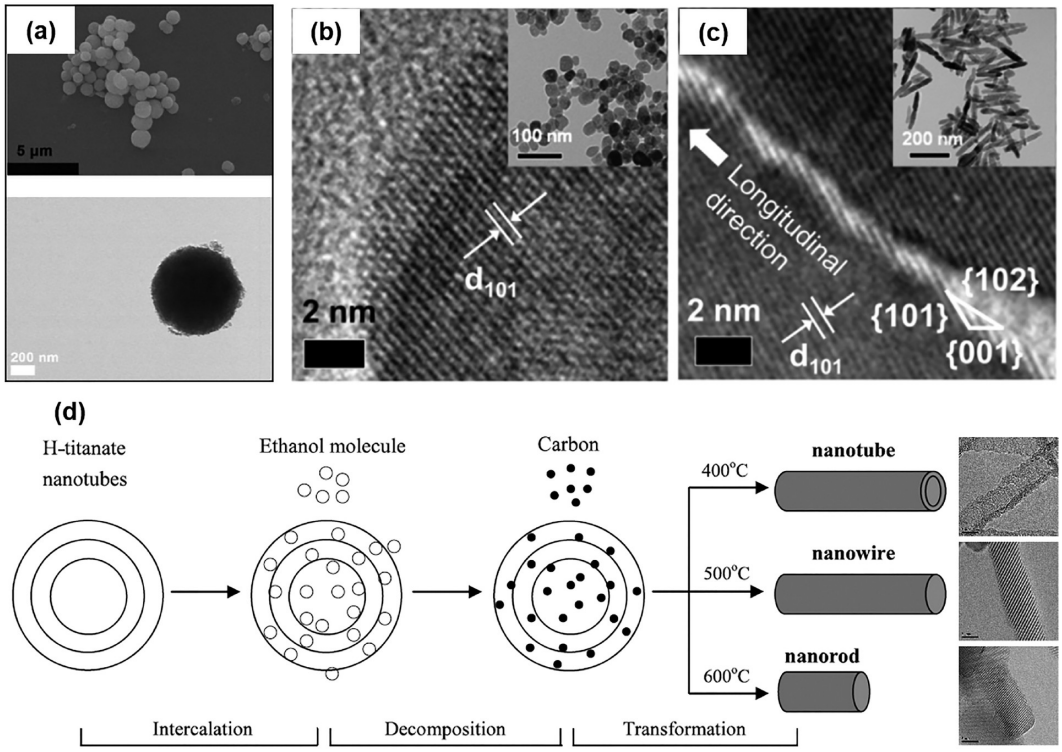

Figure 3. Morphology of nonmetal doped TiO_2 NPs. (a) SEM and TEM images of mesoporous N-doped TiO_2 NPs. Adapted with permission from ref 114. Copyright 2015 Elsevier. (b, c) HRTEM and TEM images (inset) of N-doped TiO_2 nanospheres and nanorods, respectively. Adapted with permission from ref 64. Copyright 2014 Elsevier. (d) Synthesis scheme and HRTEM images for C-doped TiO_2 NTs, NWs, and NRs (scale bar: 5 nm). Adapted with permission from ref 65. Copyright 2009 IOP Publishing, Ltd.

antimony and zinc, for example, leads to enhanced conductivity and thermal stability.[93−95] Cation doping can also further activate a surface for use in catalytic reactions.[44] Similar to nonmetal doping, codoping and tridoping different metals as well as a mixture of metals with nonmetals have been more effective than monodoping, in certain cases, for enhancing visible-light absorption.[96−99]

The most commonly employed doped metal oxides have been doped titanium dioxide, doped zinc oxide, doped tin oxide, doped mixed-titanates, perovskites, doped spinel oxides, doped ceria, doped zirconia, and doped iron oxide nanoparticles. Notwithstanding, TiO_2 and ZnO have been the pioneering materials in the field of doped metal oxides nanoparticles.[100] Titanium and zinc oxides have been utilized for the synthesis of acoustic devices, solar cells, piezoelectric devices, thin-film transistors (TFTs), textiles, rubber products, LEDs, laser diodes, chemical and biosensors, and as antibacterial and antifungal agents.[11,12,101−104]

Research in the field of bandgap engineering via doping basically started when the bandgap of TiO_2 was improved upon doping by nitrogen in studies by Asahi et al. in 2001.[105] Since then, there have been multiple reports of doped titanium dioxide powders. The ones featuring nanosized particles sensitive to visible light are discussed in detail in the following sections. Zinc oxide has been mainly doped to produce films for use as transparent conducting electrodes;[3] however, there are quite a few reports of doped zinc oxide nanoparticles as well. Compared to TiO_2, studies of doped ZnO have centered largely on the synthesis of uniform spherical nanoparticles, as described in later sections. However, doping in colloidal 1D nanostructures like nanorods (NRs), nanowires (NWs), and nanotubes (NTs), which enables a long lifetime for photogenerated charge carriers, are more widely utilized for TiO_2 compared to ZnO.[64] Recently, many studies have centered on more promising titanates like $BaTiO_3$ and $SrTiO_3$ along with mixed tantalum oxides, niobium oxides, and $BiVO_4$.[12,106] Doped tin oxides have been almost exclusively studied as thin films.[93−95] New research, however, is now starting to focus on visible-light-active nanoparticles of doped tin and iron oxides.[107,108] Some magnetic metal oxide nanoparticles have also been modified by doping to fabricate magnetically separable visible-light-active photocatalysts.[108]

Table 1 lists the various visible-light-active metal oxide nanostructures and their corresponding dopants that are covered in this review. A brief description of their primary application is also provided. While there have been many reports of the synthesis and study of photoactive doped metal oxide nanoparticles, only the ones demonstrating visible-light activity will be discussed within the scope of this review.

4. DOPED TITANIUM DIOXIDE (TiO_2) NANOPARTICLES

4.1. Synthesis and Structure of Doped TiO_2 Nanoparticles. *4.1.1. Nonmetal Doped TiO_2 Nanoparticles.* The most typical methods used for the synthesis of doped TiO_2 nanoparticles are sol−gel and hydrothermal methods, predominantly yielding anatase-phase TiO_2. The most commonly used titanium precursors are titanium butoxide (also known as tetrabutyl orthotitanate, TBOT), titanium(IV) isopropoxide (TTIP), and $TiCl_4$. Water, ethanol, and isopropanol are the most common solvents used for these reactions. Nitrogen is the most common dopant or codopant used in TiO_2 nanoparticles. Yang et al. prepared N-doped visible-active TiO_2 by using a solvothermal method, with a 0.5−2.0 molar

https://dx.doi.org/10.1021/acsanm.0c01035
ACS Appl. Nano Mater. 2020, 3, 6156−6185

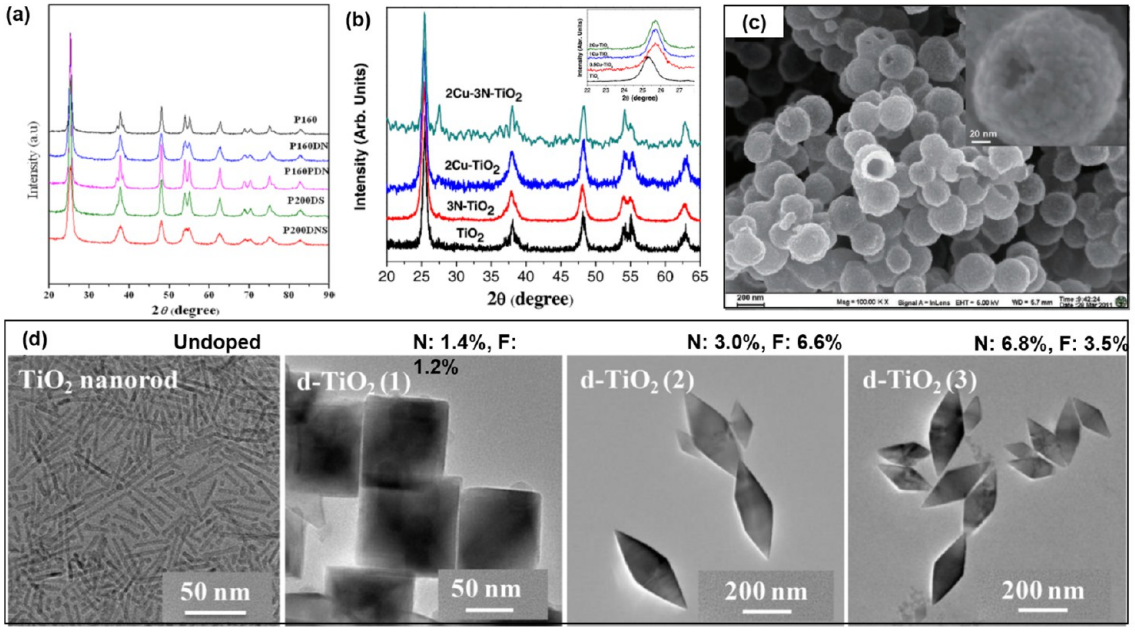

Figure 4. Structure and morphology of nonmetal codoped and tridoped TiO_2 NPs. (a) XRD patterns of TiO_2 powders (P160) doped with nitrogen (P160 DN, P160PDN-annealed in air), doped with sulfur (P200DS) and codoped with nitrogen and sulfur (P200DNS). Adapted with permission from ref 74. Copyright 2016 Elsevier. (b) XRD patterns of TiO_2 NPs doped with Cu and N (inset shows shift on Cu doping). Adapted with permission from ref 85. Copyright 2015 Elsevier. (c) SEM image of C, N, and S tridoped TiO_2 NPs. Adapted with permission from ref 76. Copyright 2013 Elsevier. (d) TEM images of N and F codoped TiO_2 NPs synthesized from TiO_2 NRs. Adapted with permission from ref 115. Copyright 2017 American Chemical Society.

ratio doping of nitrogen to titanium.[112] TBOT and ethylenediamine were used as the precursors. The nitrogen-doped TiO_2 nanoparticles adopted the anatase phase. Multiple theoretical studies have been conducted to determine the exact nature of nitrogen doping in both rutile- and anatase-phase TiO_2. Although one would assume the nitrogen typically substitutes at the oxygen site, it has been observed that the neutral nitrogen substituting the Ti site has the lowest energy of formation; spectroscopy data also seem to suggest the same, as discussed in more detail in a later section.[77] Literature reports indicate a greater ease in synthesizing hollow, porous, or mesoporous doped TiO_2 nanospheres as compared to solid nanoparticles. Li et al. reported uniform mesoporous spheres of N-doped TiO_2, as shown in Figure 3a, synthesized by using PVP as a dispersant and CTAB as a soft template.[114] The as-prepared mesoporous TiO_2 was subjected to a hydrothermal process at 180 °C for 2h with ammonia to obtain mesoporous N-doped TiO_2 spheres.

For the synthesis of colloidal 1D doped TiO_2 nanostructures, various strategies have been utilized. For example, Lee et al. employed a sol−gel technique followed by calcination under an NH_3 flow to selectively synthesize N-doped nanospheres and nanorods.[64] This technique for N-doping is commonly referred to as "thermal ammonolysis". Similarly, an aqueous solution of TTIP and triethanolamine was mixed with oleic acid or ethylenediamine, respectively, to obtain nanospheres or nanorods. As shown in Figures 3b, c, the nanospheres had a uniform diameter around 24 nm, while the nanorods had a width of about 28 nm and a length of about 170 nm. Preethi et al. utilized a unique rapid breakdown anodization (RBA) technique to obtain anatase−rutile−brookite polymorphous N-doped (0.5−4.5%) TiO_2 nanotubes.[113] The percentage of brookite phase gradually decreased from 29% with increased N-doping and disappeared for the 4.5% doped sample. A separate study of mixed brookite phase doped TiO_2 nanoparticles was reported by Zhang et al.[117] Instead of rutile−brookite, Zhang et al. prepared mixed anatase−brookite phase spherical TiO_2 nanoparticles doped with iodine. The brookite content increased with higher doping percentage;[117] upon increasing the calcination temperature from 375 to 550 °C, the rutile phase also began to appear.

Another predominant nonmetal dopant for TiO_2 is carbon. Although carbon is more effective in activating visible-light properties in spherical nanoparticles as a codopant (as discussed in the next section), it can effectively activate visible-light activation in 1D nanostructures as a monodopant. One of the most common methods for 1D TiO_2 nanoparticle synthesis is the alkaline hydrothermal method, where a TiO_2 powder is mixed in a sodium hydroxide solution and subjected to hydrothermal treatment in a Teflon-lined autoclave at temperatures of 120 °C and above. Wu et al. utilized this method to prepare TiO_2 nanotubes.[65] These nanotubes were then exposed to ethanol and then calcined at 400, 500, and 600 °C to obtain C-doped nanotubes, nanowires, and nanorods, respectively. Nanotubes are hollow 1D structures; therefore, when subjected to calcination at a higher temperature, they first collapse to form solid nanowires (at 500 °C) and are subsequently truncated to yield shorter nanorods (at 600 °C), as illustrated in Figure 3d. All three samples adopted the anatase phase. Shao et al. obtained rutile phase C-doped (5−16%) TiO_2 nanorods using a similar multistep method.[109] Cationic polystyrene spheres were used as a spherical template with TBOT in a sol−gel process to first obtain core−shell TiO_2 nanospheres. These core−shell nanospheres were then subjected to hydrothermal treatment at 180 °C, whereby these spheres fused into a sol and subsequently broke down to C-doped nanorods. Further calcination at 450 °C afforded single crystalline C-doped nanorods. Kiran et al. utilized an

https://dx.doi.org/10.1021/acsanm.0c01035
ACS Appl. Nano Mater. 2020, 3, 6156−6185

alternative approach to prepare C-doped TiO_2 nanowires starting from TiC powder.[110] After subjecting the starting materials to hydrothermal treatment in NaOH at 160 °C for 144 h, further annealing at 350 °C for 5 h converted the TiC powder to TiO_2 (anatase) nanowires.

4.1.2. Nonmetal Codoped and Tridoped TiO_2 Nanoparticles. Nitrogen is often employed as a codopant with other nonmetals or metals rather than as a monodopant because nitrogen is more effective as a codopant for visible-light activity, as discussed in more detail in the next section. The nitrogen-doping process for codoping is similar to that of monodoping. For example, ethylenediamine was used by Palaez et al. to achieve nitrogen codoping with fluorine, with the fluorine and titanium precursor being the fluoro-surfactant Zonyl FS-300 and TTIP respectively.[116] The combination of N and Ti atoms form a coordination compound around the fluoro-surfactant micelle, creating an inorganic−organic composite. Upon heating, the fluoro-surfactant is removed, and the fluorine atoms diffuse into the TiO_2 lattice. In separate studies, Albrbar and coworkers synthesized nitrogen and sulfur codoped TiO_2.[74] The gel synthesized with the sulfur precursor (dimethyl sulfoxide, DMSO) was annealed in ammonia. The method has been described as a nonhydrolytic sol−gel process. Crystal growth was observed to be better when annealed in air, compared to ammonia, which induced nitrogen doping, decreasing crystallite size (Figure 4a). Sulfur doping also causes a decrease in the crystallite size, consistent with a general process in which inhibition of crystallite growth during gel annealing occurs in the presence of dopants, as shown in Figure 4a.

Nonmetal tridoping has also been achieved with porous TiO_2 NPs (Figure 4c). Well-defined porous spherical C-, N-, and S-tridoped TiO_2 nanoparticles were prepared by Lin et al. by using thiourea as C, N, and S precursor along with $Ti(OBu)_4$.[76] Upon increasing the molar ratio of thiourea to TiO_2, there was a decrease in crystallite size and an increase in the BET (Brunauer−Emmett−Teller) surface area and pore volume. Inhibition of crystal growth and increased surface area in TiO_2 upon doping with nitrogen and sulfur have also been observed in microstructured photocatalysts.[38,40]

Nitrogen is also commonly codoped with metals. Nitrogen codoping with copper in TiO_2 NPs was achieved by Jaiswal et al. by mixing trimethylamine and copper(II) nitrate precursors with the titanium precursor TBOT.[85] Doping ratios were varied between 0.5−2% and 1−3% for copper and nitrogen, respectively. The anatase phase is preserved under these doping conditions; however, incorporation of copper shifted the main anatase peak to higher 2θ values because the Cu^{2+} ion is bigger than the Ti^{4+} ion (Figure 4b inset). Codoping nitrogen and copper, however, leads to the formation of some rutile phase (Figure 4b), as the larger Cu^{2+} replaces Ti^{4+} and N^- replaces O^{2-}, leading to oxygen vacancies and allowing the rearrangement of Ti^{4+} and O^{2-} ions in the lattice to the rutile phase. Zr^{4+} ions can also replace Ti^{4+} in the anatase phase to about 20% by using $ZrOCl_2$ as the zirconium dopant precursor with TBOT, as demonstrated by Zhang et al.[99] In addition to zirconium monodoping, these researchers also codoped zirconium with nitrogen by using ammonia as an added precursor.

In separate studies,[115] Biswas et al. adopted the oleic acid and oleylamine method, typically used for the synthesis of iron oxide and indium oxide nanoparticles,[70,71] to prepare TiO_2 nanorods. These nanorods were then codoped with nitrogen and fluorine using ammonium fluoride and urea to yield 1−7% codoped nanocubes and nanodiamonds, with sizes ranging between 70−225 nm (see Figure 4d).[115]

4.1.3. Metal Doped TiO_2 Nanoparticles. Among purely metal cation-doped TiO_2 NPs, the most uniform particles were obtained upon doping with bismuth. Highly uniform solid particles with sizes that could be tailored between 117 and 87 nm were synthesized by Li et al. with Bi-doping up to 2.2% (Figure 5a).[139] The doping process and further calcination at

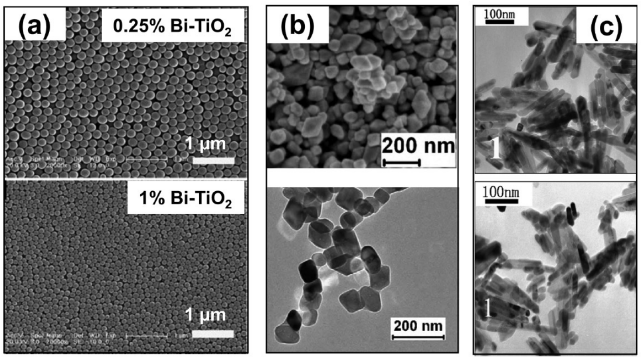

Figure 5. Morphology of metal-doped TiO_2 NPs. (a) SEM images of solid spherical Bi-doped TiO_2 NPs. Adapted with permission from ref 139. Copyright 2009 John Wiley and Sons. (b) SEM and TEM images of Bi-doped TiO_2 nanocubes. Adapted with permission from ref 88. Copyright 2010 Elsevier. (c) TEM images of $V^{4+/5+}$-doped TiO_2 NRs. Adapted with permission from ref 123. Copyright 2009 Elsevier.

450 °C led to crystallization of the nanoparticles into the anatase phase without any deformation of the particles. Similarly, relatively uniform nanocubes with ∼100 nm dimensions were prepared by An'amt et al. using Bi-doping (Figure 5b).[88] Mixing the nitrate salt of bismuth with TTIP and triethanolamine in a sol−gel hydrothermal reaction at 180 °C for 72 h afforded the Bi-doped uniform nanocubes.

Transition metals are also commonly doped into TiO_2 nanoparticles. For instance, iron was monodoped into TiO_2 using $FeCl_3$ with TTIP solution as precursors using coprecipitation by Eshaghi et al.[126] The same group also synthesized Fe-doped TiO_2 on activated carbon. Another example of a transition metal dopant is the Pt-doped TiO_2 studied by Kim et al.[66] In this example, Ti^{4+} ions were substituted by Pt^{4+} ions, and the material exhibited both anatase and rutile phases. A sol−gel synthesis method was used with TTIP and H_2PtCl_6 as the precursors. Acidic conditions and calcination temperatures between 373 and 873 K were used. Ali et al. synthesized 4.0 mol % Ag monodoped anatase TiO_2 NPs using $AgNO_3$ with TTIP and a calcination temperature of 400 °C.[138] Because Ag^+ (1.26 Å) is more than twice the size of Ti^{4+} (0.60 Å), introduction of the dopant ions causes lattice strain and a decrease in crystallite size when doped in low concentrations, but this lattice strain diminished at higher Ag^+ doping concentration. Sol−gel synthesis under acidic conditions and calcination methods were also used by Lim et al. to dope TiO_2 with niobium.[134] Controlled hydrolysis of titanium butoxide (TBOT) via an esterification reaction between acetic acid and ethanol, followed by hydrothermal treatment in the presence of nitrate salts of Fe and Ce, were used by Tong et al. to synthesize Fe- and Ce-doped TiO_2 nanospheres, respectively, having diameters of 100−500 nm.[129,140] In contrast, a similar method with TBOT and

https://dx.doi.org/10.1021/acsanm.0c01035
ACS Appl. Nano Mater. 2020, 3, 6156−6185

$Fe(NO_3)_3$ in the absence of acetic acid yielded much smaller Fe-doped TiO_2 nanocubes (~9 nm).[128] A limited number of literature examples report the synthesis of V-doped TiO_2 NPs. Belfaa et al. used ammonium methavanadate and $TiCl_4$, while Takle et al. used TTIP and V_2O_5 as the precursors.[100,122] The former used a polyol method while the latter used a sol−gel method. Both studies employed a calcination step around 400−500 °C, which appears to be the standard calcination temperature range used by all groups for doped TiO_2 synthesis. Belfaa et al. observed a consistent anatase phase with just a slight decrease in lattice parameters upon increased V doping, while Takle et al. noticed a preference for the rutile phase over the anatase phase upon increasing V doping.[100,122] These studies offer another indication that the use of different synthesis routes has a significant impact on the adopted crystalline structure as well as the morphology.[128,129,140]

As we have noted, titanium alkoxides such as titanium butoxide (TBOT) and titanium isopropoxide (TTIP) are popular precursors for the synthesis of doped TiO_2 nanoparticles. Another titanium alkoxide used for doped TiO_2 synthesis is titanium ethoxide (TEO). For example, Cao et al. prepared Mo- and W-doped TiO_2 nanocrystals via hydrolysis of the chloride salts of the dopants in 1-octadecene solvent with oleic acid and oleylamine as cosurfactants.[135] The size of the resulting nanocrystals were varied (12.1 ± 2.3, 8.6 ± 1.1, and 5.8 ± 0.9 nm) simply by varying the amounts of the two surfactants in the synthesis. The typical reaction temperature of 280−290 °C for oleic acid−oleylamine-based recipes was also employed here, and the resultant doped nanocrystals directly adopted crystalline anatase phase without any calcination steps. This recipe could also be employed for gram-scale production of the doped-TiO_2 nanocrystals (with dopant ratio of M/Ti = 0.1). This one-pot synthesis method produced M-doped TiO_2 nanocrystals in high yield (>86%), and the nanocrystal dispersions were stored for at least six months without changes to the dispersion quality, holding great promise for industrial production.

Metal ions have also been doped into colloidal 1D TiO_2 nanostructures. A single-step hydrothermal reaction was utilized by Li et al. to prepare uniform $V^{4+/5+}$-doped TiO_2 nanorods.[123] There was little or no effect on the uniform morphology of the nanorods at 1 wt % doping, as illustrated in Figure 5c; the nanorods adopted a rutile phase. As discussed earlier, the alkaline hydrothermal method is the most common method for the synthesis of doped 1D TiO_2 NPs. This method was utilized by Miyauchi et al. to prepare Cu-doped TiO_2 nanotubes starting from a TiO_2 powder and copper chloride along with sodium hydroxide at 120 °C;[132] this method also afforded rutile-phase nanorods. Using this method, chromium was similarly doped into TiO_2 nanorods at 1−10% using a chromium nitrate salt at 180 °C.[124] Cr-doped TiO_2 nanoparticles with mixed anatase−rutile phase were also synthesized by Tian et al. using a flame-spray pyrolysis method.[125] Oleic acid and oleylamine are widely used in the synthesis of iron and indium oxides, as these surfactants offer great control over morphology and size.[70,71] A modified version of this method was used by Liu et al. to synthesize 400 nm Fe-doped spherical clusters comprised of individual nanorods, each with a 10 nm diameter and a porous structure with high surface area.[127] A mixture of TTIP and ferric nitrate was used with oleic acid and oleylamine in a Teflon-lined steel autoclave at 180 °C. In separate studies, Kashale et al. utilized a green biosynthesis approach to prepare Co-doped TiO_2 nanoparticles from the chloride precursors of Ti and Co.[130] The protocol is similar to a sol−gel method but involves substitution of typical sol−gel solvents with a gram bean extract. The gram bean extract contains pectin, a complex polysaccharide present in most primary cell walls, which acts as a natural capping agent, hindering aggregation. Conventional sol−gel methods can also be used to synthesize Co-doped TiO_2 nanoparticles, as shown by Khurana et al.[131]

4.1.4. Transition Metal Codoped TiO_2 Nanoparticles. Zn and Mn codoped TiO_2 NPs were synthesized by Benjwal et al. using the nitrates of Zn and Mn along with TBOT and annealed at 500 °C.[83] Increasing the amount of Zn^{2+} and Mn^{2+} doping favored the anatase phase while inhibiting the formation of other phases (i.e., brookite and rutile). Despite a variation in ionic size, Zn^{2+} and Mn^{2+} can replace Ti^{4+} as the Zn−O and Mn−O bond lengths (~1.93 Å) are quite similar to the Ti−O bond length (~2.03 Å) in a distorted octahedral geometry. In a more recent study using the same precursors, Benjwal et al. observed that solvothermal methods afforded anatase-phase Zn and Mn codoped nanospheres, while hydrothermal methods generated anatase−rutile−brookite triphasic nanorods.[133] Zr-doped anatase TiO_2 nanoparticles were synthesized by Naraginti et al. by using $ZrO(NO_3)_2$ and TTIP as zirconium and titanium precursors, respectively.[137] The same group also codoped the zirconium with silver using $AgNO_3$ and calcined at 450 °C to obtain nanoparticle powders, 7 to 19 nm in diameter. Analysis by EDX showed near stoichiometric ratios for $AgTiO_2$ (1:1:2) and $ZrAgTiO_2$ (1:1:1:2).

Similar to anion doping, there has been considerably more success in the uniform preparation of transition metal-doped mesoporous or hollow particles compared to solid particles. Peng et al. synthesized hollow TiO_2 spheres with 250 nm diameters doped with Co, Fe, Al, as well as codoped with Co/Zn, Co/Al, and Al/Fe (see Figure 5c).[87] As shown in the TEM images in Figure 5c, the particles retain their shape and dispersity even after doping. To synthesize the aforementioned particles, a spherical polystyrene core was used as a template for the synthesis of PS/TiO_2 hybrid particles. These hybrid particles were then treated with the desired transition metal salts in a solution of citric acid and polyethylene glycol (PEG), dried, and then further annealed at 600 °C and above to yield the hollow doped TiO_2 particles. Transition metal doping, codoping, and tridoping was carried out in TiO_2 nanorods by Zhang et al. (see Figure 6b).[96] A Ti-oleate precursor was mixed with the dopant M-oleate precursor (M = V, Cr, Mn, Co, Ni, Cu, or Mo) and heated to 290 °C followed by the injection of additional aliquots of the two oleate precursors. This methodology was adapted from the Hutchinson group method, which is now widely used for the synthesis of ITO (tin-doped indium oxide) nanospheres and nanocubes.[71,167,168] This method is popular in doped metal oxide nanoparticle synthesis as it yields uniform nanoparticles with good control over morphology. Mono-, co-, and tridoping with various doping percentages, up to 10%, was achieved simply by varying the mixing ratio of Ti-oleate and M-oleate precursors. As shown in Figure 6b, the morphology is well-maintained, even for the codoped and tridoped nanorods. This method has great promise to facilitate the preparation and study of tailored metal doped TiO_2 nanospheres and nanocubes.

4.1.5. Ti^{3+} Self Doped TiO_2 Nanoparticles. Some studies have explored the synthesis of TiO_2 nanoparticles self-doped with Ti^{3+} ions; for example, Zuo et al. doped Ti^{3+} into TiO_2 by

https://dx.doi.org/10.1021/acsanm.0c01035
ACS Appl. Nano Mater. 2020, 3, 6156−6185

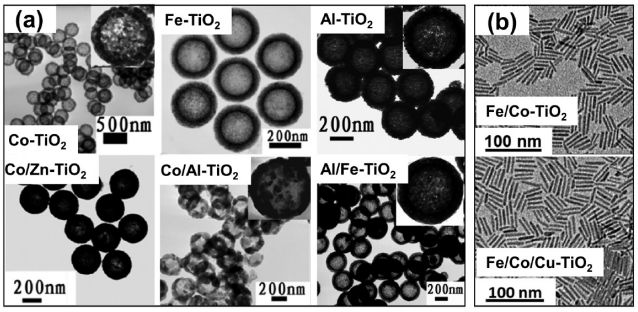

Figure 6. Morphology of metal codoped and tridoped TiO_2 NPs. (a) TEM images of hollow TiO_2 NPs doped and codoped with transition metals. Adapted with permission from ref 87. Copyright 2009 American Chemical Society. (b) Representative TEM images of transition metal codoped and tridoped TiO_2 NRs. Adapted with permission from ref 96. Copyright 2019 American Chemical Society.

utilizing varying amounts of 2-ethylimidazole.[118] However, the amount of Ti^{3+} doped successfully had no linear relation to the amount of ethylimidazole used, with the highest Ti^{3+} concentration observed by using 1 g of ethylimidazole (in a series ranging from 0.1 to 2.5 g). In a more recent study, Zhou et al. achieved Ti^{3+} doping simply by controlling the initial volume ratios of $TiCl_3$ to TTIP in the reaction solutions while utilizing a hydrothermal synthesis method.[120] Both groups noticed a strong preference for the rutile phase over the anatase phase with increasing Ti^{3+} doping. Ti^{3+} self-doping was also achieved in TiO_2 nanorods by Zhang et al.[121] A sol−gel method with TBOT was first utilized to form TiO_2 nanopowders, which were then subjected to an alkaline hydrothermal reaction in the presence of $NaBH_4$ as the reducing agent to yield Ti^{3+} self-doped TiO_2 nanorods. These nanorods, however, adopted the anatase phase, and the XRD peaks showed broadening as a consequence of the Ti^{3+} doping. The length and width of the doped nanorods were between 0.5−2 μm and 100−350 nm, respectively. However, most of these doped TiO_2 nanoparticles were neither uniform nor monodisperse. The synthesis of monodisperse uniform nanoparticles of doped TiO_2, especially solid spherical particles, remains an ongoing challenge.

4.2. Optical Properties and Applications of Doped TiO_2 Nanoparticles. *4.2.1. Nonmetal Doped TiO_2 Nanoparticles.* Doping induces various kinds of visible-light responses in TiO_2 nanoparticles. For example, Yang et al. found that a 0.5−2.0 molar doping ratio of nitrogen to titanium caused a red shift of the absorption peak and a tail from 400 nm extending all the way to 700 nm, with the 2.0 molar ratio exhibiting the longest absorption wavelengths.[112] Such an absorption was also observed by Palaez et al. upon doping with nitrogen, due to nitrogen atoms substituting oxygen atoms, which generated localized states up to 0.73 eV on top of the valence band.[116] However, the exact origin of visible-light activity in nitrogen-doped TiO_2 has been the subject of study for many researchers. Recent theoretical investigations have calculated the density of states (DOS) and partial density of states (PDOS) from the various orbital contributions in nitrogen-doped TiO_2. Studies conducted by Chen et al. attribute the substitution by nitrogen into Ti sites, which subsequently generates under-coordinated oxygen atoms as the main cause for bandgap narrowing in anatase-phase TiO_2.[77] Yang et al. also studied the effects of nitrogen-doping in rutile-phase TiO_2; these studies found that a significant decrease of the bandgap is expected in the substitutional N to Ti-atom rutile TiO_2, while the bandgap remains practically unchanged in the oxygen substitutional and interstitial N-doped structures.[78]

For spherical particles, visible-light absorption upon nitrogen doping is found to be most efficient when nitrogen is used as a codopant with other metals and nonmetals, as highlighted in a later section. There is, however, one study by Lee et al. that demonstrated enhanced visible-light absorption beyond 800 nm in N-doped nanospheres.[64] Furthermore, these authors also synthesized nanorods and found that the visible-light activity of N-doped nanorods was higher than undoped TiO_2 but lower than N-doped nanospheres. Despite the weaker light absorption, the authors also found that the N-TiO_2 nanorods produced larger amounts of O_2 via the oxidation of water due to its small overpotential in the oxygen evolution reaction (OER). Similarly, 1D N-doped TiO_2 nanotubes were evaluated by Preethi et al. for water splitting to produce H_2 gas.[113] The hydrogen-generation efficiency followed the order 1.5% > 0.5% > 3% > 4.5% > undoped TiO_2 NTs with a maximum H_2 production of 30.2 mmol/g. In these studies, a phase transformation from undoped triphasic anatase−rutile−brookite to biphasic anatase−rutile was observed as a function of increased N-doping percentage. For samples having more than 1.5% dopant, the amount of brookite phase decreased, with the H_2 production following a similar trend. The preceding observation was attributed to the absence of brookite phase, which likely leads to diminished charge separation/diffusion due to lower numbers of bulk heterojunctions and thus diminished activity. More importantly, this study established the advantages of triphasic nanoparticles, which are possible in elongated 1D nanostructures. Similar biphasic TiO_2 nanoparticles doped with iodine, consisting of anatase−brookite phase, were also studied by Zhang et al.[117] The 2.5% doped sample demonstrated maximum visible-light absorption. However, the photocatalytic reduction of CO_2 under visible light was most efficient with the 10% doped sample due to the biphasic nature and increased brookite content in the highly doped samples. Nonetheless, further increasing the amount of iodine decreased CO_2 conversion efficiency, most likely due to an increase in the number of recombination centers.

Another important nonmetal dopant is carbon. Shao et al. and Kiran et al. observed increased visible-light absorption with C-doped TiO_2 nanorods and nanowires, respectively, compared to commercial TiO_2 powders (Degussa, P-25).[109,110] Shao et al. also observed that single crystal C-doped nanorods exhibited a 2-fold increase in photocatalytic activity compared to C-doped polycrystalline TiO_2. Related studies conducted by Wu et al. also compared the light absorption and photocatalytic efficiency of nanotubes, nanowires, and nanorods.[65] The visible-light absorption of C-doped TiO_2 followed the trend: nanotubes > nanowires > nanorods. When evaluated for photodegradation of gaseous toluene, the elongated, solid nanowires outperformed the series, followed by the elongated but hollow nanotubes, while the shorter nanorods exhibited the poorest performance. These results can be attributed to the higher crystallinity of the solid NWs and lower BET surface area compared to the surface area of the NRs. The aforementioned examples show that photocatalytic efficiency is affected by a myriad of factors such as visible-light absorption efficiency, number of recombination centers, crystallinity, adopted crystal structure type, and surface area.

https://dx.doi.org/10.1021/acsanm.0c01035
ACS Appl. Nano Mater. 2020, 3, 6156−6185

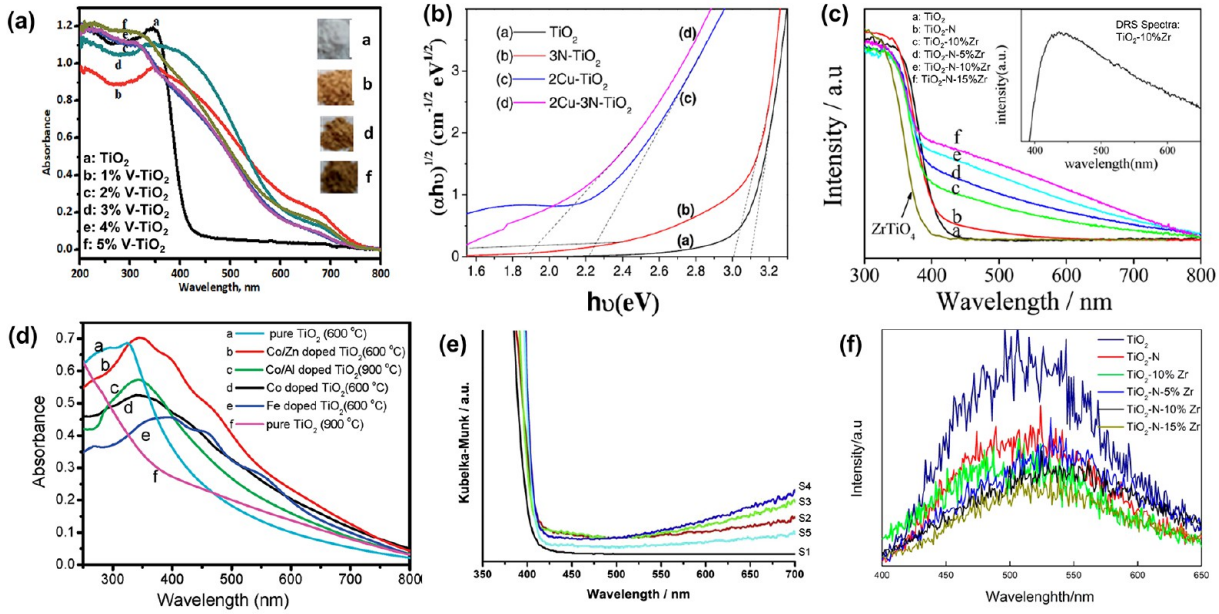

Figure 7. Optical properties of doped TiO_2 NPs. (a) UV−visible diffuse reflectance spectrum (DRS) of V-doped TiO_2 NPs. Adapted with permission from ref 122. Copyright 2018 Royal Society of Chemistry. (b) Tauc plot of TiO_2 doped with N and Cu. Adapted with permission from ref 85. Copyright 2015 Elsevier. (c, f) DRS absorption spectra and photoluminescence spectra of TiO_2 doped with N and Zr. Adapted with permission from ref 99. Copyright 2014 American Chemical Society. (d) Absorption spectra of hollow TiO_2 NPs doped with transition metals. Adapted with permission from ref 87. Copyright 2009 American Chemical Society. (e) Absorption spectra of Ti^{3+} self-doped TiO_2. Adapted with permission from ref 120. Copyright 2016 American Chemical Society.

4.2.2. Metal Doped TiO_2 Nanoparticles. Enhancing the visible-light absorption in spherical TiO_2 NPs using a single dopant has been shown to be more effective when the dopant is a metal. For example, vanadium, an early transition metal, was used by two groups to enhance visible-light absorption in anatase TiO_2. Belfaa et al. noticed a decrease in the bandgap, from 3.18 to 2.60 eV, upon increasing V doping from 0 to 8 atom %.[100] A long tail in the absorption spectra, beyond 800 nm, was observed for the V-doped TiO_2 NPs. In other related work, Takle et al. observed a much broader and gradual tail in the absorption spectra, up to 700 nm, with a much narrower bandgap around 1.79−1.69 eV for their V-doped (1−5%) TiO_2 NPs, as shown in Figure 7a.[122] Separate peaks for V_2O_4 and V_2O_5 were not observed, which suggests that the enhanced absorption is due to the presence of V^{4+} and V^{5+} states in the TiO_2 lattice. A significant reduction in the bandgap, from 3.05 eV down to 1.69 eV, was observed upon V-doping. The surface area also gradually increased with higher doping percentage, which should further enhance photocatalytic activity. These nanoparticles were then tested for photocatalytic degradation of spent wash (sugar industry) and Jakofix red dye (textile industry). However, photocatalytic studies under sunlight demonstrated the 1%-doped sample to be the most efficient, which may be attributed to its extended absorption tail in the 600−800 nm range (Figure 7a).

Another metal dopant that yields uniform visible-light-active nanoparticles is bismuth.[139] Uniform spherical Bi-doped TiO_2 NPs showed a wide absorption peak between 420 and 600 nm, accompanied by a color change from white to yellow upon doping.[139] The UV−visible spectra changed little upon varying the doping percentage, but the 0.25%-doped particles performed the best in the photocatalytic degradation of RhB dye, outperforming particles doped at 0.5 and 1%. Identical reaction kinetics were observed under two light sources (λ > 420 nm and λ > 510 nm), confirming the visible-light activity. An'amt et al. also noted that surface modification of TiO_2 nanocubes with Bi-doping led to a slight increase in size and crystallinity of the anatase phase, lowering the probability of electron−hole recombination due to rapid electron transport.[88] Increased charge transport upon Bi-doping also suppressed the recombination of electrons in TiO_2 with the dye and redox species, which in turn enhanced dye-sensitized solar-cell performance.[88] Doping TiO_2 with 1% Fe, synthesized by Eshaghi et al., led to a decrease in the bandgap from 3.33 to 3 eV.[126] This red shift was assigned to the excitation of 3d electrons of Fe^{3+} ions into the TiO_2 conduction band. When Fe-doped TiO_2 NPs were synthesized on activated carbon, the bandgap narrowed further to 2.9 eV, although the reason for this further narrowing was not discussed. Photoluminescence (PL) studies showed that photogenerated electrons from Fe-doped TiO_2 were trapped by the activated carbon, leading to greater charge separation. Fe-doped TiO_2 nanoparticles, studied by Tong et al., showed a narrower bandgap of 2.89 eV at 0.4% Fe-doping and a characteristic absorption tail extending to 550−600 nm.[128,129] A more powerful transition metal dopant for TiO_2 nanoparticles is cobalt, which has shown significant narrowing of the TiO_2 bandgap to 1.9 eV at 2% doping and 1.7 eV at 7% doping.[130,131] Co^{2+} substitution for Ti^{4+} in an octahedral or pseudo-octahedral environment leads to splitting of the *d*-orbitals of Co^{2+}, which gives rise to *d*−*d* transition peaks typically covering the entire visible region.[131] When used as an anode material for Li-ion batteries, Co-doping in TiO_2 nanoparticles enhanced the electron-transfer ability, coulombic efficiency, reversibility, retention capacity (167 mAh/g, 88.3%), and rate and cycling performance due to bandgap narrowing.[130]

Although many doped TiO_2 synthesis methods utilize calcination as one of the steps, the effects of calcination on

https://dx.doi.org/10.1021/acsanm.0c01035
ACS Appl. Nano Mater. 2020, 3, 6156−6185

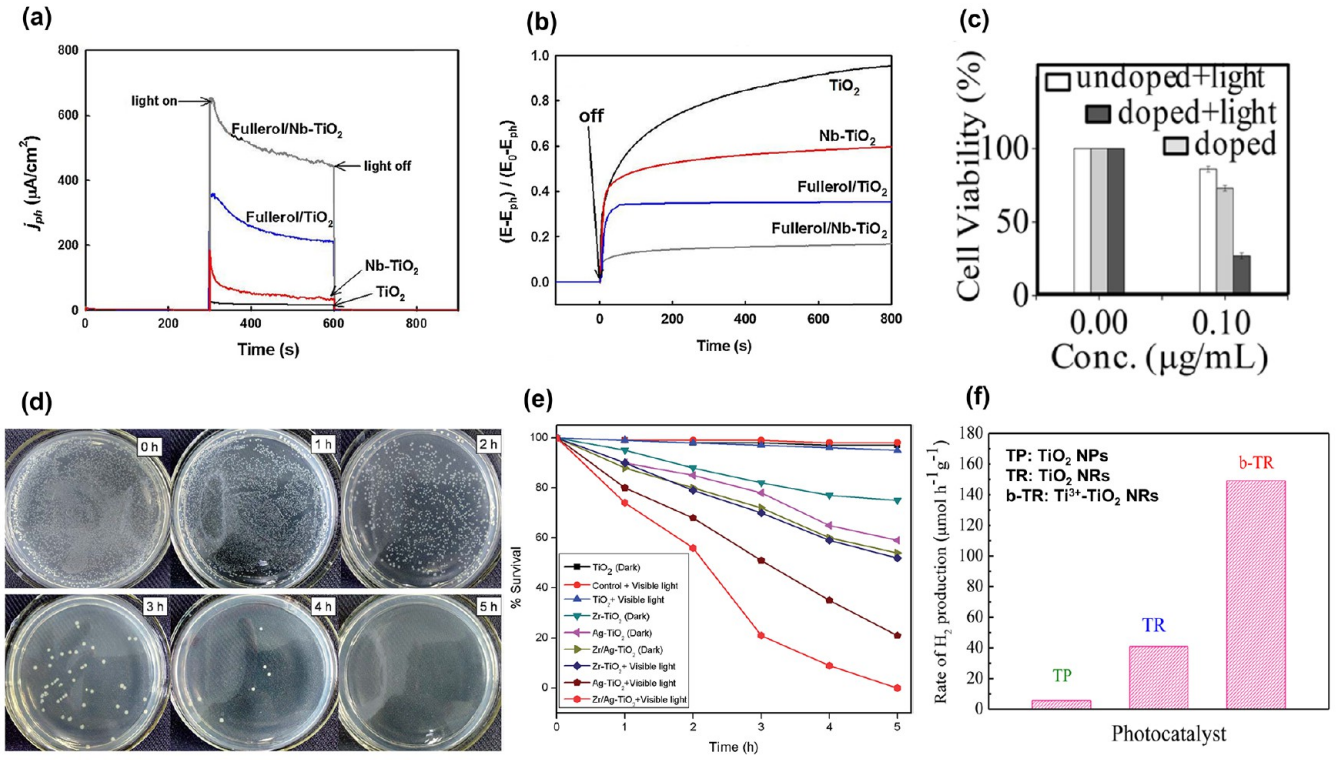

Figure 8. Applications of doped TiO_2 NPs. (a, b) Photocurrent responses of TiO_2, Nb-TiO_2, fullerol/TiO_2, and fullerol/Nb-TiO_2 electrodes under visible-light irradiation and normalized open-circuit potential (OCP) decay curves after turning off the visible light, respectively. Adapted with permission from ref 134. Copyright 2014 Elsevier. (c) Visible-light induced toxicity of N and F codoped TiO_2 nanoparticle labeled cells. Adapted with permission from ref 115. 2019 American Chemical Society. (d, e) Photocatalytic killing of *E. coli* bacteria by TiO_2 NPs doped with Zr and Ag; photographs and plot of relative rates, respectively. Adapted with permission from ref 137. Copyright 2018 Royal Society of Chemistry. (f) Photocatalytic H_2 evolution for Ti^{3+} self-doped TiO_2 nanorods under solar simulation. Adapted with permission from ref 121. Copyright 2016 American Chemical Society.

the properties are somewhat understudied. Kim et al. examined the effects of calcination temperature on PL spectra and visible-light activity of Pt-doped TiO_2 particles.[66] Higher calcination temperature gave rise to a greater suppression of electron−hole recombination. Reactions mediated by valence-band-hole oxidation are affected by the electron−hole recombination rates, and in such a reaction, higher calcination temperature showed better photocatalytic efficiency. Doping by Pt(IV) also led to a reduced bandgap from 3.0 to 2.7 eV compared to undoped TiO_2. Another parameter that influences photocatalytic activity is defect density. A few defects in a metal oxide photocatalyst, arising from the presence of dopants, can act as trapping centers to inhibit charge recombination; however, large numbers of defects can enhance charge recombination and decrease effective charge.[136] As noted by Chang et al. with Zr-doped TiO_2 nanocrystals, defect density is affected by both dopant concentration and synthesis temperature.[136] Higher dopant concentrations lead to increasing numbers of defects, while higher synthesis temperatures lead to more crystalline structures, which corresponds to fewer defects. TiO_2 nanocrystals with an optimal Zr/Ti doping ratio of 0.03 and regular shapes, synthesized at higher temperature of 400 °C (as compared to 320 °C), exhibited the highest photoactivities.[136]

Metal doping has induced visible-light absorption in colloidal 1D TiO_2 nanoparticles as well. For example, Cr-doped TiO_2 nanorods demonstrated a narrower bandgap and wider visible-light-absorption tail with increasing Cr-doping, up to 3%, leading to an enhanced photocurrent generation.[124] Doping at 1% vanadium also increased the visible-light absorption intensity and photocatalytic activity in TiO_2 nanorods.[123] Transition metal doping in TiO_2 nanorods, for example with Fe, exhibited visible-light absorption with a tail up to 600 nm monotonically increasing with higher doping percentage. When evaluated for photocatalytic H_2 production, it was observed that increasing Fe doping beyond 3.7% led to decreased activity, as dopant atoms can also act as recombination sites. Studies conducted by Liu et al., this time with Fe-doped TiO_2 nanorod clusters, displayed certain advantages due to the cluster morphology.[127] The Fe-doped TiO_2 nanorod clusters exhibited a more significant red shift in the band edge and an absorption tail up to 600 nm compared to undoped P25, N-doped TiO_2 NPs, and also monodisperse Fe-doped NRs. The nanorod clusters also demonstrated higher photocatalytic activity than monodisperse NRs and overall a 7-fold enhancement compared to P25, demonstrating the advantages of the nanorod cluster morphology. We noted above that doped metal oxide nanoparticles possess photodegradation capabilities under visible light, which is also true for 1D nanostructures. Miyauchi et al. synthesized Cu-doped TiO_2 nanotubes and then spin-coated them to make thin films.[132] These films become superhydrophilic and photodegrading under visible light, making them promising materials for self-cleaning windows.[132] The Cu^{2+}-grafted TiO_2 absorbs visible light by interfacial charge transfer between valence band of rutile TiO_2 and surface-modified Cu^{2+} ions.[132] Interfacial

https://dx.doi.org/10.1021/acsanm.0c01035
ACS Appl. Nano Mater. 2020, 3, 6156−6185

charge transfer (IFCT) in bimetallic assemblies have also been reported in other studies of visible-light-driven decomposition of organic contaminants.[169−171] Irie et al. also observed charge-transfer processes in photosensitized Cu(II)-grafted TiO_2 and WO_3.[169] Charge-transfer processes in Cu(II)-grafted TiO_2 typically create a hole in the valence band of rutile TiO_2, which decomposes organic substrates, while the Cu(I) produced by electron transfer reduces absorbed O_2.[171] Nakamura et al. discovered the generation of photocurrent in Ce(III)-grafted TiO_2 electrodes in O_2-saturated acetonitrile solutions, leading to photoirradiation-induced charge transfer from atomic Ce(III) ions to the conduction band of TiO_2 when atomically grafted onto TiO_2 surfaces.[170]

The effects of doping metal oxides can be further exploited to enable visible-light absorption via complexation or plasmonic activation as well.[134,135] For example, another transition metal niobium was used by Lim et al. to dope TiO_2 with fullerol complexation.[134] The Nb doping increased charge transfer and interfacial electron transfer and formed Ti cation vacancies that act as electron-trap sites and retarded the recombination of charge pairs. An increase in niobium doping also caused a red shift of the absorption band edge, but the absorption of fullerol on the Nb-TiO_2 surface showed a much more significant increase in visible-light absorption via a mechanism called surface-complex charge transfer (SCCT). Photocurrent studies demonstrated a significant increase in the creation of charge carriers. The open-circuit potential (OCP) decay after turning off the light also showed a slower rate of charge-carrier recombination upon Nb doping and upon incorporation of fullerol (Figures 8a and 8b, respectively). Nb-doping facilitated interfacial electron transfer, enhancing the overall photocatalytic activity. Additional absorption in the visible region can also be triggered by rare earth dopants in TiO_2. Rare earth metals are known for their sharp spectral features caused by upconversion and are widely used for phosphors.[172] Similarly, Er^{3+}-doped TiO_2 nanoparticles show sharp absorption peaks at 451, 489, 522, 654, and 796 nm, corresponding to transitions from the Er-ion ground state $^4I_{15/2}$ to higher energy levels, $^4F_{5/2}$, $^4F_{7/2}$, $^2H_{11/2}$, $^4F_{9/2}$, and $^4G_{9/2}$, respectively.[141] Such sharp spectral features offer the option for selective activation using wavelength-specific light-emitting diodes (LEDs). Additionally, Er-doping in TiO_2 also generates defects and accelerates charge transfer between TiO_2 and Er^{3+} ions, promoting the photocatalytic degradation of volatile organic compounds (VOCs).

Another mechanism used by researchers to activate visible-light absorption in metal oxides is localized surface plasmon resonance (LSPR).[135] Importantly, via the LSPR, noble metal nanoparticles are enabled to strongly absorb visible light. This phenomenon can also be triggered and carefully tuned in metal oxides by controlling the free electron concentration via doping. LSPR properties activated by heavy extrinsic doping with metals have been most widely studied in doped indium oxides and zinc oxides. However, the LSPR absorption in these materials occur only for infrared wavelengths. Cao et al. discovered that upon doping TiO_2 with molybdenum and tungsten, LSPR-induced absorption in the visible region was successfully achieved.[135] These researchers found that Mo-doped TiO_2 nanocrystals had a sharp absorption peak centered around 650 nm, while the W-doped TiO_2 nanocrystals had a wide peak extending from 500 to 2000 nm. Increases in dopant concentration generally lead to increases in absorption intensity until 15.3%, after which a trend reversal occurs due to scattering. Similar to ITO, doping TiO_2 leads to an increase in the number of electrons near the Fermi level, which is shifted to slightly above the conduction band minimum (CBM). However, the electrons near the CBM are not derived from the dopants themselves, but from the dopant-perturbed Ti electronic structure. The free electron concentration in Mo-doped TiO_2 nanocrystals was comparable to that of noble metals, and the peak shape closely resembled that for Au NPs. On the other hand, the LSPR peak of W-doped TiO_2 was much wider, covering a larger portion of the visible to near-IR regions. The authors also noticed that on varying the size of the W-doped nanocrystals from 13 to 5 nm gave rise to a blue-shift in the peak maximum (λ_{max}) from 1700 to 980 nm, further shifting the majority of the absorption to the visible to near-IR regions.

4.2.3. Codoped and Tridoped TiO_2 Nanoparticles. One of the more effective strategies used to enhance the light absorption of TiO_2 NPs is to codope with two or more elements. Often the effects of codoping significantly outperform the effects of the dopants when used separately. For example, fluorine doping causes no changes in the absorption edge for TiO_2 by itself, but when codoped with nitrogen, it contributes to the creation of surface oxygen vacancies based on photoluminescence (PL) analysis, which enhances visible-light absorption. For these types of particles, the bandgap decreased from 3.00 eV for TiO_2 and 2.99 eV for F-TiO_2 to 2.80 eV for N-TiO_2 and 2.75 eV for N,F-TiO_2. Nitrogen and fluorine were also codoped into TiO_2 nanorods by Biswas et al.[115] These N,F-TiO_2 nanorods (NRs) displayed an intense absorption in the visible region, covering the span of 350−900 nm. Biswas et al. investigated the visible-light induced generation of reactive oxygen species (ROS), which are responsible for its photocatalytic activity and for triggering light-induced cytotoxicity. Their results show that HeLa cells labeled with doped TiO_2 NRs and exposed to visible light show green emission due to the formation of ROS. In contrast, undoped TiO_2 NRs fail to produce ROS under visible light, and doped TiO_2 NRs fail to produce ROS if unexposed to visible light (see Figure 8c). Albrbar and coworkers noticed that codoping nitrogen with sulfur decreased the optical bandgap from 2.74 to 2.32 eV.[74] These particles were tested for RO16 dye degradation and provided high visible-light activity due to increased surface area, mesoporosity, and absorption. Theoretical studies by Yang et al. indicate that sulfur substitution at the oxygen sites introduce additional S-3p orbitals, increasing the width of the valence band, thus narrowing the bandgap.[78] Higher doping percentages of sulfur lead to orbital mixing and thus a significant narrowing of the bandgap. C,N,S-tridoped TiO_2 prepared by Lin et al., using a thiourea precursor, exhibited absorption spectra similar to other N-doped TiO_2 nanoparticles with steady enhancement of visible absorption as the ratio of thiurea:TiO_2 was increased, leading to a steady decline in the recombination rate of the photogenerated electrons and holes of TiO_2.[76] Doping improved the rate of photocatalytic degradation of X-3B (Reactive Brilliant Red dye).

Jaiswal et al. found that monodoping anatase TiO_2 with nitrogen (3 atom %) decreased the bandgap to 3 eV, while monodoping with copper (2 atom %) decreased it to ∼2.2 eV, as shown in Figure 7b.[85] Codoping with both nitrogen (3 atom %) and copper (2 atom %) afforded even narrower bandgap values, under 2.0 eV, compared to monodoped nanoparticles. From their studies, it can be concluded that nitrogen doping in

https://dx.doi.org/10.1021/acsanm.0c01035
ACS Appl. Nano Mater. 2020, 3, 6156−6185

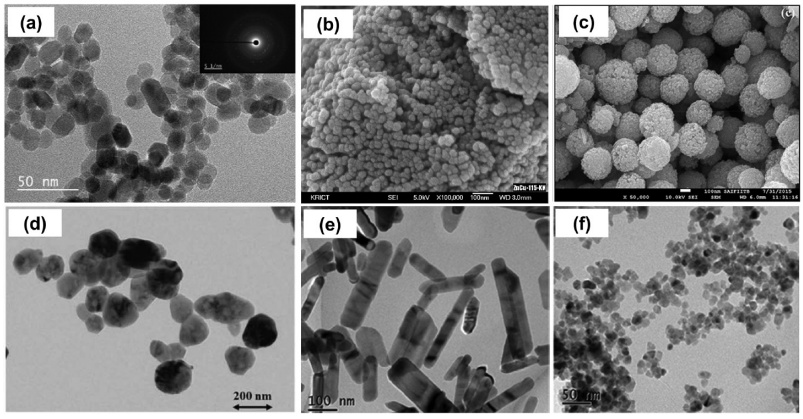

Figure 9. Morphology of doped ZnO NPs. (a) TEM image of Mn-doped ZnO NPs (inset includes SAED pattern). Adapted with permission from ref 73. (b) FESEM image of Cu-doped ZnO NPs. Adapted with permission from ref 151. Copyright 2007 Elsevier. Copyright 2016 Elsevier. (c) SEM image of Cu-doped nanoporous ZnO NPs. Adapted with permission from ref 150. Copyright 2017 American Chemical Society. (d) TEM image of Co-doped ZnO NPs. Adapted with permission from ref 148. Copyright 2017 Royal Society of Chemistry. (e, f) TEM images of 19 and 59% C-doped TiO_2 NPs, respectively, demonstrating conversion of morphology from nanorods to nanospheres with increasing carbon content. Adapted with permission from ref 142. Copyright 2015 American Chemical Society.

TiO_2 NPs effectively induces a broad absorption tail until 700 nm or more, which is further enhanced when codoped with another element.

Zhang et al. attempted to codope nitrogen and zirconium in anatase TiO_2.[99] $ZrTiO_4$ has a larger bandgap than TiO_2, but upon codoping with both N and Zr, visible-light absorption is significantly enhanced up to 800 nm, although the absorption edge itself shifts little, as shown in Figure 7c. The zirconium is substitutionally doped into the TiO_2 lattice, but the nitrogen primarily existed as surface NO_x species. The synergistic effects of these two species (doped Zr and surface NO_x) leads to a wide absorption in the visible region and an increase in the total number of charge carriers (Figure 7f). In contrast, a narrowing of the bandgap upon zirconium substitution in anatase TiO_2 NPs was observed by Naraginti et al. down to 2.98 eV.[137] These two studies suggest that zirconium by itself is a weak dopant for tuning the absorption edge and narrow the anatase TiO_2 bandgap. However, codoping with Zr and Ag showed an even narrower bandgap of 2.82 eV and a greater suppression of electron−hole recombination than the mono-doped samples. Thus, both studies show that zirconium, although a relatively weak dopant by itself, can be an effective codopant. These Zr- and Ag-doped TiO_2 NPs were used for the photocatalytic destruction of *E. coli* bacteria; the codoped sample demonstrated 100% effectiveness in killing the bacteria within 5 h, as shown in Figure 8d. There is a gradual and consistent improvement in photocatalytic activity upon monodoping with Zr and Ag individually and codoping with Zr/Ag, with the enhancement much more pronounced under visible-light irradiation, as shown in Figure 8e. The Ag monodoped TiO_2 NPs showed a bandgap of 3.17 eV. Utilizing a similar synthetic strategy, much more significant narrowing of the bandgap, down to about 2.5 eV, was observed by Ali et al. using 8 mol % Ag doping.[138] In their case, a broad visible absorption, similar to that induced by nitrogen doping, was observed in the 400−800 nm range.

Zn and Mn codoped anatase TiO_2 introduced by Benjwala et al. showed that $Ti_{1-x}Zn_xMn_xO_{2-x}$ exhibited a reduction in the bandgap from 3.1 to 2.9 eV when $x = 1$ (1% doping) and further reduction to 2.86 eV when $x = 2$ (2% doping).[83] There was also a slight decrease in PL intensity, most likely due to the transfer of electrons from excited TiO_2 to new energy levels created by the codopant. Interestingly, 1% Mn and Zn doped TiO_2 showed a better suppression of charge recombination than the 2% doped sample, implying that although higher doping lowers the bandgap, it aids recombination of electron−hole pairs. Peng et al. studied hollow TiO_2 doped with multiple transition metal ions.[87] Fe-doped TiO_2 showed a strong broad absorption up to 600 nm, displaying a red color, similar to the Co-doped spheres, which displayed a green color in solution (Figure 7d). However, the most impressive visible-light absorption was observed for Co and Zn codoped spheres, which displayed a dark green color in solution (Figure 7d). Similar spectral features were also observed for the 25% Zr-doped TiO_2, exhibiting a wide tail up to 600 nm and a bandgap of 2.8 eV.[93]

4.2.4. Ti^{3+} Self Doped TiO_2 Nanoparticles. Titanium in TiO_2 exists mainly in the Ti^{4+} state. TiO_2 can be self-doped with Ti^{3+} ions, which gives rise to a wide absorption band that is different from the UV−vis spectra of extrinsically doped TiO_2. TiO_2 particles self-doped with Ti^{3+} synthesized by Zuo et al. and also by Zhou et al. both showed a wide absorption band that increases with increasing wavelength to 800 nm and beyond, as illustrated in Figure 7e.[118,120] It is interesting to note that this spectral phenomenon has not been observed for any other dopant. Upon increasing the concentration of Ti^{3+}, the absorption in the visible region was highly enhanced, with the products exhibiting a strong blue color, and the absorption band shifted to longer wavelengths. When Zhang et al. self-doped Ti^{3+} into TiO_2 nanorods, the same type of absorption feature as well as a blue colored powder were observed.[121] The enhanced absorption at wavelengths longer than 400 nm could be ascribed to a high number of oxygen vacancies. The absorption edge bandgap was also reduced on Ti^{3+} doping, from 3.16 to 2.56 eV. Theoretical calculations suggest that upon Ti^{3+} doping, a miniband forms just below the conduction band minimum of undoped TiO_2. The bandgap of TiO_2 nanorods was reduced to 2.61 eV from 3.20 eV upon Ti^{3+} doping. These doped nanorods demonstrated remarkable photoelectrochemical (PEC) performance and hydrogen production efficiency (30-fold increase) compared to undoped TiO_2 NPs, as shown in Figure 8f.

https://dx.doi.org/10.1021/acsanm.0c01035
ACS Appl. Nano Mater. 2020, 3, 6156−6185

5. DOPED ZINC OXIDE (ZNO) NANOPARTICLES

5.1. Synthesis and Structure of Doped ZnO Nanoparticles. *5.1.1. Transition Metal Doped ZnO Nanoparticles.* Visible-light-active doped zinc oxide nanoparticles mostly feature cation doping. The most common zinc precursors used in the synthesis of doped zinc oxide nanoparticles are the acetate, nitrate, and chloride salts of zinc.[72,73,147,148,153] For transition metal doping, zinc acetate is commonly used, generally cohydrolyzed using sodium hydroxide in the presence of the acetate salt of the dopant metal. Co-hydrolysis of zinc acetate with manganese acetate followed by hydrothermal treatment at 160 °C for 24 h led to the successful synthesis of Mn-doped zinc oxide by Achouri and coworkers.[73] The 1−7% doping was achieved using the aforementioned method, keeping the hexagonal ZnO wurtzite structure intact. The size of the Mn-doped ZnO nanoparticles was found to be somewhat smaller than the undoped congeners, which can be attributed mainly to the inhibition of growth from the presence of dopant ions in the reaction medium (Figure 9a). Ullah et al. also used the cohydrolysis of zinc acetate with manganese acetate to synthesize Mn-doped zinc oxide nanoparticles.[146] Alcoholic solutions are used for this method by both groups to avoid the formation of ZnOH.[73,146] Hydrolysis of zinc acetate in the presence of cobalt chloride led to the successful synthesis of Co-doped zinc oxide with a doping percentage up to 4% by Jacob et al.[148] The synthesized nanoparticles had a diameter of 40−50 nm with consistent hexagonal wurtzite structure (Figure 9d). In place of cobalt chloride, Kanade et al. used copper chloride to synthesize uniformly spherical Cu-doped zinc oxide nanoparticles, as shown in Figure 9b.[151] The authors used an oxalic acid and ethylene glycol system instead of NaOH to achieve the hydrolysis to zinc oxide. Cu-doping up to 1.5% was obtained using the aforementioned method to yield particle sizes around 40−55 nm, similar to the Co-doped zinc oxide particles of Jacob et al.[148,151]

Another method for synthesizing uniform spherical Cu-doped ZnO nanocrystals was reported by Lu et al.[152] These authors employed an ultrafast, ionic liquid-based antisolvent method involving ZnO powders in a deep eutectic solvent (DES), followed by precipitation and growth of ZnO upon injection into a "bad" solvent (low solubility for ZnO). When ZnO-containing DES was injected into a bad solvent containing Cu^{2+} ions, Cu-doped ZnO was quickly precipitated from the solution owing to the dramatic decrease in solubility; this method afforded nanoparticles with well-defined morphology and controllable Cu^{2+} concentrations. Gupta et al. obtained uniform, discrete, spherical, porous Cu-doped nanoparticles ∼150 nm in diameter by using copper acetate with zinc acetate instead of copper chloride (Figure 9c).[150] The porous structures were found to consist of multiple smaller nanoparticles, around ∼15 nm in size, and the crystallite sizes were also observed to be in a similar range (17 nm for pristine ZnO decreasing to 9.8 nm for 10% Cu-doped zinc oxide). Fe-doped zinc oxide nanoflower particles with a doping percentage between 0.5−5% were synthesized using cohydrolysis of zinc acetate with ferric nitrate by Han et al. followed by hydrothermal treatment at 150 °C and sintering at 600 °C.[147] When the Fe content was less than 1%, the zinc oxide XRD peaks were somewhat shifted to higher angles; however, upon further increasing zinc doping, additional peaks attributed to $ZnFe_2O_4$ started to appear. Nitrate salts of the dopants used with a zinc nitrate precursor also afforded doped zinc oxide nanoparticles.[147] The use of silver nitrate with a zinc nitrate precursor by Nigussie et al. led to the formation of silver-doped zinc oxide nanoparticles.[153]

5.1.2. Non-Transition Metal Doped ZnO Nanoparticles. As observed for Fe-doped ZnO nanoparticles (vide supra), the use of the nitrate salts of the dopant with zinc acetate can also be employed for non-transition metal doping. For example, zinc acetate was used by Khan et al. with aluminum nitrate in a sol−gel process to achieve 0.5−2% Al-doped zinc oxide nanoparticles, obtained with a hexagonal ZnO structure.[145] The crystallite size was initially found to increase and then decrease upon increasing Al doping. Zinc nitrate, the other common precursor for zin oxide, can also be used for non-transition metal doping. Faraz et al. used a gel-combustion technique with zinc nitrate with samarium chloride to synthesize 1, 3, and 5% Sm-doped zinc oxide nanoparticles. The authors began by first making a gel of the precursors in a magnetic stirrer followed by an increase of the reaction temperature to 600 °C.[84]

However, doping a non-transition metal in zinc oxide nanoparticles is generally achieved via the coprecipitation method by mixing the zinc chloride precursor with a similar salt of the dopant metal. A facile coprecipitation method was utilized by Pradeev Raj and coworkers for the preparation of Mg-doped zinc oxide nanoparticles.[72] The chloride salts of magnesium and zinc were mixed in equimolar ratios and stirred with sodium hydroxide solution; sodium hydroxide aids in the precipitation of transition metal hydroxides, in this case zinc hydroxide, which after heating yields zinc oxide nanoparticles. Addition of the magnesium salt enables successful doping of Mg from 2.5−7.5% following this method. Etacheri et al. also started with zinc chloride for the synthesis of Mg doped zinc oxide nanoparticles.[144] Zinc chloride was mixed with nitric acid and magnesium nitrate to use a coprecipitation method in oxalic acid. The Mg doping percentage was controlled by stoichiometric addition of magnesium nitrate during the synthesis. The Mg-doped zinc oxide nanoparticles had diameters on the order of 50 nm. In both of these studies of Mg-doped zinc oxide nanoparticles, the hexagonal wurtzite zinc oxide phase was observed after Mg doping and calcination above 300 and 400 °C, respectively. Mg doping was also found to decrease strain and increase the crystallite size. Zinc chloride was also used for 3% Dy-doped zinc oxide synthesis by using $DyN_3O_9{\cdot}6H_2O$ with NaOH in ethanol followed by calcination at 300 °C.[154] Thus, overall, various permutations of the acetate, nitrate, and chloride salts of zinc and its dopants can be utilized to obtain metal-doped zinc oxide nanoparticles.

5.1.3. Nonmetal Doped ZnO Nanoparticles. Although nitrogen is the most common dopant for TiO_2 nanoparticles, the synthesis of uniform nitrogen-doped ZnO nanoparticles has proven to be challenging. Most N-doped ZnO studies involve films rather than colloidal nanoparticles.[173,174] There are only a handful of reports that demonstrate the ability to form nonaggregated N-doped ZnO NPs.[75,142,143,175,176] Macías-Sánchez et al. synthesized nitrogen-doped zinc oxide nanoparticles from zinc acetate and urea as precursors while using ammonium hydroxide as the nitrogen source.[75] Further calcination of the particles at 400 °C for 5 h in air afforded mixed agglomerates of N-doped zinc oxide rods and spheres with an average size around 80−100 nm. The crystallite size decreased upon nitrogen doping suggesting increased lattice strain. Similar results were observed by Zhang et al. using an analogous recipe that involved carbon instead of nitrogen

https://dx.doi.org/10.1021/acsanm.0c01035
ACS Appl. Nano Mater. 2020, 3, 6156−6185

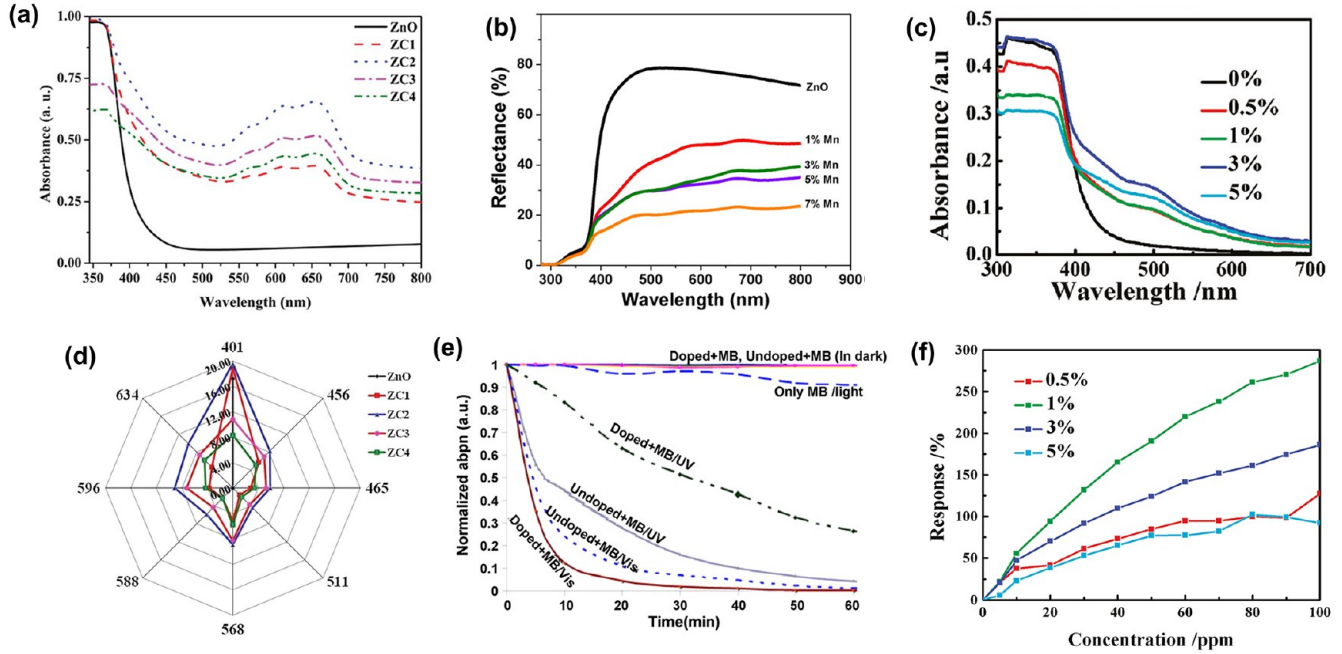

Figure 10. Optical properties and applications of doped ZnO NPs. (a, d) Absorption spectra and relative photocatalytic activity at different wavelength irradiation, respectively, for Co-doped ZnO NPs. Adapted with permission from ref 148. Copyright 2017 Royal Society of Chemistry. (b) DRS spectra of Mn-doped ZnO NPs. Adapted with permission from ref 73. Copyright 2016 Elsevier. (c, f) Absorption spectra and gas sensing response vs concentration for Fe-doped ZnO nanoflowers. Adapted with permission from ref 147. Copyright 2011 American Chemical Society. (e) Comparative UV−visible spectra of methylene blue dye degraded with time by Mn-doped ZnO NPs under UV and visible light. Adapted with permission from ref 146. Copyright 2008 Elsevier.

doping.[142] Carbon-doped zinc oxide nanoparticles were synthesized by grinding zinc acetate with urea in a mortar and then annealing at 450 °C. The undoped zinc oxide particles exhibited nanorod morphology, but upon carbon doping, the aspect ratio gradually decreased to yield spheres for the 30, 40, and 50 wt % carbon-doped samples (see Figures 9e-f). The crystallite size (∼50 nm) remained relatively constant up to 20% carbon doping; however, a gradual drop from 33 nm for the 30% doped sample to 12 nm for the 40% doped sample was observed. This recipe, which yielded largely discrete nanoparticles using gram-scale quantities of the reagents, holds promise for large-scale industrial synthesis.

5.2. Properties and Applications of Doped ZnO Nanoparticles. *5.2.1. Transition Metal Doped ZnO Nanoparticles.* Undoped zinc oxide has a direct bandgap at 3.37 eV and like TiO_2, doping can extend the activity of zinc oxide to the visible region. Among doped zinc oxide nanoparticles, the most promising visible-light absorption was observed by the Co-doped zinc oxide nanoparticles synthesized by Jacob et al.[148] Co doping introduced new peaks in the 563, 610, and 657 nm regions corresponding to d-d transitions of Co^{2+} ions in tetrahedral coordination, as shown in Figure 10a. The strongest visible-light absorption due to these peaks was observed for the 2% doped sample. While the absorption in the UV region remained the same as undoped ZnO, an overall drop in the absorption across all wavelengths started with higher doping concentrations of Co (Figure 10a). The bandgap also initially narrowed upon Co doping at 1% and 2% but widened for the sample with high Co doping percentages (3% and 4%). The photocurrent and quantum efficiency studies also followed the same trend, increasing then decreasing again with increasing doping percentage (Figure 10d). The best photocurrent performance was observed for the 2% Co-doped zinc oxide sample under the various visible-light lasers used. Similar spectral features were observed by Bilecka et al. for Co-doped ZnO nanoparticles.[149] However, their nanoparticles were much smaller (∼10 nm) than those synthesized by Jacob et al. (40−50 nm)[148] and showed a gradual increase in absorption with Co doping percentage up to 30%; these nanoparticles also showed Curie−Weiss magnetic behavior. Along with magnetic behavior, the Fe-, Ni-, and Mn-doped ZnO nanoparticles all showed strong visible-light absorption, although detailed UV−vis spectra for these compounds were not reported. Such diluted magnetic semiconductors can be applied in spintronics to enable enhanced electrical and photonic devices.

Strong visible-light absorption was also observed upon Mn-doping by Achouri et al. (Figure 10b).[73] Their 7% Mn-doped porous zinc oxide nanoparticles showed nearly four times higher visible-light absorption compared to undoped ZnO; the bandgap also gradually decreased from 3.06 to 2.84 eV. However, photocatalytic activity under solar light was best exhibited by the 3% doped sample and decreased with higher doping percentages. The Mn^{2+} ions initially act as electron-trap centers, decreasing recombination and enhancing interfacial charge transfer; however, Mn^{2+} ions will act as recombination centers when in excess, which could be a possible reason for the observed trend. In studies by Ullah et al., zinc oxide nanoparticles doped with Mn^{2+} also showed much higher overall absorption than undoped zinc oxide, extending well into the visible region up to 650 nm.[146] Their studies suggested that Mn-doped ZnO exhibits higher visible-light absorption than Al- and Cu-doped ZnO, which can be attributed to the greater number of defect sites in Mn-doped ZnO. When used for the photocatalytic degradation of dyes, the doped nanoparticles underperformed compared to

https://dx.doi.org/10.1021/acsanm.0c01035
ACS Appl. Nano Mater. 2020, 3, 6156−6185

undoped ZnO nanoparticles in the UV region but exhibited a 50-fold increase in performance under visible light (see Figure 10e).

Fe-doping in flower-like ZnO NPs synthesized Han et al. also showed enhanced visible-light absorption and photocurrent generation.[147] Fe-doping introduced an absorption tail in the visible region up to 700 nm, which increased with Fe doping until a 3% doping was achieved but dropped for the 5% Fe-doped sample, as shown in Figure 10c. The photocurrent studies concluded negligible performance for the pure ZnO sample while the 1% Fe-doped sample performed the best, compared to the undoped, 3%, and 5% Fe-doped samples. In fact, the 5% Fe-doped sample performed the worst compared to all other doped samples, and the 3% Fe-doped sample performed similar to the 0.5% Fe-doped sample. The high Fe doping in the samples created a secondary $ZnFe_2O_4$ phase on the surface, which led to increased grain and grain boundary resistances and potential barriers.[147] Figure 10f shows that the 1% Fe-doped sample also demonstrated the best gas sensing performance with formaldehyde gas. The 1% Fe-doped sample was also exceptionally stable for multiple cycles.

Cu-doped zinc oxide nanoparticles also displayed similar spectral features in the visible region as the Fe-doped nanoflowers, gradually increasing with copper doping.[151] Doping with Cu increased H_2 production from the decomposition of H_2S by about 2.5-fold compared to undoped ZnO NPs. However, compared to this study, Gupta et al. observed much higher and wider visible-light absorption for porous Cu-doped ZnO NPs.[150] These particles were evaluated for photocatalytic, antibacterial, as well as tumor suppression applications. The Cu existed in multiple valence states, which enhanced charge separation as the PL intensity decreased with increasing Cu doping until 5% doping, but increased for the 10% Cu-doped sample. The 5% Cu-doped sample also outperformed all samples in the photocatalytic and antibacterial studies performed. These Cu-doped zinc oxide nanoparticles also successfully obstructed cervical cancer and hepato-carcinoma cells with vigorous cell proliferation, thereby exhibiting antibacterial and anticancer activity under dark as well as visible-light irradiation. The best visible-light absorption was, however, observed for the Cu-doped ZnO nanocrystals synthesized by Lu et al. showing much stronger and wider visible-light absorption.[152] The absorption was attributed to intraband transitions induced by the doped Cu^{2+}. This allowed excitation of ZnO by light with energy lower than the bandgap, generating extra charge carriers. The color of Cu-doped ZnO turned milky green with increasing Cu^{2+} concentration. Although visible-light absorption consistently increased with increasing Cu^{2+} concentration, overall photoconversion efficiency was severely hampered by carrier trapping at higher doping concentrations. Photoelectrochemical (PEC) measurements demonstrated about a 2-fold increase in performance for the 2% Cu-doped sample over the undoped sample, while the 5% Cu-doped sample performed worse than the undoped sample, and the 10% Cu-doped sample showed almost no photocurrent density at all. In addition to visible-light absorption, these Cu-doped ZnO nanocrystals exhibited room temperature ferromagnetism, where the saturation magnetization increased with increasing Cu^{2+} concentration. This feature makes these Cu-doped ZnO nanocrystals promising materials for magneto-optical applications.

Antibacterial studies were also performed using Ag-doped zinc oxide nanoparticles.[153] Ag-doped zinc oxide exhibits a slightly red-shifted band edge (>400 nm) likely due to the silver plasmonic peak around 420 nm. ZnO nanoparticles exhibited better antibacterial performance than TiO_2 nanoparticles, and this trend also held true for Ag-doped ZnO and TiO_2 nanoparticles, both of which performed better than the respective undoped metal oxide nanoparticles.

5.2.2. Non-Transition Metal Doped ZnO Nanoparticles. The trend of visible-light activity increasing with doping and then decreasing again after an optimum point has also been observed for Dy-doped zinc oxide nanoparticles. In the decoloration of AR17, 3% Dy-doped zinc oxide nanoparticles showed three times the photocatalytic activity compared to that of undoped zinc oxide under visible light.[154] Dy^{4+} species can receive photogenerated electrons from the CB of ZnO to form Dy^{3+}, effectively slowing recombination and increasing interfacial charge-transfer efficiency. Samarium also proved to be an uncommon but effective dopant for increasing visible-light absorption in zinc oxide nanoparticles.[84] The bandgap decreased from 3.27 to 3.05 eV upon samarium doping. Although visible-light absorption changed gradually upon increasing Sm doping, the best photocatalytic activity was exhibited by the 3% Sm-doped sample, better than the 5% Sm-doped sample. These results indicate that higher doping percentages often create new electron−hole recombination sites, decreasing photocatalytic performance in spite of enhanced absorption.

Mg-doped zinc oxide nanoparticles, however, exhibit a much more monotonic enhancement of the optical and photocatalytic activities with increasing doping percentage.[72] The bandgap decreased gradually from 3.36 to 3.04 upon 7% Mg-doping, and a concurrent reduction in electron hole recombination was also observed. Photocatalytic performance in the degradation of RhB dyes also increased consistently upon Mg doping and was observed to be about 8 times higher for the 7.5% Mg-doped sample compared to undoped zinc oxide nanoparticles. Additionally, these Mg-doped zinc oxide nanoparticles also demonstrated antibacterial abilities.[72] Doping in films and microstructured photocatalysts has shown to induce changes in the photocatalytic mechanism due to changes in surface topography.[37−41] However, at the size range of nanoscale particles, changes in surface topography are rarely evident. In one study, Lu et al. observed that Mg-doped ZnO nanoparticles have a smoother surface and narrower size distribution than undoped ZnO nanoparticles, which is an interesting observation because doping generally increases surface disorder.[177] However, the direct effect of the surface characteristics on photocatalytic mechanism is not well understood. In the Lu et al. studies, the doped nanoparticles exhibited slightly higher photocatalytic activity, which can be attributed in part to their slightly red-shifted light-absorption.[177]

Generally speaking, the most commonly used doped zinc oxide material is aluminum-doped zinc oxide. However, in spite of being abundantly used as a transparent conducting oxide, especially as thin films, these materials have often failed to exhibit visible-light activity. Visible-light-active aluminum-doped zinc oxide nanoparticles are almost unheard of. One rare study by Khan et al. demonstrated the formation of visible-light-active Al-doped zinc oxide nanoparticles.[145] Aluminum doping appeared to increase absorption in the visible region with an absorption peak around 400 nm and a tail extending up to 800 nm. However, the bandgap increased upon doping with aluminum.

https://dx.doi.org/10.1021/acsanm.0c01035
ACS Appl. Nano Mater. 2020, 3, 6156−6185

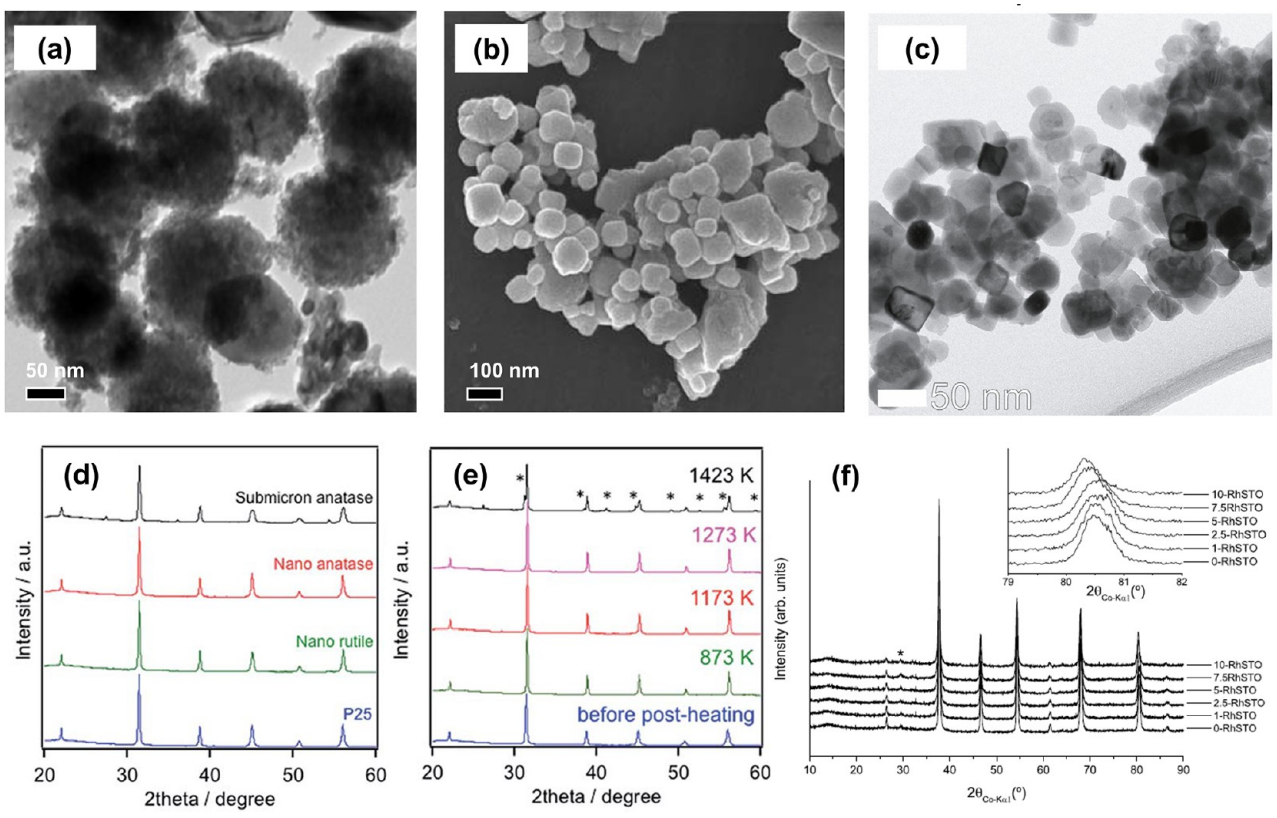

Figure 11. Morphology and structure of doped $BaTiO_3$ and $SrTiO_3$ NPs. (a) TEM image of Ce-doped $BaTiO_3$ NPs. Adapted with permission from ref 158. Copyright 2019 American Chemical Society. (b, d, e) SEM image and XRD patterns for Rh-doped $BaTiO_3$ NPs made from various TiO_2 NP precursors after heat treatment. Adapted with permission from ref 159. Copyright 2015 Royal Society of Chemistry. (c, f) TEM image and XRD patterns for Rh-doped $SrTiO_3$ NPs. Adapted with permission from ref 157. Copyright 2017 Elsevier.

5.2.3. Nonmetal Doped ZnO Nanoparticles. Doping with nonmetals have also been employed to activate visible-light absorption in ZnO NPs. Carbon and nitrogen are the primary nonmetal dopants used in doped ZnO NPs. A significant reduction in the bandgap energy was observed upon carbon doping by Zhang et al.[142] The highest overall visible-light absorption was observed for the 30% C-doped sample exhibiting nearly thrice the absorption compared to the undoped zinc oxide nanoparticles. Increasing the amount of carbon lead to a change in the morphology from nanorods to nanospheres. The bandgap also monotonically decreased upon increasing carbon doping up to 40% from 3.19 to 2.72 eV. Generally, a nanorod morphology offers a longer lifetime for photogenerated charge carriers. However, in their studies, Zhang et al. found the photoluminescence (PL) intensity also decreased gradually upon carbon doping, meaning that the nanospheres had a lower rate of recombination than the nanorods. As a result of these two factors, the nanospheres with a higher C-doping percentage (59%) demonstrated better photocatalytic activity than the 10% C-doped nanorods. Similar to the observations with TiO_2 NRs by Zhang et al.[121] and Lee at al.,[64] these trends suggest that doping percentage is a more significant factor than morphology for photocatalytic enhancement. Nitrogen is another dopant which was effective in reducing the bandgap of zinc oxide from 3.06 to 2.87 eV and was found useful for herbicide degradation (2,4-D and picloram).[75] Another study by Kale et al. showed that nitrogen doping in porous ZnO nanocomposites could reduce the bandgap of ZnO from 3.14 to 2.97 while also adding an absorption tail up to 700 nm.[143] The nitrogen doped sample showed almost an eightfold enhancement in photocatalytic activity compared to undoped ZnO.

6. DOPED PEROVSKITE NANOPARTICLES

6.1. Synthesis and Structure of Doped Perovskite Nanoparticles. *6.1.1. Doped $BaTiO_3$ and $SrTiO_3$ Nanoparticles.* A variety of perovskite oxide nanoparticles have been synthesized recently that have exhibited good photocatalytic activity. However, just like most other metal oxides, their large bandgap confines their absorption to the UV region, and thus, doping is required to enhance their visible-light response. The most popular perovskite materials are $BaTiO_3$ and $SrTiO_3$; however, most doping studies have featured $SrTiO_3$. The synthesis methods for doped $BaTiO_3$ and $SrTiO_3$ nanoparticles can be summarized into two main approaches. The first approach is to start with a TTIP precursor, just like for TiO_2, along with nitrate salts of Ba/Sr and the dopants. For example, Ag-treated cubic $SrTiO_3$ nanoparticles were synthesized from TTIP, strontium nitrate, and silver nitrate via hydrothermal treatment.[155] TTIP was also used with strontium salts along with ruthenium and nickel chloride salts to obtain nanosized particulates of 1% Ru,Ni codoped $SrTiO_3$.[156] Using TTIP with barium nitrate and cerium nitrate led to the successful synthesis of uniform Ce-doped $BaTiO_3$ nanoparticles by Senthilkumar et al., as shown in Figure 11a.[158] The size increased gradually upon Ce doping of 0, 2, 4, and 6% from 109 to 127 nm, respectively. Doping with Ce at 4% shifted the diffraction peaks to a higher angle, indicating substitution of

https://dx.doi.org/10.1021/acsanm.0c01035
ACS Appl. Nano Mater. 2020, 3, 6156−6185

Ce^{3+} ions at Ba^{2+} sites, doping with Ce at 6% shifted the diffraction peaks to lower angles, indicating substitution of Ce^{3+}/Ce^{4+} ions at Ti^{3+}/Ti^{4+} ion sites. Separate theoretical studies by Zhou et al. have found it to be energetically more favorable for the metal ions to substitute for the Ti atoms, rather than the Sr atoms.[178]

The second approach is to start from commercial TiO_2 nanoparticles and use barium/strontium hydroxides or the carbonate salt of strontium mixed with the nitrate salts or oxides of the dopant metals. $BaTiO_3$ nanoparticles with 2% rhodium doping were synthesized by Nishioka et al. from three different commercial TiO_2 sources, including P25, submicrometer anatase, and nanorutile.[159] Barium hydroxide, which is one of the most common reagents used to convert TiO_2 into $BaTiO_3$, was used along with $Rh(NO_3)_3$ as the Rh source. The particles were well-dispersed and seemed to prefer a cube-like morphology, as shown in Figure 11b. All three commercial TiO_2 precursors yielded similar cubic perovskite $BaTiO_3$ particles after heating (Figure 11d). Heat treatment up to 1273 K increased the crystallinity of the nanoparticles followed by transformation into hexagonal $BaTiO_3$ upon heating further to 1423 K (Figure 11e). Similar cube-like nanoparticles were also obtained upon doping $SrTiO_3$ with Rh, starting with commercial P25 and $RhCl_3$, as shown in Figure 11c.[157] Crystalline cubic-phased particles were obtained in gram-scale quantities (1.2 g) with a yield of 44%, by simple hydrothermal synthesis without the need for calcination. Unit cell parameters gradually increased with increasing Rh doping percentage (Figure 11f). Analysis by XPS revealed the presence of Rh^{3+} species in the material and Rh^{4+} on the surface. Rhodium was also studied as a codopant with lanthanum by Wang et al.[97] A two-step method was used with commercially available rutile-type TiO_2 and $SrCO_3$ calcined together first to make $SrTiO_3$ followed by calcination with La_2O_3 and then again with Rh_2O_3. A one-step method where all the reagents were mixed together and then calcined together was also explored. The one-step method led to better incorporation of Rh into the structure. Cai et al. demonstrated a microwave-assisted method to achieve 5% La doping in $SrTiO_3$ as well as up to 8% codoping with Cr.[98] The nitrate salts of La and Cr were used here and treated with TiO_2 and commonly used $Sr(OH)_2$ in a microwave at 150 °C for 5 h under 800 W; cubic-phase $SrTiO_3$ was obtained. These studies found that La was doped into the Sr sites while Cr was doped into the Ti sites. Anion doping with nitrogen and sulfur mostly involves urea or thiourea as the precursors, respectively, similar to TiO_2. $SrTiO_3$ nanoparticles codoped with sulfur and nitrogen were prepared from commercial TiO_2 and $SrCO_3$ with thiourea.[86]

6.1.2. Doped Tantalum and Niobium Oxide Nanoparticles. Anion doping is the most common type of doping for the other perovskite oxide nanoparticles. Most anion-doped perovskite tantalum oxide particles have been prepared on the micrometer or powder scale, and only a handful of reports generate nanosized particles. Sulfur-doped $NaTaO_3$ nanoparticles were synthesized by Li et al. (Figure 12a),[161] where the Ta_2O_5 precursor with $Na_2S_2O_3{\cdot}5H_2O$ were heated in a Teflon-lined steel autoclave at 180 °C for 12 h to yield cubic nanoparticles with edge-lengths of 200−500 nm; the doping was achieved at 10%. The same precursors and reactions conditions were used by Wu et al. to synthesize C-doped $NaTaO_3$ nanoparticles, with ethylene glycol serving as the carbon source.[160] $NaTaO_3$ exists as three polymorphs: cubic, orthorhombic, and monoclinic. The C-doped particles

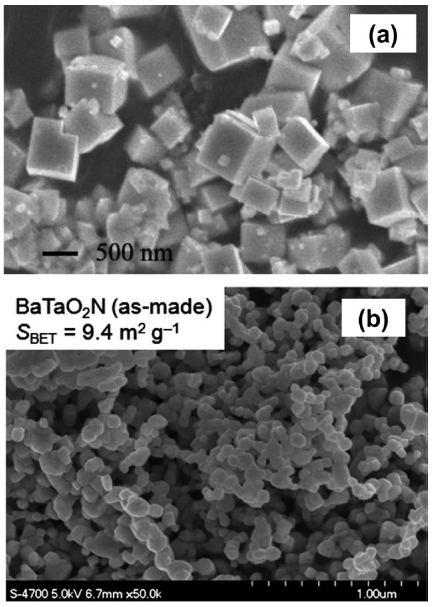

Figure 12. Morphology of doped tantalum oxide NPs. (a) SEM image of S-doped $NaTaO_3$ nanocubes. Adapted with permission from ref 161. Copyright 2015 Elsevier. (b) SEM image of N-doped $BaTaO_3$ NPs. Adapted with permission from ref 163. Copyright 2014 Elsevier.

maintained the orthorhombic phase of $NaTaO_3$, while S-doping seemed to adopt a structure closer to the cubic phase. For carbon doping, an interesting method utilizing microorganism chelation was used by Jia et al. to dope $LaCoO_3$.[25] Nitrate salts of La and Co were mixed with *B. lincheniformis* R08 biomass and citric acid to form a sol−gel, which was then polymerized, ground, and calcined to obtain perovskite-phase C-doped $LaCoO_3$ nanoparticles.

Thermal ammonolysis under flowing ammonia is the preferred method for the synthesis of N-doped tantalum and niobium oxide nanoparticles. Chen at al. synthesized N-doped $Sr_5Ta_4O_{15-x}N_x$ nanoparticles by using $TaCl_5$ and $SrCO_3$ with citric acid and ethylene glycol.[164] Flowing ammonia under high heat followed by calcination yielded the N-doped materials as irregularly shaped nanoparticles. Maeda et al. used a similar recipe with $TaCl_5$ while experimenting with $Ta(OC_2H_5)_5$ and $BaCO_3$ for N-doped $BaTaO_2N$ nanoparticles and found that the $Ta(OC_2H_5)_5$ precursor prevents the formation of a Ta_3N_5 byproduct, which was observed with the $TaCl_5$ precursor (Figure 12b).[163] Similar thermal ammonolysis by annealing under ammonia flow at 818 K for 3 h was used to synthesize 500−600 nm sized N-doped $NaNbO_3$ particles with nitrogen substitution occurring in the oxygen sites.[162] Nb_2O_5 and Na_2CO_3 precursors were used under a relatively high temperature of 1073 K, and further calcination at 1173 K was used to prepare $NaNbO_3$ nanoparticles. Thermal ammonolysis thus proves to be an easy yet effective way to achieve nitrogen doping, followed by calcination, in these types of materials.

6.2. Properties and Applications of Doped Perovskite Nanoparticles. *6.2.1. Doped $BaTiO_3$ and $SrTiO_3$ Nanoparticles.* The most popular wide bandgap perovskites are $BaTiO_3$ and $SrTiO_3$ with a bandgap of around 3.2 eV for both. These materials also undergo bandgap reduction upon doping. For example, the bandgap of $SrTiO_3$ nanoparticles gradually reduced from 3.19 to 2.92 eV, and visible-light absorption increased monotonically on increasing Rh doping until 10%.[157]

https://dx.doi.org/10.1021/acsanm.0c01035
ACS Appl. Nano Mater. 2020, 3, 6156−6185

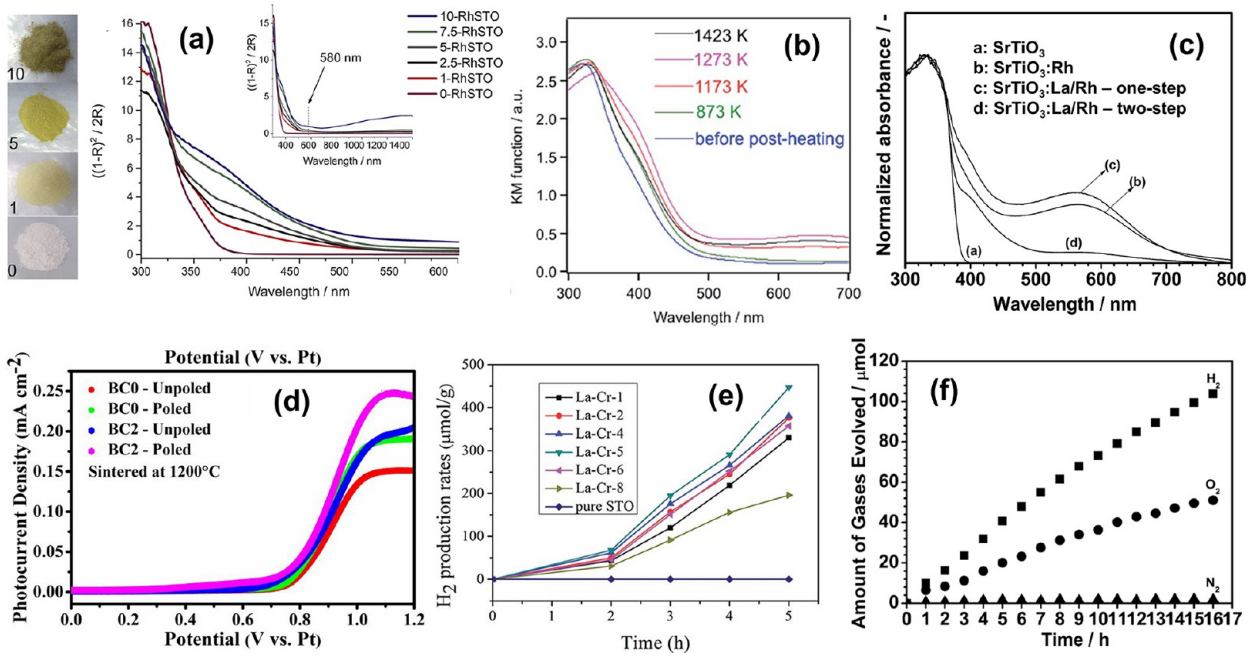

Figure 13. Optical properties and applications of doped $BaTiO_3$ and $SrTiO_3$ NPs. (a) UV−visible (inset: NIR) absorption spectra and color change upon doping for Rh-doped $SrTiO_3$ NPs. Adapted with permission from ref 157. 2017 Elsevier. (b) UV−visible DRS spectra of Rh-doped $BaTiO_3$ post heat treatment in the presence of additional barium hydroxide. Adapted with permission from ref 159. Copyright 2015 Royal Society of Chemistry. (c, f) DRS data for $SrTiO_3$ doped with Rh and La; and photocatalytic Z-scheme overall water splitting under sunlight with Ru-activated Rh and La codoped $SrTiO_3$ with Ir/CoO_x/Ta_3N_5 system. Adapted with permission from ref 97. Copyright 2014 American Chemical Society. (d) Photocurrent density curves and effect of polarization for Ce-doped $BaTiO_3$ NPs. Adapted with permission from ref 158. Copyright 2019 American Chemical Society. (e) Reaction time course of photocatalytic H_2 evolution from methanol for $SrTiO_3$ codoped with La and Cr. Adapted with permission from ref 98. Copyright 2015 Royal Society of Chemistry.

The nanoparticles developed a yellowish tinge with increasing Rh doping, shown in Figure 13a. The 20−50 nm sized cubic particles were used for photocatalytic reactions at wavelengths >420 nm and for killing *E. coli* bacteria. The best photocatalytic activity under visible illumination was observed for the 5% Rh-doped sample, which was comparable to the activity of P25 under UV light of similar intensity. The 5% Rh-doped $SrTiO_3$ sample also killed *E. coli* bacteria with 6 h of visible-light exposure. Rh-doped $BaTiO_3$ nanoparticles also showed similar spectra in the visible range with an absorption tail extending to 500 nm (Figure 13b).[159] Heat treatment at 1273 K extended the absorption furthest into the visible region. Photocatalytic H_2 evolution from methanol under visible-light irradiation was studied and was also found to be most effective for the nanoparticles heat-treated at 1273 K. High-temperature-induced crystallization decreases the density of defects that can act as recombination centers, leading to enhanced photocatalytic activity. In the case of $SrTiO_3$ nanoparticles, visible-light absorption was substantially more enhanced with Rh doping using a one-step method and even higher when codoped with La.[97] A wide absorption peak around 560−600 nm was observed with the tail extending up to 800 nm (Figure 13c). Heat treatment was once again found to be important, as the sample calcined at 1373 K for 6 h exhibited the highest photocatalytic activity, which was attributed to the absence of impurity phases and the dopant-enriched shell. Wang et al. developed a Z-scheme photocatalyst to split water into H_2 and O_2 by using Rh and La codoped $SrTiO_3$ with a Ir/CoO_x/Ta_3N_5 system, under irradiation up to 540 nm (Figure 13f).[97] Similarly, La was found to be a useful codopant with Cr in $SrTiO_3$ for H_2 production under visible light.[98] In these studies, 1−8% La,Cr codoped $SrTiO_3$ nanoparticles showed a yellowish tinge with increased doping percentage and an absorption shoulder extending to over 500 nm, while also lowering the bandgap to ∼2.8 eV. However, the best photocatalytic performance for H_2 evolution was observed for the 5% codoped sample (∼450 μmol/g), with Cr being the major contributor in the enhanced performance, and codoping with La enhancing H_2 evolution further (Figure 13e). However, among all doped $SrTiO_3$ nanoparticles, the lowest bandgap and widest visible absorption was observed in the case of Ru- and Ni-doped $SrTiO_3$, as reported by Joseph et al.[156] The 3d orbitals of Ni^{3+} and 4d orbitals of Ru^{3+} create additional donor levels near the valence band, lowering the bandgap to 1.9 and 2.13 eV, respectively. Overall, absorption throughout the visible region and NIR region was substantially enhanced. These nanoparticles were evaluated for rate of photocatalytic degradation of Congo red dye and textile industry effluent, where the rates were observed to decrease in the order Ni-$SrTiO_3$ > Ru-$SrTiO_3$ > TiO_2 > $SrTiO_3$.

Hydrogen production via photocatalytic water splitting was also found to be enhanced by Ce doping of $BaTiO_3$ nanoparticles.[158] Senthilkumar et al. found that the built-in electric field in ferroelectric Ce-doped $BaTiO_3$ assisted in photocatalytic dye degradation and PEC water splitting. The latter studies showed that the photoanode fabricated at 4 mol % exhibited high photocurrent density (1.45 $mAcm^{-2}$) and H_2 evolution (22.50 μmol h^{-1} cm^{-2}). Ce-doping in $BaTiO_3$ distorts the Ti−O_6 octahedra, leading to higher spontaneous and remnant polarization and d33 coefficient at 4 mol % due to the built-in electric field. Photocatalytic activity was evaluated under visible-light irradiation for the degradation of multiple

https://dx.doi.org/10.1021/acsanm.0c01035
ACS Appl. Nano Mater. 2020, 3, 6156−6185

dyes, revealing that the poled sample had superior activity, shown in Figure 13d. Poling creates a built-in electric field in ferroelectric $BaTiO_3$, hindering the recombination of charge carriers, which then leads to enhanced photodegradation. The built-in electric field and band bending in Ce-doped $BaTiO_3$ promotes fast carrier transport at the photoanode/electrolyte interface. The authors tested 2, 4, and 6% Ce-doped samples, and the 4% doped sample proved to be most effective for all applications. An LSPR-induced enhancement in visible-light absorption and photocatalytic activity for NO removal was also observed for Ag-treated $SrTiO_3$ nanocubes.[155]

Similar to TiO_2, doping perovskite oxide nanoparticles with anions such as N, S, and C have shown to lower the bandgap and improve visible-light activity. Doping with S and N in $SrTiO_3$ show additional absorption edges at 490 and 510 nm, respectively, and was found to decrease the bandgap to 2.37 eV.[86] Destruction of NO at 510 and 400 nm was found to be 10.9 and 7.7 times higher, respectively, than for pure $SrTiO_3$.

6.2.2. Doped Niobium and Tantalum Oxide NPs. Niobium and tantalum oxide nanoparticles are typically doped with nonmetals. Similar to nitrogen doping in $Sr_5Ti_4O_{15-x}N_x$ nanoparticles, nitrogen doping was found to enhance the visible-light absorption of $BaTaO_3$ and $NaNbO_3$ nanoparticles. In the case of the $BaTaO_3$ perovskite structure, N doping to form $BaTaO_2N$ led to a wide absorption peak up to 700 nm, while N-doping induced a tail up to about 600 nm in $NaNbO_3$ nanoparticles.[163] These nanoparticles were used for the degradation of 2-propanol to acetone and eventually to CO_2.[162] $BaTaO_2N$ was used in conjunction with $BaZrO_3$ in a solid solution for H_2 and O_2 evolution from water. Nitrogen doping also led to increased visible-light absorption by forming $Sr_5Ta_4O_{15-x}N_x$ and shifting the peak from 275 to 565 nm while substantially reducing the bandgap from 4.5 to 2.2 eV.[164] Similar absorption features were also reported with $Ba_5Ta_4O_{15-x}N_x$. These N-doped oxides were used to catalyze both the half reactions of splitting water under visible-light irradiation. Visible-light absorption was increased with an add-on-tail in $NaTaO_3$ upon 20% doping with sulfur, because sulfur 3p orbitals add additional levels above the valence band.[161] Photocatalytic performance gradually increased by about five times up to 20% S-doping and dropped slightly for the 30% doped sample. $NaTaO_3$ photocatalytic activity was also enhanced upon carbon doping in conjunction with Cl-doped TiO_2 for the decomposition of NO_x species under simulated solar illumination.[160] Diffuse reflectance spectra (DRS) showed an add-on-tail until about 600 nm. Carbon doping also improved visible-light absorption in $LaCoO_3$ with absorption thresholds at 574 nm compared to 411 nm for the undoped sample due to the partial substitution of O with C in the crystal lattice.[25] The bandgap decreased from 3.02 to 2.16 eV. Reduction of CO_2 was also greatly enhanced to yield formic acid, reaching 96 μmol/h/g under irradiation by a xenon lamp.

7. OTHER DOPED METAL OXIDE NANOPARTICLES

7.1. Synthesis and Structure of Other Doped Metal Oxide Nanoparticles. Many of the methods used above in the case of TiO_2, ZnO, and the perovskites have been found to be useful for other metal oxide nanoparticles as well. For example, the use of TTIP with ethylenediamine to produce N-doped TiO_2 nanoparticles can be translated to the synthesis of N-doped ZrO_2 and HfO_2 nanoparticles as well, by substituting with the isopropoxides of Zn and Hf, respectively.[166] The amount of N-doping can be controlled by the amount of acid (acetic acid) and base (KOH) added during hydrolysis. All of these doped oxide nanoparticles display clear diffraction peaks after sintering, consistent with $TiO_{2-x}N_x$, $ZrO_{2-x}N_x$, and $HfO_{2-x}N_x$ having anatase, cubic, and monoclinic structures, respectively. Nitrogen and sulfur codoping along with carbon in ZrO_2 nanoparticles was achieved using thiourea, similar to that observed with TiO_2 and $SrTiO_3$ nanoparticles.[76,86,165] For metal cation doping, the preference toward the nitrate salts was also observed as Eu doping was achieved in addition to C,N,S tridoping in ZrO_2 using $Eu(NO_3)_3{\cdot}6H_2O$.[165] A mixture of all nitrate salts of Zn, Fe, and Co with sodium borohydride was used to achieve Co-doped $ZnFe_2O_4$ nanoparticles.[108] Co ions were substituted into the Zn sites at 3, 10, 20, and 40% to yield cubic spinel-phase monocrystalline particles having 11 ± 3 nm diameters (Figure 14a). Generally, it is difficult to prevent aggregation in magnetic particles, compared to nonmagnetic metal oxides; however, Fan and coworkers were able to maintain good dispersion even after Co doping until 20%; however, the surface area dropped significantly for the sample doped at 40%, indicating nanoparticle aggregation. The nitrate salt of cerium was also effective for CeO_2 nanoparticle synthesis, which were doped with rare earth metals when combined with rare earth oxides during synthesis.[89] Another widely used metal oxide nanoparticle is tin oxide (SnO_2), which is typically made from tin chloride precursors. However, recently Medhi et al. discovered that tin oxide nanoparticles and doped tin oxide nanoparticles can be synthesized using sodium stannate as the precursor.[107] A simple hydrothermal method at 150 °C was employed in the presence of sodium antimonate and sodium zincate to obtain uniform and monodisperse antimony- and zinc-doped tin oxide nanoparticles (diameter ~40 nm), respectively, as shown in Figure 14b. The antimony-doped tin oxide nanoparticles (ATO)

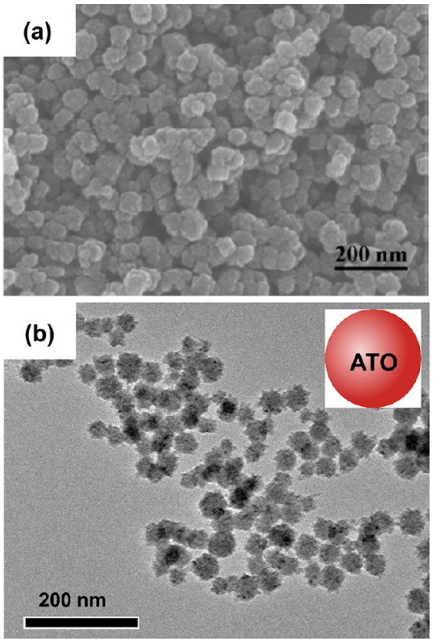

Figure 14. Morphology of other doped metal oxide NPs. (a) SEM image of Co-doped $ZnFe_2O_4$ NPs. Adapted with permission from ref 108. Copyright 2012 American Chemical Society. (b) TEM image of antimony-doped tin oxide NPs. Adapted with permission from ref 107. Copyright 2019 American Chemical Society.

https://dx.doi.org/10.1021/acsanm.0c01035
ACS Appl. Nano Mater. 2020, 3, 6156−6185

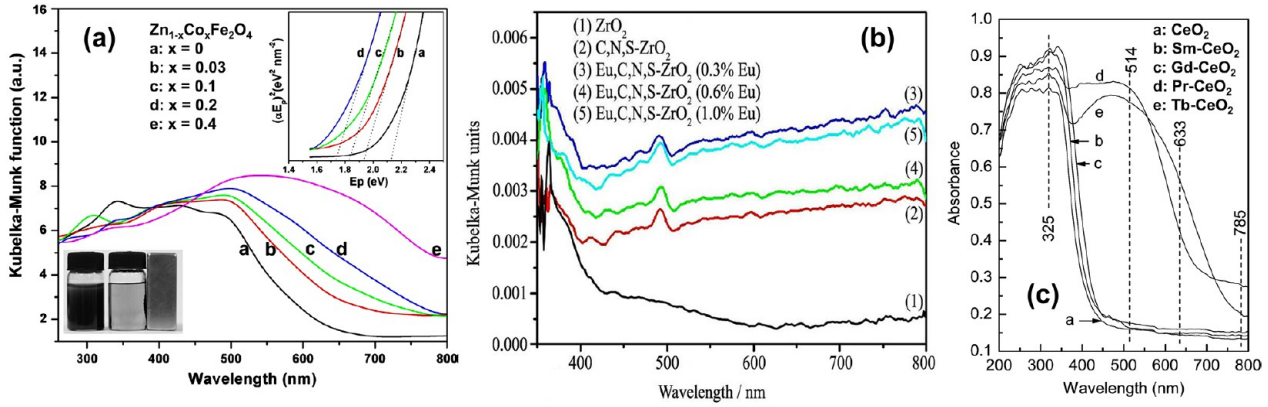

Figure 15. Properties of other doped metal oxide nanoparticles. (a) UV−visible absorption spectra of ferromagnetic Co-doped $ZnFe_2O_4$ NPs (insets show bandgap change and magnetic separation of catalyst). Adapted with permission from ref 108. Copyright 2012 American Chemical Society. (b) Absorption spectra of ZrO_2 NPs coped with C, N, S, and Eu. Adapted with permission from ref 165. Copyright 2015 Elsevier. (c) Absorption spectra of CeO_2 NPs doped with rare earth metals. Adapted with permission from ref 89. Copyright 2011 American Chemical Society.

retained the rutile phase of tin oxide, but the zinc-doped tin oxide nanoparticles (ZTO) adopted a $ZnSnO_3$ phase. The doping percentages could be systematically varied from zero to 13% and 9%, respectively, for the ATO and ZTO nanoparticles.[107] Overall, general trends in the synthesis schemes used by most groups that translate well for different metal oxide nanoparticles offer good insight for future synthetic strategies that will be needed for next-generation homogeneously doped metal oxide nanoparticles.

7.2. Properties and Applications of Other Doped Metal Oxide Nanoparticles. Doping has also proven to be an effective strategy to enhance visible-light utilization in ferrite nanoparticles and oxide nanoparticles of zirconium, cerium, hafnium, tin, and cobalt.[23,89,107,108,166] The visible-light activity of spinel magnetic ferrite $ZnFe_2O_4$ was enhanced upon Co doping by Fan et al.[108] The visible-light absorption intensity increases with Co doping, and there is red shift in the bandgap, as depicted in Figure 15a. The bandgap of undoped $ZnFe_2O_4$ NPs (2.13 eV) was greater than the bulk (1.9 eV) due to confinement, but progressively diminished upon Co doping to 1.73 eV. Co doping increased visible-light absorption intensity significantly in the 600−800 nm range (Figure 15a). Visible-light absorption was consistently observed to broaden with increasing Co doping. However, photocatalytic activity increased linearly for $Zn_{1-x}Co_xFe_2O_4$ until x = 0.2, but the x = 0.4 sample was less active than the undoped sample. These nanoparticles demonstrated room-temperature ferrimagnetism with the highest coercivity for the $Zn_{0.6}Co_{0.4}Fe_2O_4$ sample (~32 Oe) and saturation magnetization (~51 emu/g), which were significantly higher than the values for all other samples. However, higher ferrimagnetism in the x = 0.4 sample led to aggregation at this doping%, decreasing photocatalytic efficiency. With a saturation magnetization of ~14 emu/g, the optimal trade-off between photocatalytic efficiency and magnetic strength was found at x = 0.2, for application as a magnetically separable visible-light photocatalyst (Figure 15a inset).

Qiu et al. conducted a comparative study of N-doped TiO_2, ZrO_2, and HfO_2 nanoparticles. DRS spectra and difference DRS data (subtracting the reflectance spectra of nondoped from the doped samples) were used to determine the impact of N-doping. The most significant improvement in visible-light absorption upon N-doping in these nanoparticles was observed for ZrO_2 followed by TiO_2 and then HfO_2.[166] While N-doping improved the photocatalytic activity for all three oxides, TiO_2 being the better photocatalyst, showed the best photocatalytic activity among the three oxides, even after doping. The visible-light absorption in ZrO_2 was also significantly enhanced by C,N,S tridoping and improved further by combining Eu doping with C,N,S doping (Figure 15b).[165] These nanoparticles were used for the photocatalytic degradation of indigo carmine. The transparent conducting oxide SnO_2 is transparent in the visible to near-IR regions. However, the antimony-doped tin oxide nanoparticles synthesized by Medhi et al. demonstrated an absorption tail until 700 nm.[107] The bandgaps were also lowered upon doping by antimony and zinc. Similar to Sn doping in In_2O_3, Sb doping in SnO_2 shifts the Fermi level into the single dispersive CB of SnO_2, giving rise to a significant increase in carrier concentration and mobility.[107] In the case of CeO_2 nanoparticles doped with rare earth metals, no improvement in visible-light absorption was observed upon doping with Sm and Gd, but significant absorption broadening was observed upon doping with Pr and Tb, as shown in Figure 15c.[89]

Another metal oxide nanoparticle that is less widely used as a parent metal oxide is cobalt oxide. As noted above, Co is a popular dopant for TiO_2 and ZnO nanoparticles largely because cobalt oxide already has a bandgap in the visible range, which can be further tuned by doping. Additionally, cobalt is a metal with variable oxidation states and possess impressive catalytic properties, widely exploited in the field of organometallic catalysis. The S-doped CoO/Co_3O_4 nanoparticles synthesized by Choi et al. showed photocatalytic efficiency for CO_2 reduction to methane that was 2.7 times greater than the undoped analogs, even in the absence of a hole scavenger.[23] These studies demonstrate that doped cobalt oxide nanoparticles have great promise for use as visible-light-active photocatalysts.

8. SUMMARY

As described in this review, much useful research on the synthesis and applications of doped metal oxide nanoparticles has been conducted. Surprisingly, hollow, porous, or mesoporous nanospheres are often easier to synthesize than solid nanoparticles. Nevertheless, heat treatment in the form of sintering or annealing at high temperatures is invariably needed to obtain crystalline nanoparticles. Increased mobility of charge

https://dx.doi.org/10.1021/acsanm.0c01035
ACS Appl. Nano Mater. 2020, 3, 6156−6185

carriers and lower density of defects in more crystalline nanoparticles lead to reduced recombination and therefore enhanced photocatalytic activity. Hydrothermal/solvothermal syntheses are the most popular methods for preparing doped metal oxide nanoparticles, owing largely to their simplicity and potential for scale up. Sol−gel methods are also commonly used, while the oleic acid/oleyl amine method provides a powerful approach for large-scale synthesis of uniform nanoparticles with fine control over their shape and size. Doping was observed to be an effective strategy to enhance visible-light absorption via three main modes: (1) a red shift of the bandgap into the visible region, (2) an absorption tail extending into visible wavelengths, and/or (3) the introduction of new absorption peaks in the visible region. Nitrogen is the most commonly studied dopant for all of the metal oxide nanoparticles, commonly achieved via ammonolysis or by using ethylenediamine, which leads to enhanced visible-light absorption. Sulfur, carbon, and fluorine are the other commonly used nonmetal dopants used to promote visible-light activity. Metal ion doping, especially with a variety of transition metals, has also been effectively utilized for this purpose. Many studies have also found that doping can also reduce electron−hole recombination. While visible-light absorption typically increases with doping percentage, there is often a peak doping percentage beyond which photocatalytic efficiency decreases due to the creation of extra recombination centers at higher doping percentages. Visible-light absorption can also be hampered in some cases at high doping percentages. In practice, the optimum doping percentage varies from nanoparticle system to nanoparticle system and from dopant to dopant and is also affected by the synthesis protocol. These doped nanoparticles with their enhanced visible-light absorption were utilized for a variety of applications such as the photocatalytic degradation of dyes, water splitting, H_2 evolution from a variety of sources, reduction of CO_2, gas sensing, and antibacterial treatment.

At a glance, one might be tempted to conclude that any kind of doping improves the visible-light performance of metal oxides; however, the studies covered in this review show that doping can also hamper performance by causing aggregation, diminishing absorption, and increasing recombination. Instead of narrowing the bandgap, heavy doping in metal oxides can also lead to a wider bandgap due to structural changes or a Moss−Burstein shift.[179−182] Just like the tendency for unnecessary exploration with various dopants in graphene, as recently pointed out by Wang et al.,[183] researchers should also avoid needless doping in metal oxide nanoparticles, and a careful balance between the positive and negative effects of doping needs to be found. The criteria for selecting a dopant depends on several different factors. Nonmetals have proven to be convenient dopants for narrowing the bandgap of metal oxides while maintaining morphological consistency. However, metal dopants give rise to stronger visible light absorption both as monodopants and codopants; nonmetal dopant effects are also enhanced when codoped with metals. Recent advances with nonaqueous synthetic methods have allowed for the synthesis of metal doped, codoped, and tridoped nanoparticles having uniform morphologies and narrow size distributions. Chemical similarities of the dopant with the parent metal (in terms of ionic size, atomic structure, and coordination preferences) facilitate the generation of doped nanoparticles with fewer defects and recombination centers. Therefore, transition metals are powerful dopants in TiO_2, ZnO, $BaTiO_3$, and $SrTiO_3$ nanoparticles for photocatalysis. For electrical applications, along with structural similarities leading to fewer defects, doping with relatively electron-rich metals is also preferred because it raises the Fermi level, leading to higher conduction.

As evident from the research covered in this review, the groundwork for the synthesis and study of doped metal oxide nanoparticles with visible-light activity is there. There now await many opportunities for the synthesis of new doped metal oxide nanoparticle systems, combining various dopants, for further enhancing the visible-light activity along with inducing additional properties including magnetism. For example, new photocatalysts that combine the effects of codoping with carefully tailored hybrid heterojunctions are likely to emerge. Hybrid nanostructures comprised of doped metal oxides along with noble metal plasmonic nanoparticles, carbon nanotubes, conducting polymers, graphene oxide, and reduced graphene oxide also promise to be at the forefront of photoresponsive nanomaterials research. A comprehensive understanding of readily manufacturable doped metal oxide nanoparticles opens the door to all these possibilities. Undoubtedly, we will continue to see creative advances in this promising field of research.

AUTHOR INFORMATION

Corresponding Author

T. Randall Lee − *Department of Chemistry and the Texas Center for Superconductivity, University of Houston, Houston, Texas 77204-5003, United States;* orcid.org/0000-0001-9584-8861; Email: trlee@uh.edu

Authors

Riddhiman Medhi − *Department of Chemistry and the Texas Center for Superconductivity, University of Houston, Houston, Texas 77204-5003, United States;* orcid.org/0000-0002-2368-2468

Maria D. Marquez − *Department of Chemistry and the Texas Center for Superconductivity, University of Houston, Houston, Texas 77204-5003, United States*

Complete contact information is available at: https://pubs.acs.org/10.1021/acsanm.0c01035

Notes

The authors declare no competing financial interest.

ACKNOWLEDGMENTS

We thank the Air Force Office of Scientific Research (AFOSR FA9550-18-1-0094, the Robert A. Welch Foundation (E-1320), the Texas Center for Superconductivity at the University of Houston, and the University of Houston Advanced Manufacturing Institute for generously supporting this research.

REFERENCES

(1) Wang, C. S.; Klein, B. M. First-Principles Electronic Structure of Si, Ge, GaP, GaAs, ZnS, and ZnSe. I. Self-Consistent Energy Bands, Charge Densities, and Effective Masses. *Phys. Rev. B: Condens. Matter Mater. Phys.* **1981**, *24*, 3393−3416.

(2) Yu, K. J.; Yan, Z.; Han, M.; Rogers, J. A. Inorganic Semiconducting Materials for Flexible and Stretchable Electronics. *npj Flexible Electron.* **2017**, *1*, 4.

(3) Zhou, Z.; Lan, C.; Wei, R.; Ho, J. C. Transparent Metal-Oxide Nanowires and Their Applications in Harsh Electronics. *J. Mater. Chem. C* **2019**, *7*, 202−217.
(4) Millán, J.; Godignon, P. In Wide Bandgap Power Semiconductor Devices. *2013 Spanish Conference on Electron Devices* **2013**, 293−296.
(5) Shenai, K.; Scott, R. S.; Baliga, B. J. Optimum Semiconductors for High-Power Electronics. *IEEE Trans. Electron Devices* **1989**, *36*, 1811−1823.
(6) Gu, C.; Wheeler, P.; Castellazzi, A.; Watson, A. J.; Effah, F. Semiconductor Devices in Solid-State/Hybrid Circuit Breakers: Current Status and Future Trends. *Energies* **2017**, *10*, 495.
(7) Neudeck, P. G.; Okojie, R. S.; Liang-Yu, C. High-Temperature Electronics - A Role for Wide Bandgap Semiconductors? *Proc. IEEE* **2002**, *90*, 1065−1076.
(8) Rajbhandari, S.; McKendry, J. J. D.; Herrnsdorf, J.; Chun, H.; Faulkner, G.; Haas, H.; Watson, I. M.; O'Brien, D.; Dawson, M. D. A Review of Gallium Nitride LEDs for Multi-Gigabit-Per-Second Visible Light Data Communications. *Semicond. Sci. Technol.* **2017**, *32*, 023001.
(9) Guo, Y.; Ma, L.; Mao, K.; Ju, M.; Bai, Y.; Zhao, J.; Zeng, X. C. Eighteen Functional Monolayer Metal Oxides: Wide Bandgap Semiconductors with Superior Oxidation Resistance and Ultrahigh Carrier Mobility. *Nanoscale Horiz.* **2019**, *4*, 592−600.
(10) Ray, C.; Pal, T. Recent Advances of Metal−Metal Oxide Nanocomposites and their Tailored Nanostructures in Numerous Catalytic Applications. *J. Mater. Chem. A* **2017**, *5*, 9465−9487.
(11) Ganguly, A.; Anjaneyulu, O.; Ojha, K.; Ganguli, A. K. Oxide-Based Nanostructures for Photocatalytic and Electrocatalytic Applications. *CrystEngComm* **2015**, *17*, 8978−9001.
(12) Liu, Y.; Wang, W.; Xu, X.; Marcel Veder, J.-P.; Shao, Z. Recent Advances in Anion-Doped Metal Oxides for Catalytic Applications. *J. Mater. Chem. A* **2019**, *7*, 7280−7300.
(13) Yu, X.; Marks, T. J.; Facchetti, A. Metal Oxides for Optoelectronic Applications. *Nat. Mater.* **2016**, *15*, 383−396.
(14) Dixon, S. C.; Scanlon, D. O.; Carmalt, C. J.; Parkin, I. P. n-Type Doped Transparent Conducting Binary Oxides: An Overview. *J. Mater. Chem. C* **2016**, *4*, 6946−6961.
(15) Lu, Q.; Yu, Y.; Ma, Q.; Chen, B.; Zhang, H. 2D Transition-Metal-Dichalcogenide-Nanosheet-Based Composites for Photocatalytic and Electrocatalytic Hydrogen Evolution Reactions. *Adv. Mater.* **2016**, *28*, 1917−1933.
(16) Ola, O.; Maroto-Valer, M. M. Review of Material Design and Reactor Engineering on TiO_2 Photocatalysis for CO_2 Reduction. *J. Photochem. Photobiol., C* **2015**, *24*, 16−42.
(17) Park, K.-W.; Kolpak, A. M. Optimal Methodology for Explicit Solvation Prediction of Band Edges of Transition Metal Oxide Photocatalysts. *Commun. Chem.* **2019**, *2*, 79.
(18) Fresno, F.; Jana, P.; Reñones, P.; Coronado, J. M.; Serrano, D. P.; de la Peña O'Shea, V. A. CO_2 Reduction over $NaNbO_3$ and $NaTaO_3$ Perovskite Photocatalysts. *Photochem. Photobiol. Sci.* **2017**, *16*, 17−23.
(19) Kanhere, P.; Chen, Z. A Review on Visible Light Active Perovskite-Based Photocatalysts. *Molecules* **2014**, *19*, 19995−20022.
(20) Sherly, E. D.; Vijaya, J. J.; Kennedy, L. J. Effect of CeO_2 Coupling on the Structural, Optical and Photocatalytic Properties of ZnO Nanoparticle. *J. Mol. Struct.* **2015**, *1099*, 114−125.
(21) Di Paola, A.; Bellardita, M.; Palmisano, L. Brookite, the Least Known TiO_2 Photocatalyst. *Catalysts* **2013**, *3*, 36−73.
(22) Kurien, U.; Hu, Z.; Lee, H.; Dastoor, A. P.; Ariya, P. A. Radiation Enhanced Uptake of Hg0(g) on Iron (Oxyhydr)oxide Nanoparticles. *RSC Adv.* **2017**, *7*, 45010−45021.
(23) Choi, J. Y.; Lim, C. K.; Park, B.; Kim, M.; Jamal, A.; Song, H. Surface Activation of Cobalt Oxide Nanoparticles for Photocatalytic Carbon Dioxide Reduction to Methane. *J. Mater. Chem. A* **2019**, *7*, 15068−15072.
(24) Qin, J.; Lin, L.; Wang, X. A Perovskite Oxide $LaCoO_3$ Cocatalyst for Efficient Photocatalytic Reduction of CO_2 with Visible Light. *Chem. Commun.* **2018**, *54*, 2272−2275.
(25) Jia, L.; Li, J.; Fang, W.; Song, H.; Li, Q.; Tang, Y. Visible-Light-Induced Photocatalyst Based on C-Doped $LaCoO_3$ Synthesized by Novel Microorganism Chelate Method. *Catal. Commun.* **2009**, *10*, 1230−1234.
(26) Lu, Q.; Mu, Y.; Roberts, W. J.; Althobaiti, M.; Dhanak, R. V.; Wu, J.; Zhao, C.; Zhao, Z. C.; Zhang, Q.; Yang, L.; Mitrovic, Z. I.; Taylor, S.; Chalker, R. P. Electrical Properties and Interfacial Studies of $Hf_xTi_{1-x}O_2$ High Permittivity Gate Insulators Deposited on Germanium Substrates. *Materials* **2015**, *8*, 8169−8182.
(27) Arimi, A.; Megatif, L.; Granone, L. I.; Dillert, R.; Bahnemann, D. W. Visible-Light Photocatalytic Activity of Zinc Ferrites. *J. Photochem. Photobiol., A* **2018**, *366*, 118−126.
(28) Valenti, M.; Jonsson, M. P.; Biskos, G.; Schmidt-Ott, A.; Smith, W. A. Plasmonic Nanoparticle-Semiconductor Composites for Efficient Solar Water Splitting. *J. Mater. Chem. A* **2016**, *4*, 17891−17912.
(29) Han, F.; Kambala, V. S. R.; Srinivasan, M.; Rajarathnam, D.; Naidu, R. Tailored Titanium Dioxide Photocatalysts for the Degradation of Organic Dyes in Wastewater Treatment: A Review. *Appl. Catal., A* **2009**, *359*, 25−40.
(30) Serpone, N. Is the Bandgap of Pristine TiO_2 Narrowed by Anion- and Cation-Doping of Titanium Dioxide in Second-Generation Photocatalysts? *J. Phys. Chem. B* **2006**, *110*, 24287−24293.
(31) Chiu, Y.-H.; Lai, T.-H.; Chen, C.-Y.; Hsieh, P.-Y.; Ozasa, K.; Niinomi, M.; Okada, K.; Chang, T.-F. M.; Matsushita, N.; Sone, M.; Hsu, Y.-J. Fully Depleted Ti−Nb−Ta−Zr−O Nanotubes: Interfacial Charge Dynamics and Solar Hydrogen Production. *ACS Appl. Mater. Interfaces* **2018**, *10*, 22997−23008.
(32) Bhachu, D. S.; Sankar, G.; Parkin, I. P. Aerosol Assisted Chemical Vapor Deposition of Transparent Conductive Zinc Oxide Films. *Chem. Mater.* **2012**, *24*, 4704−4710.
(33) Babar, A. R.; Shinde, S. S.; Moholkar, A. V.; Bhosale, C. H.; Kim, J. H.; Rajpure, K. Y. Physical Properties of Sprayed Antimony Doped Tin Oxide Thin Films: The Role of Thickness. *J. Semicond.* **2011**, *32*, 053001.
(34) Obaida, M.; Moussa, I.; Boshta, M. Low Sheet Resistance F-Doped SnO_2 Thin Films Deposited by Novel Spray Pyrolysis Technique. *Int. J. Chem. Tech Res.* **2015**, *8*, 239−247.
(35) Yao, Z.; Jia, F.; Tian, S.; Li, C.; Jiang, Z.; Bai, X. Microporous Ni−Doped TiO_2 film Photocatalyst by Plasma Electrolytic Oxidation. *ACS Appl. Mater. Interfaces* **2010**, *2*, 2617−2622.
(36) Biener, J.; Wittstock, A.; Baumann, F. T.; Weissmüller, J.; Bäumer, M.; Hamza, V. A. Surface Chemistry in Nanoscale Materials. *Materials* **2009**, *2*, 2404−2428.
(37) Parida, K. M.; Martha, S.; Das, D. P.; Biswal, N. Facile Fabrication of Hierarchical N-Doped GaZn Mixed Oxides for Water Splitting Reactions. *J. Mater. Chem.* **2010**, *20*, 7144−7149.
(38) Martha, S.; Chandra Sahoo, P.; Parida, K. M. An Overview on Visible Light Responsive Metal Oxide Based Photocatalysts for Hydrogen Energy Production. *RSC Adv.* **2015**, *5*, 61535−61553.
(39) Javid, A.; Kumar, M.; Ashraf, M.; Lee, J. H.; Han, J. G. Photocatalytic Antibacterial Study of N-Doped TiO_2 Thin Films Synthesized by ICP Assisted Plasma Sputtering Method. *Phys. E* **2019**, *106*, 187−193.
(40) Pany, S.; Parida, K. M. Sulfate-Anchored Hierarchical Meso−Macroporous N-doped TiO_2: A Novel Photocatalyst for Visible Light H_2 Evolution. *ACS Sustainable Chem. Eng.* **2014**, *2*, 1429−1438.
(41) Parida, K. M.; Pany, S.; Naik, B. Green Synthesis of Fibrous Hierarchical Meso-Macroporous N Doped TiO_2 Nanophotocatalyst with Enhanced Photocatalytic H_2 Production. *Int. J. Hydrogen Energy* **2013**, *38*, 3545−3553.
(42) Li, C.-H.; Li, M.-C.; Liu, S.-P.; Jamison, A. C.; Lee, D.; Lee, T. R.; Lee, T.-C. Plasmonically Enhanced Photocatalytic Hydrogen Production from Water: The Critical Role of Tunable Surface Plasmon Resonance from Gold−Silver Nanoshells. *ACS Appl. Mater. Interfaces* **2016**, *8*, 9152−9161.
(43) Baer, D. R.; Engelhard, M. H.; Johnson, G. E.; Laskin, J.; Lai, J.; Mueller, K.; Munusamy, P.; Thevuthasan, S.; Wang, H.; Washton, N.;

https://dx.doi.org/10.1021/acsanm.0c01035
ACS Appl. Nano Mater. 2020, 3, 6156−6185

Elder, A.; Baisch, B. L.; Karakoti, A.; Kuchibhatla, S. V. N. T.; Moon, D. Surface Characterization of Nanomaterials and Nanoparticles: Important Needs and Challenging Opportunities. *J. Vac. Sci. Technol., A* **2013**, *31*, 50820−50820.
(44) García-Mota, M.; Vojvodic, A.; Abild-Pedersen, F.; Nørskov, J. K. Electronic Origin of the Surface Reactivity of Transition-Metal-Doped TiO_2(110). *J. Phys. Chem. C* **2013**, *117*, 460−465.
(45) Talapin, D. V.; Shevchenko, E. V. Introduction: Nanoparticle Chemistry. *Chem. Rev.* **2016**, *116*, 10343−10345.
(46) Jeevanandam, J.; Barhoum, A.; Chan, Y. S; Dufresne, A.; Danquah, M. K Review on Nanoparticles and Nanostructured Materials: History, Sources, Toxicity and Regulations. *Beilstein J. Nanotechnol.* **2018**, *9*, 1050−1074.
(47) Srinoi, P.; Chen, Y.-T.; Vittur, V.; Marquez, D. M.; Lee, R. T. Bimetallic Nanoparticles: Enhanced Magnetic and Optical Properties for Emerging Biological Applications. *Appl. Sci.* **2018**, *8*, 1106.
(48) Freitas, J. N.; Gonçalves, A. S.; Nogueira, A. F. A Comprehensive Review of the Application of Chalcogenide Nanoparticles in Polymer Solar Cells. *Nanoscale* **2014**, *6*, 6371−6397.
(49) Dong, H.; Chen, Y. C.; Feldmann, C. Polyol Synthesis of Nanoparticles: Status and Options Regarding Metals, Oxides, Chalcogenides, and Non-Metal Elements. *Green Chem.* **2015**, *17*, 4107−4132.
(50) Bryan, W. W.; Medhi, R.; Marquez, M. D.; Rittikulsittichai, S.; Tran, M.; Lee, T. R. Porous Silver-Coated pNIPAM-co-AAc Hydrogel Nanocapsules. *Beilstein J. Nanotechnol.* **2019**, *10*, 1973−1982.
(51) Georgakilas, V.; Perman, J. A.; Tucek, J.; Zboril, R. Broad Family of Carbon Nanoallotropes: Classification, Chemistry, and Applications of Fullerenes, Carbon Dots, Nanotubes, Graphene, Nanodiamonds, and Combined Superstructures. *Chem. Rev.* **2015**, *115*, 4744−4822.
(52) Ha, M.; Kim, J.-H.; You, M.; Li, Q.; Fan, C.; Nam, J.-M. Multicomponent Plasmonic Nanoparticles: From Heterostructured Nanoparticles to Colloidal Composite Nanostructures. *Chem. Rev.* **2019**, *119*, 12208−12278.
(53) Wu, F.; Bai, J.; Feng, J.; Xiong, S. Porous Mixed Metal Oxides: Design, Formation Mechanism, and Application in Lithium-Ion Batteries. *Nanoscale* **2015**, *7*, 17211−17230.
(54) Zhang, S.; Leem, G.; Srisombat, L.-o.; Lee, T. R. Rationally Designed Ligands that Inhibit the Aggregation of Large Gold Nanoparticles in Solution. *J. Am. Chem. Soc.* **2008**, *130*, 113−120.
(55) Kvítek, L.; Panáček, A.; Soukupová, J.; Kolář, M.; Večeřová, R.; Prucek, R.; Holecová, M.; Zbořil, R. Effect of Surfactants and Polymers on Stability and Antibacterial Activity of Silver Nanoparticles (NPs). *J. Phys. Chem. C* **2008**, *112*, 5825−5834.
(56) Mahmoud, M. A.; El-Sayed, M. A.; Gao, J.; Landman, U. High-Frequency Mechanical Stirring Initiates Anisotropic Growth of Seeds Requisite for Synthesis of Asymmetric Metallic Nanoparticles like Silver Nanorods. *Nano Lett.* **2013**, *13*, 4739−4745.
(57) Chen, Y.-T.; Medhi, R.; Nekrashevich, I.; Litvinov, D.; Xu, S.; Lee, T. R. Specific Detection of Proteins Using Exceptionally Responsive Magnetic Particles. *Anal. Chem.* **2018**, *90*, 6749−6756.
(58) Wang, D.; Xie, T.; Li, Y. Nanocrystals: Solution-Based Synthesis and Applications as Nanocatalysts. *Nano Res.* **2009**, *2*, 30−46.
(59) Hayashi, H.; Hakuta, Y. Hydrothermal Synthesis of Metal Oxide Nanoparticles in Supercritical Water. *Materials* **2010**, *3*, 3794−3817.
(60) Gan, Y. X.; Jayatissa, A. H.; Yu, Z.; Chen, X.; Li, M. Hydrothermal Synthesis of Nanomaterials. *J. Nanomater.* **2020**, *2020*, 8917013.
(61) Mirzaei, A.; Neri, G. Microwave-Assisted Synthesis of Metal Oxide Nanostructures for Gas Sensing Application: A Review. *Sens. Actuators, B* **2016**, *237*, 749−775.
(62) Gupta, S.; Tripathi, M. A Review on the Synthesis of TiO_2 Nanoparticles by Solution Route. *Open Chem.* **2012**, *10*, 279−294.
(63) Rajput, N. Methods of Preparation of Nanoparticles − A Review. *IJAET* **2015**, *7*, 1806−1811.
(64) Lee, M.; Yun, H. J.; Yu, S.; Yi, J. Enhancement in Photocatalytic Oxygen Evolution via Water Oxidation under Visible Light on Nitrogen-Doped TiO_2 Nanorods with Dominant Reactive {102} Facets. *Catal. Commun.* **2014**, *43*, 11−15.
(65) Wu, Z.; Dong, F.; Zhao, W.; Wang, H.; Liu, Y.; Guan, B. The Fabrication and Characterization of Novel Carbon Doped TiO_2 Nanotubes, Nanowires and Nanorods with High Visible Light Photocatalytic Activity. *Nanotechnology* **2009**, *20*, 235701.
(66) Kim, S.; Hwang, S.-J.; Choi, W. Visible Light Active Platinum-Ion-Doped TiO_2 Photocatalyst. *J. Phys. Chem. B* **2005**, *109*, 24260−24267.
(67) Djerdj, I.; Arčon, D.; Jagličić, Z.; Niederberger, M. Nonaqueous Synthesis of Metal Oxide Nanoparticles: Short Review and Doped Titanium Dioxide as Case Study for the Preparation of Transition Metal-Doped Oxide Nanoparticles. *J. Solid State Chem.* **2008**, *181*, 1571−1581.
(68) Pinna, N.; Garnweitner, G.; Antonietti, M.; Niederberger, M. Non-Aqueous Synthesis of High-Purity Metal Oxide Nanopowders Using an Ether Elimination Process. *Adv. Mater.* **2004**, *16*, 2196−2200.
(69) Stefik, M.; Heiligtag, F. J.; Niederberger, M.; Grätzel, M. Improved Nonaqueous Synthesis of TiO_2 for Dye-Sensitized Solar Cells. *ACS Nano* **2013**, *7*, 8981−8989.
(70) Leem, G.; Sarangi, S.; Zhang, S.; Rusakova, I.; Brazdeikis, A.; Litvinov, D.; Lee, T. R. Surfactant-Controlled Size and Shape Evolution of Magnetic Nanoparticles. *Cryst. Growth Des.* **2009**, *9*, 32−34.
(71) Staller, C. M.; Robinson, Z. L.; Agrawal, A.; Gibbs, S. L.; Greenberg, B. L.; Lounis, S. D.; Kortshagen, U. R.; Milliron, D. J. Tuning Nanocrystal Surface Depletion by Controlling Dopant Distribution as a Route Toward Enhanced Film Conductivity. *Nano Lett.* **2018**, *18*, 2870−2878.
(72) Pradeev raj, K.; Sadaiyandi, K.; Kennedy, A.; Sagadevan, S.; Chowdhury, Z. Z.; Johan, M. R. B.; Aziz, F. A.; Rafique, R. F.; Thamiz Selvi, R.; Rathina bala, R. Influence of Mg Doping on ZnO Nanoparticles for Enhanced Photocatalytic Evaluation and Antibacterial Analysis. *Nanoscale Res. Lett.* **2018**, *13*, 229.
(73) Achouri, F.; Corbel, S.; Balan, L.; Mozet, K.; Girot, E.; Medjahdi, G.; Said, M. B.; Ghrabi, A.; Schneider, R. Porous Mn-doped ZnO Nanoparticles for Enhanced Solar and Visible Light Photocatalysis. *Mater. Des.* **2016**, *101*, 309−316.
(74) Albrbar, A. J.; Djokić, V.; Bjelajac, A.; Kovač, J.; Ćirković, J.; Mitrić, M.; Janaćković, D.; Petrović, R. Visible-Light Active Mesoporous, Nanocrystalline N, S-Doped and Co-Doped Titania Photocatalysts Synthesized by Non-Hydrolytic Sol-Gel Route. *Ceram. Int.* **2016**, *42*, 16718−16728.
(75) Macías-Sánchez, J. J.; Hinojosa-Reyes, L.; Caballero-Quintero, A.; de la Cruz, W.; Ruiz-Ruiz, E.; Hernández-Ramírez, A.; Guzmán-Mar, J. L. Synthesis of Nitrogen-Doped ZnO by Sol−Gel Method: Characterization and its Application on Visible Photocatalytic Degradation of 2,4-D and Picloram Herbicides. *Photochem. Photobiol. Sci.* **2015**, *14*, 536−542.
(76) Lin, X.; Fu, D.; Hao, L.; Ding, Z. Synthesis and Enhanced Visible-Light Responsive of C, N, S-Tridoped TiO_2 Hollow Spheres. *J. Environ. Sci.* **2013**, *25*, 2150−2156.
(77) Chen, H.; Dawson, J. A. Nature of Nitrogen-Doped Anatase TiO_2 and the Origin of Its Visible-Light Activity. *J. Phys. Chem. C* **2015**, *119*, 15890−15895.
(78) Yang, K.; Dai, Y.; Huang, B. Understanding Photocatalytic Activity of S- and P-Doped TiO_2 under Visible Light from First-Principles. *J. Phys. Chem. C* **2007**, *111*, 18985−18994.
(79) Leijtens, T.; Eperon, G. E.; Barker, A. J.; Grancini, G.; Zhang, W.; Ball, J. M.; Kandada, A. R. S.; Snaith, H. J.; Petrozza, A. Carrier Trapping and Recombination: The Role of Defect Physics in Enhancing the Open Circuit Voltage of Metal Halide Perovskite Solar Cells. *Energy Environ. Sci.* **2016**, *9*, 3472−3481.
(80) Sajjad, M.; Ullah, I.; Khan, M. I.; Khan, J.; Khan, M. Y.; Qureshi, M. T. Structural and Optical Properties of Pure and Copper Doped Zinc Oxide Nanoparticles. *Results Phys.* **2018**, *9*, 1301−1309.

https://dx.doi.org/10.1021/acsanm.0c01035
ACS Appl. Nano Mater. 2020, 3, 6156−6185

(81) Carrettin, S.; Hao, Y.; Aguilar-Guerrero, V.; Gates, B. C.; Trasobares, S.; Calvino, J. J.; Corma, A. Increasing the Number of Oxygen Vacancies on TiO_2 by Doping with Iron Increases the Activity of Supported Gold for CO Oxidation. *Chem. - Eur. J.* **2007**, *13*, 7771−7779.
(82) Takanabe, K. Photocatalytic Water Splitting: Quantitative Approaches toward Photocatalyst by Design. *ACS Catal.* **2017**, *7*, 8006−8022.
(83) Benjwal, P.; Kar, K. K. Removal of Methylene Blue from Wastewater under a Low Power Irradiation Source by Zn, Mn Co-Doped TiO_2 Photocatalysts. *RSC Adv.* **2015**, *5*, 98166−98176.
(84) Faraz, M.; Naqvi, F. K.; Shakir, M.; Khare, N. Synthesis of Samarium-Doped Zinc Oxide Nanoparticles with Improved Photocatalytic Performance and Recyclability under Visible Light Irradiation. *New J. Chem.* **2018**, *42*, 2295−2305.
(85) Jaiswal, R.; Bharambe, J.; Patel, N.; Dashora, A.; Kothari, D. C.; Miotello, A. Copper and Nitrogen Co-Doped TiO_2 Photocatalyst with Enhanced Optical Absorption and Catalytic Activity. *Appl. Catal., B* **2015**, *168−169*, 333−341.
(86) Wang, J.; Li, H.; Li, H.; Yin, S.; Sato, T. Preparation and Photocatalytic Activity of Visible Light-Active Sulfur and Nitrogen Co-Doped $SrTiO_3$. *Solid State Sci.* **2009**, *11*, 182−188.
(87) Peng, B.; Meng, X.; Tang, F.; Ren, X.; Chen, D.; Ren, J. General Synthesis and Optical Properties of Monodisperse Multifunctional Metal-Ion-Doped TiO_2 Hollow Particles. *J. Phys. Chem. C* **2009**, *113*, 20240−20245.
(88) An'amt, M. N.; Radiman, S.; Huang, N. M.; Yarmo, M. A.; Ariyanto, N. P.; Lim, H. N.; Muhamad, M. R. Sol−Gel Hydrothermal Synthesis of Bismuth−TiO_2 Nanocubes for Dye-Sensitized Solar Cell. *Ceram. Int.* **2010**, *36*, 2215−2220.
(89) Guo, M.; Lu, J.; Wu, Y.; Wang, Y.; Luo, M. UV and Visible Raman Studies of Oxygen Vacancies in Rare-Earth-Doped Ceria. *Langmuir* **2011**, *27*, 3872−3877.
(90) Wang, Y.; Zhang, R.; Li, J.; Li, L.; Lin, S. First-Principles Study on Transition Metal-Doped Anatase TiO_2. *Nanoscale Res. Lett.* **2014**, *9*, 46.
(91) Walukiewicz, W. Defect Formation and Diffusion in Heavily Doped Semiconductors. *Phys. Rev. B: Condens. Matter Mater. Phys.* **1994**, *50*, 5221−5225.
(92) Du, J.; Chen, X.-l.; Liu, C.-c.; Ni, J.; Hou, G.-f.; Zhao, Y.; Zhang, X.-d. Highly Transparent and Conductive Indium Tin Oxide Thin Films for Solar Cells Grown by Reactive Thermal Evaporation at Low Temperature. *Appl. Phys. A: Mater. Sci. Process.* **2014**, *117*, 815−822.
(93) Jain, G.; Kumar, R. Electrical and Optical Properties of Tin Oxide and Antimony Doped Tin Oxide Films. *Opt. Mater.* **2004**, *26*, 27−31.
(94) Vijayalakshmi, S.; Venkataraj, S.; Subramanian, M.; Jayavel, R. Physical Properties of Zinc Doped Tin Oxide Films Prepared by Spray Pyrolysis Technique. *J. Phys. D: Appl. Phys.* **2008**, *41*, 035505.
(95) Giraldi, T. R.; Escote, M. T.; Maciel, A. P.; Longo, E.; Leite, E. R.; Varela, J. A. Transport and Sensors Properties of Nanostructured Antimony-Doped Tin Oxide Films. *Thin Solid Films* **2006**, *515*, 2678−2685.
(96) Zhang, Z.; Wu, Q.; Johnson, G.; Ye, Y.; Li, X.; Li, N.; Cui, M.; Lee, J. D.; Liu, C.; Zhao, S.; Li, S.; Orlov, A.; Murray, C. B.; Zhang, X.; Gunnoe, T. B.; Su, D.; Zhang, S. Generalized Synthetic Strategy for Transition-Metal-Doped Brookite-Phase TiO_2 Nanorods. *J. Am. Chem. Soc.* **2019**, *141*, 16548−16552.
(97) Wang, Q.; Hisatomi, T.; Ma, S. S. K.; Li, Y.; Domen, K. Core/Shell Structured La- and Rh-Codoped $SrTiO_3$ as a Hydrogen Evolution Photocatalyst in Z-Scheme Overall Water Splitting under Visible Light Irradiation. *Chem. Mater.* **2014**, *26*, 4144−4150.
(98) Cai, F.; Meng, Y.; Hu, B.; Tang, Y.; Shi, W. Microwave-Assisted Synthesis of La−Cr Co-Doped $SrTiO_3$ Nano-Particles and their Use in Photocatalytic Hydrogen Evolution under Visible Light. *RSC Adv.* **2015**, *5*, 57354−57360.
(99) Zhang, P.; Yu, Y.; Wang, E.; Wang, J.; Yao, J.; Cao, Y. Structure of Nitrogen and Zirconium Co-Doped Titania with Enhanced Visible-Light Photocatalytic Activity. *ACS Appl. Mater. Interfaces* **2014**, *6*, 4622−4629.
(100) Belfaa, K.; Lassoued, M. S.; Ammar, S.; Gadri, A. Synthesis and Characterization of V-Doped TiO_2 Nanoparticles through Polyol Method with Enhanced Photocatalytic Activities. *J. Mater. Sci.: Mater. Electron.* **2018**, *29*, 10269−10276.
(101) Daghrir, R.; Drogui, P.; Robert, D. Modified TiO_2 For Environmental Photocatalytic Applications: A Review. *Ind. Eng. Chem. Res.* **2013**, *52*, 3581−3599.
(102) Wang, J.; Chen, R.; Xiang, L.; Komarneni, S. Synthesis, Properties and Applications of ZnO Nanomaterials with Oxygen Vacancies: A Review. *Ceram. Int.* **2018**, *44*, 7357−7377.
(103) Nasr, M.; Eid, C.; Habchi, R.; Miele, P.; Bechelany, M. Recent Progress on Titanium Dioxide Nanomaterials for Photocatalytic Applications. *ChemSusChem* **2018**, *11*, 3023−3047.
(104) Kołodziejczak-Radzimska, A.; Jesionowski, T. Zinc Oxide-From Synthesis to Application: A Review. *Materials* **2014**, *7*, 2833−2881.
(105) Asahi, R.; Morikawa, T.; Ohwaki, T.; Aoki, K.; Taga, Y. Visible-Light Photocatalysis in Nitrogen-Doped Titanium Oxides. *Science* **2001**, *293*, 269.
(106) Zhang, G.; Liu, G.; Wang, L.; Irvine, J. T. S. Inorganic Perovskite Photocatalysts for Solar Energy Utilization. *Chem. Soc. Rev.* **2016**, *45*, 5951−5984.
(107) Medhi, R.; Li, C.-H.; Lee, S. H.; Marquez, M. D.; Jacobson, A. J.; Lee, T.-C.; Lee, T. R. Uniformly Spherical and Monodisperse Antimony- and Zinc-Doped Tin Oxide Nanoparticles for Optical and Electronic Applications. *ACS Appl. Nano Mater.* **2019**, *2*, 6554−6564.
(108) Fan, G.; Tong, J.; Li, F. Visible-Light-Induced Photocatalyst Based on Cobalt-Doped Zinc Ferrite Nanocrystals. *Ind. Eng. Chem. Res.* **2012**, *51*, 13639−13647.
(109) Shao, J.; Sheng, W.; Wang, M.; Li, S.; Chen, J.; Zhang, Y.; Cao, S. In Situ Synthesis of Carbon-Doped TiO_2 Single-Crystal Nanorods with a Remarkably Photocatalytic Efficiency. *Appl. Catal., B* **2017**, *209*, 311−319.
(110) Kiran, V.; Sampath, S. Facile Synthesis of Carbon Doped TiO_2 Nanowires Without an External Carbon Source and their Opto-Electronic Properties. *Nanoscale* **2013**, *5*, 10646−10652.
(111) Qiao, M.; Wu, S.; Chen, Q.; Shen, J. Novel Triethanolamine Assisted Sol−Gel Synthesis of N-Doped TiO_2 Hollow Spheres. *Mater. Lett.* **2010**, *64*, 1398−1400.
(112) Yang, G.; Jiang, Z.; Shi, H.; Xiao, T.; Yan, Z. Preparation of Highly Visible-Light Active N-Doped TiO_2 Photocatalyst. *J. Mater. Chem.* **2010**, *20*, 5301−5309.
(113) Preethi, L. K.; Antony, R. P.; Mathews, T.; Walczak, L.; Gopinath, C. S. A Study on Doped Heterojunctions in TiO_2 Nanotubes: An Efficient Photocatalyst for Solar Water Splitting. *Sci. Rep.* **2017**, *7*, 14314.
(114) Li, X.; Liu, P.; Mao, Y.; Xing, M.; Zhang, J. Preparation of Homogeneous Nitrogen-Doped Mesoporous TiO_2 Spheres with Enhanced Visible-Light Photocatalysis. *Appl. Catal., B* **2015**, *164*, 352−359.
(115) Biswas, A.; Chakraborty, A.; Jana, N. R. Nitrogen and Fluorine Codoped, Colloidal TiO_2 Nanoparticle: Tunable Doping, Large Red-Shifted Band Edge, Visible Light Induced Photocatalysis, and Cell Death. *ACS Appl. Mater. Interfaces* **2018**, *10*, 1976−1986.
(116) Pelaez, M.; de la Cruz, A. A.; Stathatos, E.; Falaras, P.; Dionysiou, D. D. Visible Light-Activated N-F-Codoped TiO_2 Nanoparticles for the Photocatalytic Degradation of Microcystin-LR in Water. *Catal. Today* **2009**, *144*, 19−25.
(117) Zhang, Q.; Li, Y.; Ackerman, E. A.; Gajdardziska-Josifovska, M.; Li, H. Visible Light Responsive Iodine-Doped TiO_2 for Photocatalytic Reduction of CO_2 to Fuels. *Appl. Catal., A* **2011**, *400*, 195−202.
(118) Zuo, F.; Wang, L.; Feng, P. Self-Doped Ti^{3+}@TiO_2 Visible Light Photocatalyst: Influence of Synthetic Parameters on the H_2 Production Activity. *Int. J. Hydrogen Energy* **2014**, *39*, 711−717.
(119) Kumar, R.; Govindarajan, S.; Siri Kiran Janardhana, R. K.; Rao, T. N.; Joshi, S. V.; Anandan, S. Facile One-Step Route for the

https://dx.doi.org/10.1021/acsanm.0c01035
ACS Appl. Nano Mater. 2020, 3, 6156−6185

Development of in Situ Cocatalyst-Modified Ti^{3+} Self-Doped TiO_2 for Improved Visible-Light Photocatalytic Activity. *ACS Appl. Mater. Interfaces* **2016**, *8*, 27642−27653.
(120) Zhou, Y.; Chen, C.; Wang, N.; Li, Y.; Ding, H. Stable Ti^{3+} Self-Doped Anatase-Rutile Mixed TiO_2 with Enhanced Visible Light Utilization and Durability. *J. Phys. Chem. C* **2016**, *120*, 6116−6124.
(121) Zhang, Y.; Xing, Z.; Liu, X.; Li, Z.; Wu, X.; Jiang, J.; Li, M.; Zhu, Q.; Zhou, W. Ti^{3+} Self-Doped Blue TiO_2(B) Single-Crystalline Nanorods for Efficient Solar-Driven Photocatalytic Performance. *ACS Appl. Mater. Interfaces* **2016**, *8*, 26851−26859.
(122) Takle, S. P.; Naik, S. D.; Khore, S. K.; Ohwal, S. A.; Bhujbal, N. M.; Landge, S. L.; Kale, B. B.; Sonawane, R. S. Photodegradation of Spent Wash, a Sugar Industry Waste, Using Vanadium-Doped TiO_2 Nanoparticles. *RSC Adv.* **2018**, *8*, 20394−20405.
(123) Li, L.; Liu, C.-y.; Liu, Y. Study on Activities of Vanadium (IV/V) Doped TiO_2(R) Nanorods Induced by UV and Visible Light. *Mater. Chem. Phys.* **2009**, *113*, 551−557.
(124) Zhu, H.; Tao, J.; Dong, X. Preparation and Photoelectrochemical Activity of Cr-Doped TiO_2 Nanorods with Nanocavities. *J. Phys. Chem. C* **2010**, *114*, 2873−2879.
(125) Tian, B.; Li, C.; Zhang, J. One-Step Preparation, Characterization and Visible-Light Photocatalytic Activity of Cr-Doped TiO_2 with Anatase and Rutile Bicrystalline Phases. *Chem. Eng. J.* **2012**, *191*, 402−409.
(126) Eshaghi, A.; Moradi, H. Optical and Photocatalytic Properties of the Fe-Doped TiO_2 Nanoparticles Loaded on the Activated Carbon. *Adv. Powder Technol.* **2018**, *29*, 1879−1885.
(127) Liu, Y.; Wei, J. H.; Xiong, R.; Pan, C. X.; Shi, J. Enhanced Visible Light Photocatalytic Properties of Fe-Doped TiO_2 Nanorod Clusters and Monodispersed Nanoparticles. *Appl. Surf. Sci.* **2011**, *257*, 8121−8126.
(128) Wu, Y.; Zhang, J.; Xiao, L.; Chen, F. Preparation and Characterization of TiO_2 Photocatalysts by Fe^{3+} Doping Together with Au Deposition for the Degradation of Organic Pollutants. *Appl. Catal., B* **2009**, *88*, 525−532.
(129) Tong, T.; Zhang, J.; Tian, B.; Chen, F.; He, D. Preparation of Fe^{3+}-Doped TiO_2 Catalysts by Controlled Hydrolysis of Titanium Alkoxide and Study on their Photocatalytic Activity for Methyl Orange Degradation. *J. Hazard. Mater.* **2008**, *155*, 572−579.
(130) Kashale, A. A.; Rasal, A. S.; Kamble, G. P.; Ingole, V. H.; Dwivedi, P. K.; Rajoba, S. J.; Jadhav, L. D.; Ling, Y.-C.; Chang, J.-Y.; Ghule, A. V. Biosynthesized Co-Doped TiO_2 Nanoparticles Based Anode for Lithium-Ion Battery Application and Investigating the Influence of Dopant Concentrations on its Performance. *Composites, Part B* **2019**, *167*, 44−50.
(131) Khurana, C.; Pandey, O. P.; Chudasama, B. Synthesis of Visible Light-Responsive Cobalt-Doped TiO_2 Nanoparticles with Tunable Optical Bandgap. *J. Sol-Gel Sci. Technol.* **2015**, *75*, 424−435.
(132) Miyauchi, M.; Liu, Z.; Zhao, Z.-G.; Anandan, S.; Tokudome, H. Visible-Light-Driven Superhydrophilicity by Interfacial Charge Transfer between Metal Ions and Metal Oxide Nanostructures. *Langmuir* **2010**, *26*, 796−801.
(133) Benjwal, P.; De, B.; Kar, K. K. 1-D and 2-D Morphology of Metal Cation Co-Doped (Zn, Mn) TiO_2 and Investigation of their Photocatalytic Activity. *Appl. Surf. Sci.* **2018**, *427*, 262−272.
(134) Lim, J.; Monllor-Satoca, D.; Jang, J. S.; Lee, S.; Choi, W. Visible Light Photocatalysis of Fullerol-Complexed TiO_2 Enhanced by Nb Doping. *Appl. Catal., B* **2014**, *152*−*153*, 233−240.
(135) Cao, S.; Zhang, S.; Zhang, T.; Fisher, A.; Lee, J. Y. Metal-Doped TiO_2 Colloidal Nanocrystals with Broadly Tunable Plasmon Resonance Absorption. *J. Mater. Chem. C* **2018**, *6*, 4007−4014.
(136) Chang, S.-m.; Doong, R.-a. Characterization of Zr-Doped TiO_2 Nanocrystals Prepared by a Nonhydrolytic Sol-Gel Method at High Temperatures. *J. Phys. Chem. B* **2006**, *110*, 20808−20814.
(137) Naraginti, S.; Li, Y.; Wu, Y. A Visible Light Mediated Synergistic Catalyst for Effective Inactivation of E. coli and Degradation of Azo Dye Direct Red-22 with Mechanism Investigation. *RSC Adv.* **2016**, *6*, 75724−75735.
(138) Ali, T.; Ahmed, A.; Alam, U.; Uddin, I.; Tripathi, P.; Muneer, M. Enhanced Photocatalytic and Antibacterial Activities of Ag-Doped TiO_2 Nanoparticles under Visible Light. *Mater. Chem. Phys.* **2018**, *212*, 325−335.
(139) Li, H.; Wang, D.; Wang, P.; Fan, H.; Xie, T. Synthesis and Studies of the Visible-Light Photocatalytic Properties of Near-Monodisperse Bi-Doped TiO_2 Nanospheres. *Chem. - Eur. J.* **2009**, *15*, 12521−12527.
(140) Tong, T.; Zhang, J.; Tian, B.; Chen, F.; He, D.; Anpo, M. Preparation of Ce−TiO_2 Catalysts by Controlled Hydrolysis of Titanium Alkoxide Based on Esterification Reaction and Study on its Photocatalytic Activity. *J. Colloid Interface Sci.* **2007**, *315*, 382−388.
(141) Rao, Z.; Xie, X.; Wang, X.; Mahmood, A.; Tong, S.; Ge, M.; Sun, J. Defect Chemistry of Er^{3+}-Doped TiO_2 and Its Photocatalytic Activity for the Degradation of Flowing Gas-Phase VOCs. *J. Phys. Chem. C* **2019**, *123*, 12321−12334.
(142) Zhang, X.; Qin, J.; Hao, R.; Wang, L.; Shen, X.; Yu, R.; Limpanart, S.; Ma, M.; Liu, R. Carbon-Doped ZnO Nanostructures: Facile Synthesis and Visible Light Photocatalytic Applications. *J. Phys. Chem. C* **2015**, *119*, 20544−20554.
(143) Kale, G.; Arbuj, S.; Kawade, U.; Rane, S.; Ambekar, J.; Kale, B. Synthesis of Porous Nitrogen Doped Zinc Oxide Nanostructures using a Novel Paper Mediated Template Method and their Photocatalytic Study for Dye Degradation under Natural Sunlight. *Mater. Chem. Front.* **2018**, *2*, 163−170.
(144) Etacheri, V.; Roshan, R.; Kumar, V. Mg-Doped ZnO Nanoparticles for Efficient Sunlight-Driven Photocatalysis. *ACS Appl. Mater. Interfaces* **2012**, *4*, 2717−2725.
(145) Khan, W.; Khan, Z. A.; Saad, A. A.; Shervani, S.; Saleem, A.; Naqvi, A. H. Synthesis and Characterization of Al Doped ZnO Nanoparticles. *Int. J. Mod. Phys.: Conf. Ser.* **2013**, *22*, 630−636.
(146) Ullah, R.; Dutta, J. Photocatalytic Degradation of Organic Dyes with Manganese-Doped ZnO Nanoparticles. *J. Hazard. Mater.* **2008**, *156*, 194−200.
(147) Han, L.; Wang, D.; Lu, Y.; Jiang, T.; Liu, B.; Lin, Y. Visible-Light-Assisted HCHO Gas Sensing Based on Fe-Doped Flowerlike ZnO at Room Temperature. *J. Phys. Chem. C* **2011**, *115*, 22939−22944.
(148) Jacob, A. A.; Balakrishnan, L.; Shambavi, K.; Alex, Z. C. Multi-Band Visible Photoresponse Study of Co^{2+} Doped ZnO Nanoparticles. *RSC Adv.* **2017**, *7*, 39657−39665.
(149) Bilecka, I.; Luo, L.; Djerdj, I.; Rossell, M. D.; Jagodič, M.; Jagličić, Z.; Masubuchi, Y.; Kikkawa, S.; Niederberger, M. Microwave-Assisted Nonaqueous Sol-Gel Chemistry for Highly Concentrated ZnO-Based Magnetic Semiconductor Nanocrystals. *J. Phys. Chem. C* **2011**, *115*, 1484−1495.
(150) Gupta, J.; Bahadur, D. Visible Light Sensitive Mesoporous Cu-Substituted ZnO Nanoassembly for Enhanced Photocatalysis, Bacterial Inhibition, and Noninvasive Tumor Regression. *ACS Sustainable Chem. Eng.* **2017**, *5*, 8702−8709.
(151) Kanade, K. G.; Kale, B. B.; Baeg, J.-O.; Lee, S. M.; Lee, C. W.; Moon, S.-J.; Chang, H. Self-Assembled Aligned Cu doped ZnO Nanoparticles for Photocatalytic Hydrogen Production under Visible Light Irradiation. *Mater. Chem. Phys.* **2007**, *102*, 98−104.
(152) Lu, Y.-H.; Lin, W.-H.; Yang, C.-Y.; Chiu, Y.-H.; Pu, Y.-C.; Lee, M.-H.; Tseng, Y.-C.; Hsu, Y.-J. A Facile Green Antisolvent Approach to Cu^{2+}−Doped ZnO Nanocrystals with Visible-Light-Responsive Photoactivities. *Nanoscale* **2014**, *6*, 8796−8803.
(153) Nigussie, G. Y.; Tesfamariam, G. M.; Tegegne, B. M.; Weldemichel, Y. A.; Gebreab, T. W.; Gebrehiwot, D. G.; Gebremichel, G. E. Antibacterial Activity of Ag-Doped TiO_2 and Ag-Doped ZnO Nanoparticles. *Int. J. Photoenergy* **2018**, *2018*, 5927485.
(154) Khataee, A.; Darvishi Cheshmeh Soltani, R.; Hanifehpour, Y.; Safarpour, M.; Gholipour Ranjbar, H.; Joo, S. W. Synthesis and Characterization of Dysprosium-Doped ZnO Nanoparticles for Photocatalysis of a Textile Dye under Visible Light Irradiation. *Ind. Eng. Chem. Res.* **2014**, *53*, 1924−1932.

https://dx.doi.org/10.1021/acsanm.0c01035
ACS Appl. Nano Mater. 2020, 3, 6156−6185

(155) Zhang, Q.; Huang, Y.; Xu, L.; Cao, J.-j.; Ho, W.; Lee, S. C. Visible-Light-Active Plasmonic Ag−$SrTiO_3$ Nanocomposites for the Degradation of NO in Air with High Selectivity. *ACS Appl. Mater. Interfaces* **2016**, *8*, 4165−4174.
(156) Joseph, A. I. J.; Thiripuranthagan, S. Metal Doped Titanate Photo Catalysts for the Mineralization of Congo Red under Visible Irradiation. *RSC Adv.* **2015**, *5*, 9792−9805.
(157) Kiss, B.; Manning, T. D.; Hesp, D.; Didier, C.; Taylor, A.; Pickup, D. M.; Chadwick, A. V.; Allison, H. E.; Dhanak, V. R.; Claridge, J. B.; Darwent, J. R.; Rosseinsky, M. J. Nano-Structured Rhodium Doped $SrTiO_3$−Visible Light Activated Photocatalyst for Water Decontamination. *Appl. Catal., B* **2017**, *206*, 547−555.
(158) Senthilkumar, P.; Jency, D. A.; Kavinkumar, T.; Dhayanithi, D.; Dhanuskodi, S.; Umadevi, M.; Manivannan, S.; Giridharan, N. V.; Thiagarajan, V.; Sriramkumar, M.; Jothivenkatachalam, K. Built-in Electric Field Assisted Photocatalytic Dye Degradation and Photoelectrochemical Water Splitting of Ferroelectric Ce Doped $BaTiO_3$ Nanoassemblies. *ACS Sustainable Chem. Eng.* **2019**, *7*, 12032−12043.
(159) Nishioka, S.; Maeda, K. Hydrothermal Synthesis of Rhodium-Doped Barium Titanate Nanocrystals for Enhanced Photocatalytic Hydrogen Evolution under Visible Light. *RSC Adv.* **2015**, *5*, 100123−100128.
(160) Wu, X.; Yin, S.; Dong, Q.; Sato, T. Preparation and Visible Light Induced Photocatalytic Activity of C-$NaTaO_3$ and C-$NaTaO_3$−Cl-TiO_2 Composite. *Phys. Chem. Chem. Phys.* **2013**, *15*, 20633−20640.
(161) Li, F.-F.; Liu, D.-R.; Gao, G.-M.; Xue, B.; Jiang, Y.-S. Improved Visible-Light Photocatalytic Activity of $NaTaO_3$ with Perovskite-like Structure via Sulfur Anion Doping. *Appl. Catal., B* **2015**, *166−167*, 104−111.
(162) Shi, H.; Li, X.; Iwai, H.; Zou, Z.; Ye, J. 2-Propanol Photodegradation over Nitrogen-Doped $NaNbO_3$ Powders under Visible-Light Irradiation. *J. Phys. Chem. Solids* **2009**, *70*, 931−935.
(163) Maeda, K.; Domen, K. Preparation of $BaZrO_3$−$BaTaO_2N$ Solid Solutions and the Photocatalytic Activities for Water Reduction and Oxidation Under Visible Light. *J. Catal.* **2014**, *310*, 67−74.
(164) Chen, S.; Yang, J.; Ding, C.; Li, R.; Jin, S.; Wang, D.; Han, H.; Zhang, F.; Li, C. Nitrogen-Doped Layered Oxide $Sr_5Ta_4O_{15-x}N_x$ for Water Reduction and Oxidation under Visible Light Irradiation. *J. Mater. Chem. A* **2013**, *1*, 5651−5659.
(165) Agorku, E. S.; Kuvarega, A. T.; Mamba, B. B.; Pandey, A. C.; Mishra, A. K. Enhanced Visible-Light Photocatalytic Activity of Multi-Elements-Doped ZrO_2 for Degradation of Indigo Carmine. *J. Rare Earths* **2015**, *33*, 498−506.
(166) Qiu, X.; Zhao, Y.; Burda, C. Synthesis and Characterization of Nitrogen-Doped Group IVB Visible-Light-Photoactive Metal Oxide Nanoparticles. *Adv. Mater.* **2007**, *19*, 3995−3999.
(167) Runnerstrom, E. L.; Bergerud, A.; Agrawal, A.; Johns, R. W.; Dahlman, C. J.; Singh, A.; Selbach, S. M.; Milliron, D. J. Defect Engineering in Plasmonic Metal Oxide Nanocrystals. *Nano Lett.* **2016**, *16*, 3390−3398.
(168) Jansons, A. W.; Hutchison, J. E. Continuous Growth of Metal Oxide Nanocrystals: Enhanced Control of Nanocrystal Size and Radial Dopant Distribution. *ACS Nano* **2016**, *10*, 6942−6951.
(169) Irie, H.; Miura, S.; Kamiya, K.; Hashimoto, K. Efficient Visible Light-Sensitive Photocatalysts: Grafting Cu(II) Ions onto TiO_2 and WO_3 Photocatalysts. *Chem. Phys. Lett.* **2008**, *457*, 202−205.
(170) Nakamura, R.; Okamoto, A.; Osawa, H.; Irie, H.; Hashimoto, K. Design of All-Inorganic Molecular-Based Photocatalysts Sensitive to Visible Light: Ti(IV)-O-Ce(III) Bimetallic Assemblies on Mesoporous Silica. *J. Am. Chem. Soc.* **2007**, *129*, 9596−9597.
(171) Irie, H.; Kamiya, K.; Shibanuma, T.; Miura, S.; Tryk, D. A.; Yokoyama, T.; Hashimoto, K. Visible Light-Sensitive Cu(II)-Grafted TiO_2 Photocatalysts: Activities and X-ray Absorption Fine Structure Analyses. *J. Phys. Chem. C* **2009**, *113*, 10761−10766.
(172) Escudero, A.; Becerro, A. I.; Carrillo-Carrion, C.; Nunez, N. O.; Zyuzin, M. V.; Laguna, M.; Gonzalez-Mancebo, D.; Ocana, M.; Parak, W. J. Rare Earth Based Nanostructured Materials: Synthesis, Functionalization, Properties and Bioimaging and Biosensing Applications. *Nanophotonics* **2017**, *6*, 881−921.
(173) Pathak, T. K.; Kumar, V.; Purohit, L. P. High Quality Nitrogen-Doped Zinc Oxide Thin Films Grown on ITO by Sol−Gel Method. *Phys. E* **2015**, *74*, 551−555.
(174) Ng, Z.-N.; Chan, K.-Y.; Muslimin, S.; Knipp, D. P-Type Characteristic of Nitrogen-Doped ZnO Films. *J. Electron. Mater.* **2018**, *47*, 5607−5613.
(175) Yi-Hao, T.; Hang, Z.; Yin, W.; Ming-Hui, D.; Guo, J.; Bin, Z. Facile Fabrication of Nitrogen-Doped Zinc Oxide Nanoparticles with Enhanced Photocatalytic Performance. *Micro Nano Lett.* **2015**, *10*, 432−434.
(176) Chavillon, B.; Cario, L.; Renaud, A.; Tessier, F.; Cheviré, F.; Boujtita, M.; Pellegrin, Y.; Blart, E.; Smeigh, A.; Hammarström, L.; Odobel, F.; Jobic, S. P-Type Nitrogen-Doped ZnO Nanoparticles Stable under Ambient Conditions. *J. Am. Chem. Soc.* **2012**, *134*, 464−470.
(177) Lu, X.; Liu, Z.; Zhu, Y.; Jiang, L. Sonochemical Synthesis and Photocatalytic Property of Zinc Oxide Nanoparticles Doped with Magnesium(II). *Mater. Res. Bull.* **2011**, *46*, 1638−1641.
(178) Zhou, X.; Shi, J.; Li, C. Effect of Metal Doping on Electronic Structure and Visible Light Absorption of $SrTiO_3$ and $NaTaO_3$ (Metal = Mn, Fe, and Co). *J. Phys. Chem. C* **2011**, *115*, 8305−8311.
(179) Saw, K. G.; Aznan, N. M.; Yam, F. K.; Ng, S. S.; Pung, S. Y. New Insights on the Burstein-Moss Shift and Bandgap Narrowing in Indium-Doped Zinc Oxide Thin Films. *PLoS One* **2015**, *10*, No. e0141180.
(180) Yogamalar, N. R.; Chandra Bose, A. Burstein−Moss Shift and Room Temperature Near-Band-Edge Luminescence in Lithium-Doped Zinc Oxide. *Appl. Phys. A: Mater. Sci. Process.* **2011**, *103*, 33−42.
(181) Nakano, Y.; Saeki, S.; Morikawa, T. Optical Bandgap Widening of p-Type Cu_2O Films by Nitrogen Doping. *Appl. Phys. Lett.* **2009**, *94*, 022111.
(182) Di Trolio, A.; Bauer, E. M.; Scavia, G.; Veroli, C. Blueshift of Optical Bandgap in c-Axis Oriented and Conducting Al-Doped ZnO Thin Films. *J. Appl. Phys.* **2009**, *105*, 113109.
(183) Wang, L.; Sofer, Z.; Pumera, M. Will Any Crap We Put into Graphene Increase Its Electrocatalytic Effect? *ACS Nano* **2020**, *14*, 21−25.

https://dx.doi.org/10.1021/acsanm.0c01035
ACS Appl. Nano Mater. 2020, 3, 6156−6185